Astronomy & Astrophysics manuscript no. xitau
May 25, 2016

ξ Tauri: a unique laboratory to study the dynamic interaction in a compact hierarchical quadruple system ⋆ ⋆⋆

J.A. Nemravová[1], P. Harmanec[1], M. Brož[1], D. Vokrouhlický[1], D. Mourard[2], C.A. Hummel[3], C. Cameron[4], J.M. Matthews[5], C.T. Bolton[6], H. Božić[7], R. Chini[8,9], T. Dembsky[8], S. Engle[10], C. Farrington[11], J.H. Grunhut[3], D.B. Guenther[12], E.F. Guinan[10], D. Korčáková[1], P. Koubský[13], R. Kříček[1], R. Kuschnig[14], P. Mayer[1], G.P. McCook[10], A.F.J. Moffat[15], N. Nardetto[2], A. Prša[10], J. Ribeiro[16], J. Rowe[17], S. Rucinski[6], P. Škoda[13], M. Šlechta[13], I. Tallon-Bosc[18], V. Votruba[13], W.W. Weiss[14], M. Wolf[1], R.T. Zavala[19], and P. Zasche[1]

(Affiliations can be found after the references)

Release May 25, 2016

ABSTRACT

Context. Compact hierarchical systems are important, since the effects caused by the dynamical interaction among its members occur on a human time-scale. These interactions play a role in the formation of close binaries through Kozai cycles with tides. One such system is ξ Tauri with three hierarchical orbits: (i) 7.14 d (eclipsing components Aa, Ab), (ii) 145 d (components Aa+Ab, B), and (iii) 51 yr (components Aa+Ab+B, C).
Aims. (i) To obtain physical properties of the system, and (ii) to study the dynamical interaction between its components.
Methods. Our analysis is based on a large series of spectroscopic, photometric (including space-borne) observations, and long-baseline optical and infrared spectro-interferometric observations. We use two approaches to infer the system properties: (i) a set of "observation-specific" models, where all components have elliptical trajectories, and (ii) an N-body model, which computes the trajectory of each component by integration of Newton's equations of motion.
Results. (i) The triple subsystem exhibits clear signs of dynamical interaction. The most pronounced are the advance of the apsidal line and eclipse-timing variations. (ii) We determined the geometry of all three orbits using both the observation-specific and N-body models. The latter correctly accounted for observed effects of the dynamical interaction, predicted cyclic variations of orbital inclinations, and determined the sense of motion of all orbits. (iii) Using perturbation theory we demonstrated that prominent secular and periodic dynamical effects are explainable with a quadrupole interaction. (iv) We constrained basic properties of all components, especially of members of the inner triple subsystem, detected rapid low-amplitude light variations, attributing them to co-rotating surface structures of component B, and estimated the radius of component B. Properties of component C remain uncertain because of its low relative luminosity. (v) We provided an independent estimate of the distance to the system.
Conclusions. Accuracy and consistency of our results make ξ Tau an excellent test bed for models of formation and evolution of hierarchical systems.

Key words. stars: binaries: close – stars: binaries: spectroscopic – stars: binaries: eclipsing – stars: kinematics and dynamics stars: fundamental parameters – stars: individual: ξ Tau

1. Introduction

Binaries and multiple systems play a crucial role in our understanding of the formation, stability, and evolution of stars and their hierarchies starting from simple binaries up to galaxies.

Among all known binaries, those that eclipse have represented the most useful group, since - until recently - accurate determination of component masses and radii was possible primarily for them. For binaries with components of different masses, a common origin of the system also provided a stringent test of the models of stellar evolution. At the same time, however, this fact represented an unpleasant selection effect, especially for binaries with hot components and rapid rotation: we have observed them roughly equator-on only.

The recent rapid advances in optical interferometry allowing the usage of longer baselines, co-phasing of more telescopes and longer integration times, provided the chance to obtain accurate basic physical properties also for non-eclipsing binaries. It is possible to obtain the spatial orbit of such binaries and derive their accurate orbital inclination. In combination with radial-velocity (RV) curves, this allows the determination of component masses and the absolute value of the semi-major axis. Since the interferometric orbit provides the angular value of the semi-major axis, one also obtains an estimate of the distance of the binary, which is completely independent of the photometric distance modulus. In the most favourable cases, long-baseline interferometry can also provide independent estimates of the component radii.

A large number of binaries are actually members of multiple systems (Eggleton & Tokovinin 2008). In cases when it is possible to derive masses of more than two components, one can study not only the nuclear but also the dynamical evolution of such systems. It has been suggested that the formation of triple

Send offprint requests to: J.A. Nemravová,
e-mail: jana.nemravova@gmail.com

⋆ Tables D.1 – D.7 are available only in electronic form at the CDS via anonymous ftp to cdarc.u-strasbg.fr (130.79.128.5) or web page http://cdsweb.u-strasbg.fr/cgi-bin/qcat?J/A+A/.

⋆⋆ **Based on data from the MOST satellite, a former Canadian Space Agency mission, jointly operated by Microsatellite Systems Canada Inc. (MSCI; formerly Dynacon Inc.), the University of Toronto Institute for Aerospace Studies and the University of British Columbia, with the assistance of the University of Vienna.**

systems, containing a compact binary accompanied by a distant component, was dynamically very colourful. During the evolution, gravitational interactions of the three stars are expected to excite the eccentricity of the binary via Kozai mechanism, bringing them close to each other. Later, tides stabilised the system by not letting the Kozai-pumped eccentricity to further increase and reverted the trend to circularisation (e.g. Eggleton & Kiseleva-Eggleton 2001; Fabrycky & Tremaine 2007). Even though we cannot observe the systems at their dynamically violent youth, we can still appreciate some degree of dynamical evolution produced by continued gravitational interactions of the three stars. In order to compare predictions of the theory with observations, one has to know the mutual orientation of orbits with respect to each other, i.e. their inclinations and the longitudes of ascending nodes. These are available only for objects for which an astrometric orbit is known. This in turn can only be obtained with interferometry.

This study is devoted to an investigation of one such system, a unique and rare close quadruple system ξ Tau, whose favourable orbital geometry and luminosity ratios between its components allow the determination of physical properties of the system and its components with high precision and the study of possible dynamical effects in the system. ξ Tau (2 Tau, HD 21364, HIP 16083, HR 1038) is a hierarchical quadruple system, consisting of two sharp-lined A stars, which undergo binary eclipses, a more distant broad-lined B star and a much more distant F star. The visual magnitude $V = 3.72$ mag, the declination of $9°44'$, and quite accurate Hipparcos parallax 15.6 ± 1.04 mas (van Leeuwen 2007) make ξ Tau an easy and interesting target for a wide range of instruments and observational techniques.

The binary nature of the system was discovered by Campbell (1909). The wide orbit was first resolved by Mason et al. (1999) via speckle interferometry. All later available speckle-interferometric observations were analysed by Rica Romero (2010), who derived an astrometric orbit. The inner triple system was first mentioned by Fekel (1981), who quoted orbital periods of 7.15 d and 145.0 d based on a private communication from C.T. Bolton. The orbital elements of the triple subsystem were published in a catalogue by Tokovinin (1997). More accurate elements were given in a preliminary report by Bolton & Grunhut (2007), who obtained periods of 7.1466440(49) d and 145.1317(40) d. They were also the first to note that the inner binary is an eclipsing system, based on Hipparcos photometry. Hummel et al. (2013) reported a solution of the 145.2 d orbit based on interferometric observations. The first detailed, but still preliminary study of ξ Tau was published by Nemravová et al. (2013). These authors analysed numerous spectral, photometric and interferometric observations and discovered the presence of apsidal motion of the 145.2 d orbit with period 224 ± 147 yrs. They were able to disentangle the spectra of both A stars and the broad-lined B star.

The system is quite complex, hence we provide a basic summary of its orbital elements and properties of its components based on our analysis presented in following Sects. in Table 1. It serves only to introduce the system and should not be mistaken with results.

This paper represents a complex study of the system, based on analyses of a huge and unique body of spectral, photometric and spectro-interferometric and astrometric data. Each type of observations is first analysed separately by more or less standard means (Sects. 3, 4, 5, and 6) and the results are then confronted and critically compared in Sect. 7. Using them as the initial starting point, we then present the N-body model of the whole quadruple system, in which also the mutual interactions of the orbits are modelled. This is a new approach, which tries to embrace almost all available pieces of information and which provides the best description of the geometry and dynamics of the system to date (see Sect. 8.1). Finally, in Sect. 9, we recall some results of a simple perturbation theory which allows us to understand the principal dynamical effects revealed by the numerical model from Sect. 8.1.

In the following text we shall denote the individual components and orbits of the system as follows: Components Aa and Ab are the primary and secondary of the close eclipsing subsystem revolving in a 7.15 d orbit, labelled no.1. Component B is the broad-lined star of spectral type B, revolving with the close pair in the 145 d orbit, labelled no. 2. Finally, we denote the faint and very distant F-type star as component C and its 51 yr orbit with the triple subsystem as orbit, labelled no. 3.

Table 1. Brief summary of orbital elements and properties of components of ξ Tau. It serves only for introductory purposes and does not present final results. P denotes the orbital period, e the eccentricity, i the inclination, Cpts. components of an orbit, Sp.T. the spectral type, m the mass, and V the apparent magnitude in the Johnson V filter.

		Orbit		
Quantity		1	2	3
P	(d)	7.14664	145.12	18 630
e		$\lesssim 0.01$	0.21	0.564
i	(deg)	86.8	86.6	-24.4
a	($R_\odot$)	25.3	233	6 097
Cpts.		Aa+Ab	A[1]+B	AB[2]+C
Sp.T.		B9V+B9V	+B5V	+F5V[3]
m	($M_\odot$)	2.25+2.13	+3.73	+0.92[4]
V	(mag)	5.46+5.53	+4.25	+7.55[3]

Notes. [1]A denotes the inner eclipsing system Aa+Ab. [2]AB denotes the intermediate system A+B. [3]Based on the magnitude difference listed in the Hipparcos and Tycho catalogue (ESA 1997). [4]The evident mismatch between the spectral type and its mass is due to high uncertainty of both parameters.

2. Observations and reductions

Here we provide only basic information about the observational material at our disposal. More details on the datasets and their reductions are in Appendices A, B, and C.

Throughout this paper we use a shortened form of heliocentric Julian dates, reduced Julian dates given as RJD = HJD−2 400 000.0.

2.1. Spectral observations

The series of spectroscopic observations, which has already been used by Nemravová et al. (2013) was complemented with more recent ones secured at Ondřejov, La Silla: echelle spectrograph FEROS (Kaufer et al. 1999), and Cerro Armazones: the BESO spectrograph (Steiner et al. 2008; Fuhrmann et al. 2011). Four archival ELODIE echelle spectra were also used (Moultaka et al. 2004). Having now a rich collection of electronic spectra, we no longer needed the early RVs from the DDO photographic spectra, used by Nemravová et al. (2013). The spectra were primarily used to obtain RV measurements of all three components of the close triple subsystem. The journal of all available spectra with the number of measured RVs for components of the inner triple

Table 2. Journal of spectroscopic observations. For each instrument: ΔT refers to the time span between the first and the last measurement, N gives the number of RVs measured for components Aa, Ab, and B, $\Delta\lambda$ is the wavelength interval covered by the spectra in question, and R is the spectral resolution.

ΔT (RJD)	N Aa/Ab/B	$\Delta\lambda$ (Å)	R	Ins.
49 300.7–52 670.5	37/37/37	4357–4568	10 800	DDO
51 960.3–53 637.6	04/04/04	4270–4523	42 000	ELO
	04/04/04	4759–4991		
	04/04/04	6260–6735		
55 041.9–55 867.6	13/13/13	4270–4523	48 000	BES
	13/13/13	4759–4991		
	13/13/13	6260–6735		
55 579.4–56 357.3	34/34/34	4270–4523	19 200	OND
56 579.4–56 889.6	05/04/05	4274–4508	19 200	OND
55 579.3–55 645.3	02/02/02	4378–4632	17 700	OND
55 579.3–56 357.3	20/20/20	4753–5005	19 300	OND
56 527.6–56 592.5	05/05/05	4759–4991	21 500	OND
56 527.6–56 889.6	14/14/14	6260–6735	14 000	OND
55 561.3–56 357.3	58/58/59	6255–6767	12 700	OND
55 597.4–55 980.3	19/19/22	6497–6688	14 000	LIS
56 555.7–56 564.7	12/12/12	4270–4523	48 000	FER
	12/12/12	4759–4991		
	12/12/12	6260–6735		

Notes. In column 'Ins.': DDO - David Dunlap Observatory 1.9 m reflector, Cassegrain CCD spectrograph; ELO - Haute Provence Observatory 1.2 m reflector, echelle ELODIE CCD spectrograph; BES - Cerro Amazones Hexapod Telescope, BESO echelle CCD spectrograph; OND - Ondřejov Observatory 2 m reflector, coudé CCD spectrograph; LIS - Lisbon Observatory of the Instituto Geográfico do Exército, reflector, CCD spectrograph; FER - La Silla 2.2 m reflector, Feros echelle CCD spectrograph.

subsystem is in Table 2. More details on the spectra and their reductions can be found in Appendix A.

Radial-velocities measured on the available spectra (see Sect. 3.2) are listed in Table D.1.

2.2. Photometric observations

Photometry, which has already been used by Nemravová et al. (2013) was complemented by very accurate observations acquired almost continuously over two weeks with the MOST satellite (Walker et al. 2003), and by another series of Johnson UBV observations from Hvar. Additionally, we also analysed the photometric minima published by Zasche et al. (2014).

The MOST satellite monitored ξ Tau over 16 days almost continuously. It acquired 21 525 observations, which – after the initial reduction by the MOST team – were still affected by two systematic effects: (i) The stray light from the Earth atmosphere, which introduced narrow peaks with separation ≈ 101 minutes, i.e. the MOST orbital period, and (ii) the relaxation time after the change of the observed field, during which the CCD had to reach a thermal equilibrium. This manifests itself by a slowly decreasing offset, usually lasting several tens of minutes. The first effect was, with the exception of few observations during eclipses, removed with a low-passband Butterworth filter (Butterworth 1930). The second effect forced us to neglect all observations secured prior to RJD = 56 522. The remaining 18 510 observations were then subjected to analysis.

A journal of available photometric observations is in Table 3 and more details on the observations and data reductions can be found in Appendix B.

Reduced UBV photometric observations acquired at Hvar Observatory, South African Astronomical Observatory, Four College APT, and photometric observations acquired with the MOST satellite are listed in Tables D.2, D.3, D.4, and D.5.

Table 4. Journal of the spectro-interferometric observations. ΔT is the **time span** RJD of the first and the last observation, ΔB the range of the projected baselines, $\Delta\lambda$ the wavelength range, N_{V^2} the total number of visibility observations, and N_{T3_ϕ} the total number of closure phase observations.

Instr.	ΔT (RJD)	ΔB (m)	$\Delta\lambda$ (nm)	$N_{\mathrm{V}^2}/N_{\mathrm{T3}_\phi}$
1	48 275–48 563	14–30	500–800	108/0
2	51 093–56 298	0–79	550–850	13 461/4 137
3	55 825–56 228	31–279	532–760	6 132/0
4	56 264–56 264	41–139	1 200–2 600	2 160/720

Notes. In column 'Instr.': 1 - Mark III, 2 - NPOI, 3 - CHARA/VEGA, 4 - VLTI/AMBER.

2.3. Interferometric observations

The system was observed by **four** different spectro-interferometers: (i) The Mark III Stellar Interferometer[1] (Mark III) (Shao et al. 1988), (ii) the Navy Precision Optical Interferometer (NPOI) (Armstrong et al. 1998), (iii) the Visible spEctroGraph and polArimeter (VEGA) (Mourard et al. 2009) mounted at the Centre for High Angular Resolution Astronomy (CHARA) (ten Brummelaar et al. 2005), and (iv) the Astronomical Multi-BEam combineR (AMBER) (Petrov et al. 2007) attached to the Very Large Telescope Interferometer (VLTI) (Glindemann et al. 2004). **A journal of the spectro-interferometric observations is in Table 4.** The phase coverage of orbits 1 and 2 with all spectro-interferometric observations is shown in Fig. 1. Details on the spectro-interferometric observations **and their reduction** are provided in Appendix C.

Reduced spectro-interferometric observations from all four instruments are listed in form of calibrated squared visibility moduli in Table D.6 and closure phases in Table D.7.

3. Spectroscopy

The spectral lines of all three components of the triple subsystem (i.e. orbits 1 and 2) of ξ Tau are clearly seen in all available spectra. Component C was not detected in any of the spectra at our disposal, because its relative luminosity is less than 1%, i.e. beyond the detection limit of the available spectra. Attempts to detect its spectral lines were carried out via spectral disentangling and a comparison of the near infrared spectra with synthetic profiles, both with null results.

Two different approaches to derive the orbital elements of the triple subsystem of ξ Tau were used. The first one was a direct analysis of RVs measured with the method described in Sect. 3.2 and the second one was the spectral disentangling (Simon & Sturm 1994; Hadrava 1995) in Sect. 3.3.

[1] Decommissioned in 1992.

Table 3. Journal of photometric observations. For each row: N is the number of observations in each of the filters used, ΔT is the time span covered by each dataset, column 'Passbands' shows the photometric filters used, column 'Comp/Check' lists the names of comparison and check star used. UBV denote the Johnson filters, and MO denotes the broad-band filter of the MOST satellite.

N	ΔT (RJD)	Passbands	Comp / Check	Instrument
441/451/452	46 324.6–56 882.6[1]	UBV	4 Tau / 6 Tau	HVAR
69	47 909.6–48 695.0	$V(H_{\rm p})$[2]	all-sky	HIPP
26/26/26	55 569.3–55 579.4	UBV	6 Tau / 4 Tau	SAAO
131/133/135	55 883.9–55 956.8	UBV	4 Tau / 6 Tau	VILL
18 510	56 222.0–56 238.0	MO	all-sky	MOST

Notes. [1]Only three observations were taken before RJD $= 54\,116$, all at RJD $= 46\,324$. [2]The original Hipparcos $H_{\rm p}$ broad-band observations were transformed to the Johnson V filter after Harmanec (1998). However for the light-curve solutions the limb darkening coefficients corresponding to the original Hipparcos passband were used. Instruments: HVAR - Hvar Observatory 0.65 m Cassegrain reflector, photoelectric photometer; HIPP - The ESA Hipparcos Astrometric Mission; SAAO - South African Astronomical Observatory 0.5 m Cassegrain reflector, Lucy photoelectric photometer; VILL - the Four College 0.8 m reflector, photoelectric photometer; MOST - the Canadian MOST satellite.

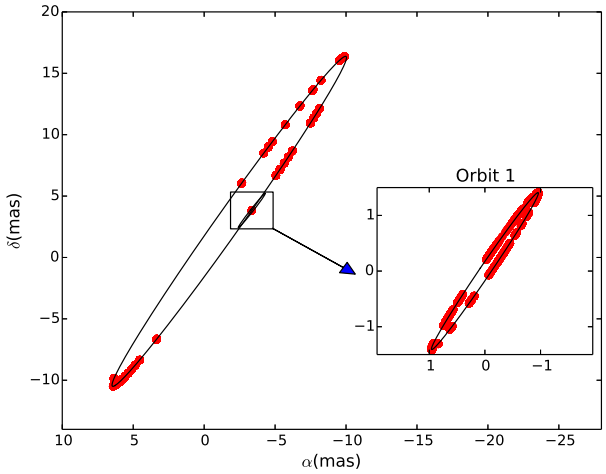

Fig. 1. Coverage of orbits 1 and 2 with the spectro-interferometric observations. ***The outer plot:*** **black line denotes the orbit of the centre of mass of the eclipsing binary relative to component B (which resides at the beginning of the coordinate system of the outer plot), and red dots denote relative position of centre of mass of the eclipsing binary relative to component B at epochs of spectro-interferometric observations.** ***The inset plot:*** **black line denotes orbit of component Ab relative to component Aa (which resides at the beginning of the coordinate system of the inset plot), and red dots denote relative position component Ab relative to component Aa at epochs of spectro-interferometric observations. In case of both plots, the orbital elements are invariable, i.e. they do not show true orbits 1, and 2 as they would appear on the sky, but only demonstrate that the spectro-interferometric observations sample the orbits well enough to constrain elements of both orbits.**

Additionally, we also derived the basic radiative properties of ξ Tau using the comparison of the synthetic to observed and disentangled spectra.

3.1. RVs measured via comparison of the observed and synthetic line profiles

RVs were derived using an automatic method based on the comparison of synthetic and observed spectra, searching for the best match with the optimisation of χ^2 given by:

$$\chi^2 = \sum_{i=1}^{N_{\rm I}} \left(\frac{I_{\rm OBS}\left(\lambda_i\right) - \sum_{j=1}^{N_{\rm C}} I_{{\rm SYN},j}\left(\lambda_i, RV_j\right)}{\sigma_i} \right)^2 , \qquad (1)$$

where $I_{\rm OBS}$ is the observed spectrum, $I_{{\rm SYN},j}$ the synthetic spectrum of the j-th component, $N_{\rm I}$ is the number of discrete elements of the digitised spectrum, $N_{\rm C}$ is the number of the components of the system, RV_j the radial velocity of the j-th component, and σ_i the standard deviation of the i-th point of the observed spectrum, which was estimated from the continuum and adopted for the whole spectrum.

The majority of the spectra at our disposal was acquired in three wavelength regions $\Delta\lambda \in \{4200-4500; 4750-5000; 6200-6700\}$ Å. Each region contains a Balmer line, which turned out to be the best one for measurement of the RVs of component B and several metallic lines, which gave accurate RVs of components Aa and Ab. These regions were also extracted from echelle spectra, and RVs were measured on each region independently. The last region (Hα) contains a number of telluric lines, including the Hα line itself. Our model is unable to account for telluric spectrum and consequently it was not possible to measure accurate RVs of Hα with this technique.

Initial RVs for the searching program were computed from the orbital solution presented in Nemravová et al. (2013) and the RV for each component was searched over the interval $[-70; 70]$ km s^{-1} surrounding the initial estimate. The similarity of components of the eclipsing binary Aa, and Ab required us to control whether the two components have not been interchanged by the program, especially near the conjunctions. If they were, the search was repeated using a narrower search interval.

RVs and their uncertainty were estimated in the following way:

1. The parameters of synthetic spectra were chosen randomly from the Gaussian distributions centred at values listed in Table 7 and the standard deviations were set to their uncertainties.
2. The synthetic spectra were fitted to the observed ones. The procedure was repeated five hundred times for each spectrum and the RV including its uncertainty was estimated from the resulting distribution.

This approach allowed us to estimate only the 'statistical' part of the total **uncertainty**. Usually, the statistical uncertainty

$\Delta RV_{\rm stat}$ was $\leq$ 1 km s^{-1} for components Aa, and Ab and $\leq$ 10 km s^{-1} for component B. The measurement of RVs of component B was more difficult, because the majority of metallic lines in its spectrum is very shallow and smeared out by the high rotational velocity of component B. The measurements also turned out to be very sensitive to the choice of the model and its discrepancies.

The telluric lines in the red and IR parts of the spectra were used to correct for the variations of the zero-point of the RV scale. Such corrections were typically ≤ 2 km s^{-1} for the Ondřejov spectra, hence all measurements for which the RV zero-point could not be checked this way were assigned uncertainty $\max(\Delta RV_{\rm stat}, 2)$ km s^{-1}, and the remaining ones were assigned uncertainty $\max(\Delta RV_{\rm stat}, 1)$ km s^{-1}, where 1 km s^{-1} is the upper bound of the precision of the zero-point correction for the Ondřejov spectra.

3.2. Direct analysis of RVs

Since we were not aware of any publicly available program for orbital solutions of hierarchical systems with apsidal advance of the outer orbit(s), JN has developed such a program. The measured RVs were fitted with a model, which takes into account the two dynamical interactions between the three or four components. The effects considered are the apsidal motion of orbit 2, and the light-time (LITE) effect produced by orbits 2 ($\mathbf{t}_{\rm LITE} \approx \mathbf{0.006}$ d) and 3 ($\mathbf{t}_{\rm LITE} \approx \mathbf{0.013}$ d). The RVs of the j-th component RV_j were fitted with the standard Keplerian model:

$$RV_j(t) = \sum_i K_i \left[\cos\left(\omega_i(t) + v_i(t)\right) + e_i \cos\omega_i(t)\right], \qquad (2)$$

where the index i goes over those orbits of ξ Tau, which are relevant for the motion of the j-th component of the ξ Tau system, K_i is the semiamplitude of the RV curve, ω_i the argument of periastron, v_i the true anomaly, e_i the eccentricity, and t is time. The light-time correction (LITE) $\Delta t_{\rm LITE}$ was computed **using the following formula**:

$$\Delta t_{\rm LITE,j}(t) = \sum_i \frac{P_i K_i \left(1-e_i^2\right)^{\frac{3}{2}}}{2\pi c} \frac{\sin\left[\omega_i(t) + v_i(t)\right]}{1 + e_i \cos v_i(t)}, \qquad (3)$$

where the index i goes over those orbits, which are hierarchically above that one, in which the j-th component lies (i.e over those, which produce LITE), P is the orbital period, and c the speed of light. Otherwise the notation is the same as for Eq. (2). The argument of periastron is a linear function of time $\omega_i(t) = \omega_i(t_0) + \dot\omega_i\,(t - t_{0,i})$, where $t_{0,i}$ is the reference epoch, $\dot\omega_i$ is the mean apsidal motion of the i-th orbit.

The model elements were optimised by searching the minimum of the following χ^2:

$$\chi^2 = \sum_{k=1}^{N_{\rm S}} \sum_{j=1}^{N_{\rm C}} \sum_{l=1}^{N_{\rm O}} \frac{1}{\sigma_{j,l}^2} \left[RV_j^{\rm OBS}(\tilde t_{j,l}) - RV_j^{\rm SYN}\left(\tilde t_{j,l}\right) - \gamma_k\right]^2, \qquad (4)$$

where the index k goes over $N_{\rm S}$ subsets of the measured RVs, which are defined in Table 2, the index j over $N_{\rm C}$ components of the ξ Tau system for which RVs were measured, and the index l goes over $N_{\rm O}$ individual measurements of the RV and $\tilde t$ is time corrected for the LITE. σ denotes individual rms of the RVs estimated with the procedure described in Sect. 2, $RV^{\rm OBS}$ the measured RV, $RV^{\rm SYN}$ the model RV computed with Eq. (2), and corrected for the LITE via Eq. (3), and γ denotes the systemic velocity. The minimum of χ^2 given by Eq. (4) was searched with the Sequential Least Squares routine (Kraft 1988).

As discussed above, RVs of component B are less accurate than those of components Aa, and Ab. Hence only RVs of the members of the eclipsing binary were fitted to obtain the majority of orbital elements. The individual subsets for individual types of the spectra gave very similar values of the systemic velocity (within 3σ), hence all available measurements were grouped together and a joint systemic velocity was derived for them. Once a final solution was obtained, the measurements were complemented with measurements of RVs of component B and the mass ratio q_2 was optimised (keeping the remaining parameters fixed). The parameters corresponding to the best-fit solution are listed in Table 5. RVs and the best-fitting model are plotted against time (to show the secular evolution of the periastron argument) for orbit 2 in Fig. 2, and against phase for orbit 1 in Fig. 3.

The uncertainties and correlations of individual parameters were estimated with the bootstrap method. 1 000 samples were randomly chosen from all available RVs. Each sample consists of the same number (748) of measurements as the original one (meaning that some measurements repeat within a sample). Each sample was fitted with an orbital model and the uncertainties were estimated from the distribution of the results.

The reduced chi-square (denoted $\chi^2_{\rm R}$ throughout the article) $\chi^2_{\rm R} \approx 2$, i.e. greater than ideal case of 1, is probably caused by: 1) variations of the RV zero-point larger than what we accounted for (we note that the estimate is based on the variations of the zero-point measured on the Ondřejov red spectra), 2) by the fact that the synthetic spectra need not correspond to the observed ones in all details, which is something which we cannot account for properly. 3) the model does not account properly for the dynamical interaction (see Sects. **8**, and 9) between all orbits.

We also fitted a model including orbit C fixed at the orbital elements given in Table 10. The reduced chi-square was only marginally ($\leq 1\%$) lower than that in Table 5. This is not surprising, since the semiamplitude of the RV caused by the revolution of the triple subsystem around the common centre of gravity with component C is ≈ 1 km s^{-1} and the LITE produced by that motion is $\approx \mathbf{0.013}$ d, i.e. both beyond the detection limit of our measurements.

3.3. Spectral disentangling

We were only able to disentangle the spectra in the vicinity of five major spectral lines Hα, Hβ, He I 4471 Å, Mg II 4481 Å, and Hγ, since only these regions were available for both the slit and echelle spectra. An attempt was made to disentangle the spectra of individual components using only the spectra from the three available echelle spectrographs. However, these disentangled spectra had strongly warped continua and were not helpful for further investigation.

The program KOREL (Hadrava 1995, 1997, 2009) (release 04-2004), which not only disentangles the spectra, but also fits the spectroscopic orbital elements, was used. This gave us the opportunity to compare the orbital solution obtained directly from the measured RVs with the result of KOREL. Only components B, Aa, and Ab were fitted, since component C is not detectable. Relative luminosities of all three components were kept constant during the orbital motion. This assumption, although not exactly satisfied because of the presence of shallow eclipses of components Aa and Ab, was necessary for the stability of the disentangling.

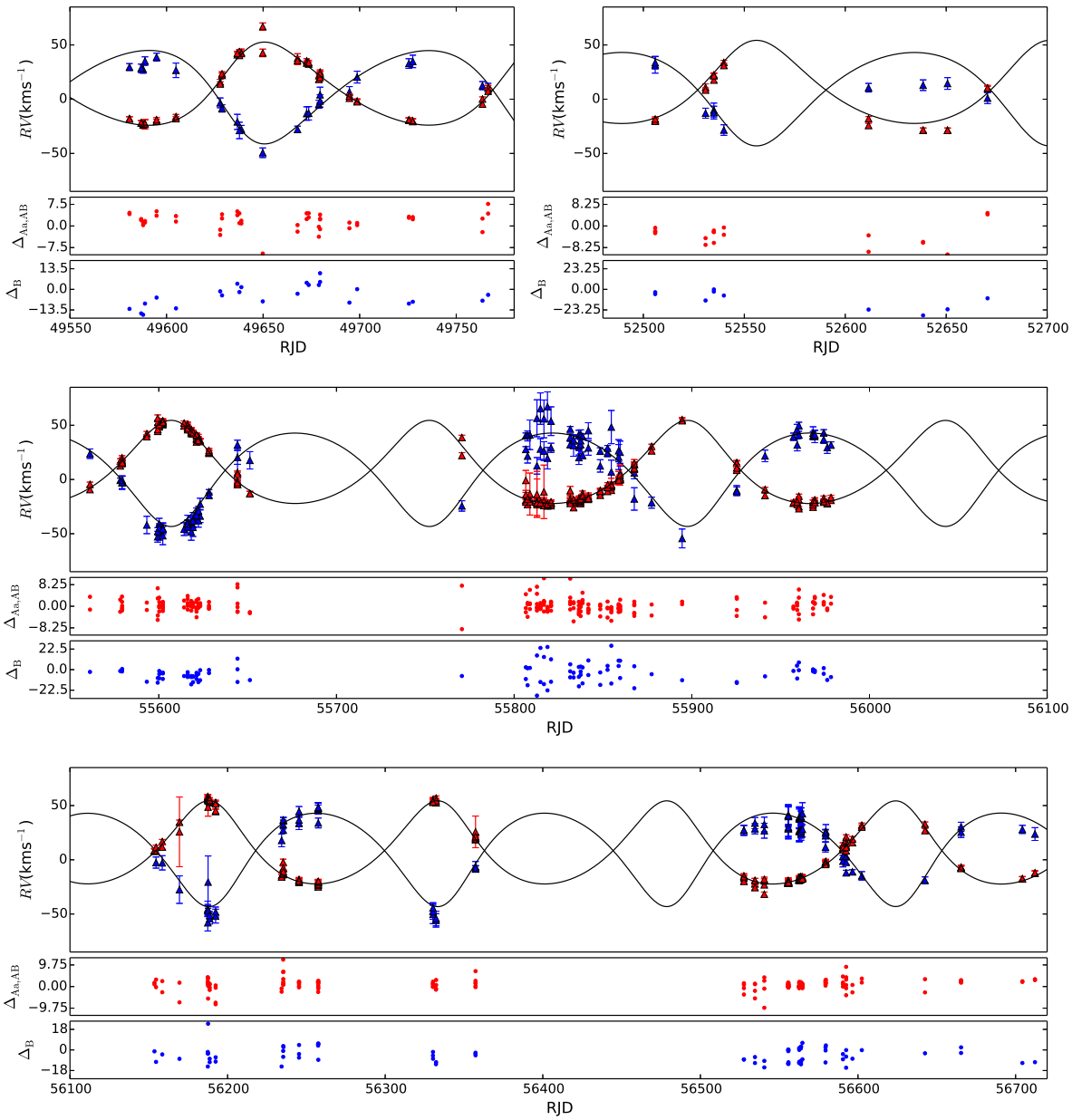

Fig. 2. RVs of the centre of gravity of the eclipsing binary (red triangles), and component B (blue triangles) against the best-fitting model (black) corresponding to parameters listed in Table 5. $\Delta_{\rm Aa,Ab}$ (in km s^{-1}) denote residuals of the fit for RVs of the centre of gravity of the eclipsing binary, and $\Delta_{\rm B}$ (in km s^{-1}) residuals of the fit for RVs of component B.

The orbital elements presented in Table 5 served as the starting estimates for the minimisation. The spectroscopic orbital elements obtained with KOREL are in Table 6. The disentangled profiles from the considered spectral regions are shown in Fig. A.1. KOREL does not provide the uncertainties of the fitted elements. Therefore a map of the χ^2 around the minimum found with the minimisation engine was drawn for every combination of two fitted parameters. The uncertainties, which are listed in Table 6 correspond to 68% confidence intervals (roughly one σ) estimated from these maps.

An attempt was carried out to disentangle lines of component C in two spectral bands in the near infrared, $\Delta\lambda_{\rm IR} = \{7750-7800, 8570-8800\}$ Å. The spectrum of component C was not detected in either of these bands. It was probably caused by the relatively low S/N of the echelle spectra in the infrared region and their limited number.

Table 5. Parameters of the two-orbit (1 and 2) fit given by Eqs. (2), and (3) to measured RVs. $P_{\rm AN}$ denotes the anomalistic period, $P_{\rm S}$ the sidereal period, $T_{\rm min}$ the epoch of the primary minimum of the light curve, $T_{\rm p}$ the epoch of the periastron passage.

El. Orb.	Units	Values 1	2
$P_{\rm AN}$	(d)	–	145.579±0.048
$P_{\rm S}$	(d)	7.14664±0.00002	145.113±0.071
$T_{\rm min}$	(RJD-56 220)	4.7067±0.0025	–
$T_{\rm p}$	(RJD-55 600)	–	9.46±0.52
K	(km s^{-1})	87.79±0.25	38.37±0.19
e		0.0[1]	0.2101±0.0053
q		0.9438±0.0036	0.889±0.056
ω	(deg)	90[1]	9.25±1.42
$\dot{\omega}$	(deg yr^{-1})	0.0[1]	2.90±0.33
N		748	
$\chi^2_{\rm R}$		2.128	
		Systemic velocity	
γ	(km s^{-1})	8.05 ± 0.18	

Notes. [1]The parameter was fixed. K_1 refers to the primary of the eclipsing binary $K^{\rm Aa}$, and K_2 to the centre of gravity of the eclipsing binary $K^{\rm Aa+Ab}$.

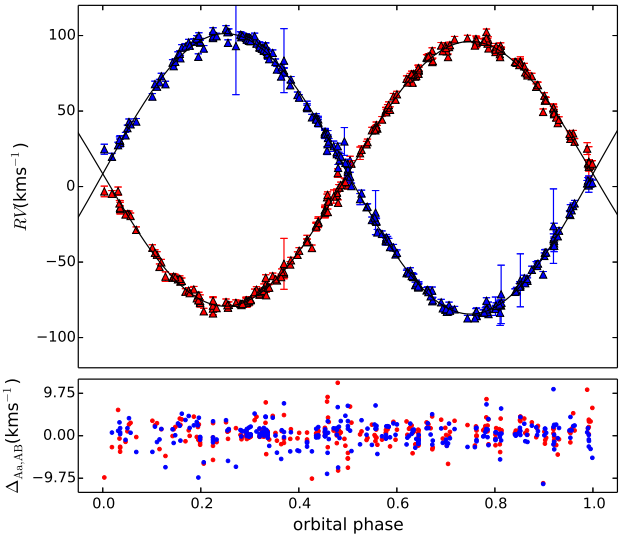

Fig. 3. RVs of components Aa (red), and Ab (blue) relative to the centre of gravity of the eclipsing binary against the best-fitting model (black) listed in Table 5. $\Delta_{\rm Aa,Ab}$ are residuals of the fit for components Aa, and Ab.

We also note that we tried to use the disentangled profiles instead of synthetic ones to measure RVs with the PYTERPOL program written by JN. This worked well for components Aa, and Ab, but not for component B. We suspect that it is so because the shape of the disentangled spectral lines depends on the orbital elements, for which the spectra were disentangled and vice versa. Hence the disentangled spectra partially "remember" the orbital elements, for which they were obtained and if used for the RV measurements, they would give a fine RV curve described by a solution close to these elements. This becomes a problem when one or more orbital elements suffer from a large uncertainty, which was the case for ξ Tau in the mass ratio of orbit 2.

Table 6. Orbital elements obtained by KOREL (spectra disentangling) for all available spectra containing at least one of the studied regions. The orbital model consists of orbits 1 and 2.

Elem. Orbit	Unit	1	2
$P_{\rm AN}$	(d)	–	145.612±0.056
$P_{\rm S}$	(d)	7.14664±0.00002	145.123±0.072
$T_{\rm min}$	(RJD-56220)	4.6963±0.0040	–
$T_{\rm p}$	(RJD-56000)	–	9.29±1.44
K	(km s^{-1})	87.52±0.59	37.55±0.57
e		0[1]	0.180±0.024
q		0.943±0.008	1.02±0.27
ω	(deg)	90[1]	8.52±4.1
$\dot{\omega}$	(deg yr^{-1})	0[1]	3.032±0.38
$\chi^2_{\rm R}$		1.19	

Notes. [1]The parameter was fixed. K_1 refers to primary of the eclipsing binary $K^{\rm Aa}$, and K_2 to the centre of gravity of the eclipsing binary $K^{\rm Aa+Ab}$.

3.4. Comparison of observed and synthetic spectra

JN has developed a Python program PYTERPOL[2], which interpolates in a pre-calculated grid of synthetic spectra to obtain estimates of the radiative properties of the components of multiple systems. For ξ Tau these parameters were the effective temperature $T_{\rm eff}$, gravitational acceleration $\log g$, the projected rotational velocity $v \sin i$, RV, and the relative luminosity $L_{\rm R}$. The parameters of components Aa, Ab, and B were covered by the POLLUX grid (Palacios et al. 2010) and component C was searched for using the AMBRE grid (de Laverny et al. 2012). Solar metallicity was assumed.

The fit was carried out in four spectral regions, but only three relative luminosities were derived, since two of the regions are very close to each other and the luminosities $L_{\rm R}$ are likely almost the same.

The spectral regions were:

1) $\Delta\lambda_1 = [4280, 4495]$ Å,

2) $\Delta\lambda_2 = [4815, 4940]$ Å, and

3) $\Delta\lambda_3 = \{[6330, 6390]\,; [6660, 6695]\}$ Å.

The relative luminosities were assumed to be constant over each spectral region $\Delta\lambda_i$.

Two of the regions contain a Balmer line, which constrains the gravitational acceleration of all three components, and a large number of metallic lines, which constrain the temperature, RVs, and the projected rotational velocities. 137 spectra from the Ondřejov Observatory were fitted together, since their normalisation is straightforward (a first order polynomial often suffices to fit the continuum), so that the Balmer lines are not affected by systematics often introduced by the rectification. The uncertainty of the relative flux was estimated from the continuum for each spectrum and set constant for each spectrum.

The bootstrap method was used to obtain an optimal set of parameters. 137 spectra were randomly drawn from the pool of 137 Ondřejov spectra (meaning that one or more spectra can be present multiple times within the random sample) and fitted. The

[2] A detailed description with a simple tutorial how to use it is at: https://github.com/chrysante87/pyterpol/wiki

Table 7. Parameters of the fit of the synthetic spectra to 137 observed Ondřejov spectra. The modelled spectral intervals are: $\mathbf{\Delta}\lambda_\mathbf{1} = [4280, 4495]$Å, $\mathbf{\Delta}\lambda_\mathbf{2} = [4815, 4940]$Å, $\mathbf{\Delta}\lambda_\mathbf{3} = \{[6330, 6390]\,; [6660, 6695]\}$Å.

Parameter	Unit	Value		
Component		B	Aa	Ab
$T_{\rm eff}$	(K)	14 190±150	10 700±160	10 480±130
$\log g$	(cgs)	4.527±0.041	4.08±0.12	4.01±0.10
$v \sin i$	(km s^{-1})	229.2±1.7	12.6±2.6	14.3±3.1
$L_{\rm R}^{\Delta\lambda_1}$		0.660±0.024	0.179±0.018	0.165±0.022
$L_{\rm R}^{\Delta\lambda_2}$		0.688±0.026	0.162±0.024	0.155±0.027
$L_{\rm R}^{\Delta\lambda_3}$		0.665±0.036	0.173±0.028	0.161±0.031
$\chi^2_{\rm R}$			0.87	

initial set of parameters was randomly chosen from intervals[3] which were established from the first trial fits. The initial RVs were estimated from the orbital solution presented in Nemravová et al. (2013) and randomly put slightly off (within 30 km s^{-1} vicinity of the estimate) to secure robustness of the final solution. The procedure was repeated five hundred times and the final set of parameters was estimated from the distribution of the results. The shape of the distribution was Gaussian-like, i.e. describable with a mean value and its standard deviation. The results are presented in Table 7.

A comparison of four spectral regions with the model is shown in Fig. 4. The reduced $\chi^2_{\rm R}$ is lower than one, indicating that we have slightly overestimated the uncertainty of the relative flux of the observed spectra.

3.5. Comparison of synthetic and disentangled spectra

Disentangled spectra corresponding to the solution of Table 6 were fitted with the interpolated synthetic spectra to check on the results of Sect. 3.4. The program PYTERPOL was again used. The following spectral regions were fitted:

$\mathbf{\Delta}\lambda_\mathbf{1} = \{[4280, 4400]\,; [4455, 4495]\}$ Å,
$\mathbf{\Delta}\lambda_\mathbf{2} = [4765, 4970]$ Å,
$\mathbf{\Delta}\lambda_\mathbf{3} = \{[6325, 6395]\,; [6510, 6620]\,; [6655, 6695]\}$Å.

The parameters corresponding to the best-fitting synthetic spectra are listed in Table 8. The optimal parameters were estimated with a MCMC simulation and the uncertainties reflect only the statistical part of the uncertainty. The systematic uncertainty — the warp in the continua and the need for its normalisation — cannot be easily quantified and is responsible for the extremely high reduced $\chi^2_{\rm R}$ along with the very high S/N ratio of the disentangled spectra. Therefore the uncertainties of parameters listed in Table 8 are very likely underestimated.

This systematic effect corrupts the estimate of $\log g$ of all components, especially component B, where the warping was the most pronounced; therefore applies as well to the rotational velocity of component B. The rotational velocity of components Aa, and Ab is affected strongly by the choice of the instrumental broadening which is very difficult to estimate for disentangled spectra and was set to 0.2 Å. The total light is also very likely affected by the re-normalisation, which (necessarily) changes the depths of spectral lines (one can see that $L = \sum_{i=1}^{3} L_{\rm R}^{\Delta\lambda,i} \neq 1$ for all studied bands).

Bearing all this in mind, we state that this result does not contradict, but rather supports that obtained by fitting of synthetic to observed spectra. A comparison of the synthetic spectra corresponding to the parameters listed in this Sect., disentangled spectra and re-normalised disentangled spectra is in Fig. A.1.

Table 8. Parameters of synthetic spectra best-fitting the disentangled spectra. γ denotes the systemic velocity of ξ Tau. The fit is plotted in Fig. A.1.

Element	Unit	Value		
		Component		
		B	Aa	Ab
$T_{\rm eff}$	(kK)	14.07(14)	10.26(14)	10.050(80)
$\log g_{\rm [cgs]}$		3.99(4)	4.06(9)	4.02(4)
$v \sin i$	(km s^{-1})	253.6(16)	18.6(12)	10.2(10)
$L_{\rm R}^{\Delta\lambda_1}$		0.758(8)	0.168(3)	0.150(7)
$L_{\rm R}^{\Delta\lambda_2}$		0.711(6)	0.191(5)	0.149(3)
$L_{\rm R}^{\Delta\lambda_3}$		0.686(7)	0.188(4)	0.161(7)
γ	(km s^{-1})		8.1(27)	
$\chi^2_{\rm R}$			31.58	

4. Photometry

The preliminary analysis published in Nemravová et al. (2013) has shown that the light variations can be attributed to the eclipses of components Aa and Ab of orbit 1. They partially eclipse each other and produce two very narrow and nearly identical minima, which are only ≈ 0.1 mag deep in the Johnson V passband.

In addition to the binary eclipses, our new, very precise MOST satellite observations unveiled persistent low-amplitude rapid cyclic light changes, which are likely to be associated with component B, since they remain to be present during both binary eclipses. The MOST light curve also allows the determination of very accurate radii of components Aa and Ab and the detection of variations of the mean motion of the eclipsing pair. The zoomed parts of both minima of the MOST light curve are shown in Fig. 5.

4.1. The period analysis of the light curve

Our first goal in the analysis of the MOST light curve was to unveil the nature of the rapid cyclic low-amplitude changes. Two different methods were used to construct and investigate periodogram of the light curve. The first one is based on the Fourier

[3] The intervals are the following: $T_{\rm eff}^{\rm B} \in [13\,000, 14\,500]$ K, $T_{\rm eff}^{\rm Aa} \in [9\,000, 11\,500]$ K, $T_{\rm eff}^{\rm Ab} \in [9\,000, 11\,500]$ K, $\log g^{\rm B} \in [4.0, 5.0]$, $\log g^{\rm Aa} \in [3.5, 4.5]$, $\log g^{\rm Ab} \in [3.5, 4.5]$, $v \sin i^{\rm B} \in [200, 250]$ km s^{-1}, $v \sin i^{\rm Aa} \in [0, 40]$ km s^{-1}, $v \sin i^{\rm Ab} \in [0, 40]$ km s^{-1}, $L_{\rm R}^{\rm B} \in [0.55, 0.8]$, $L_{\rm R}^{\rm Aa} \in [0.10, 0.25]$, $L_{\rm R}^{\rm Ab} \in [0.10, 0.25]$.

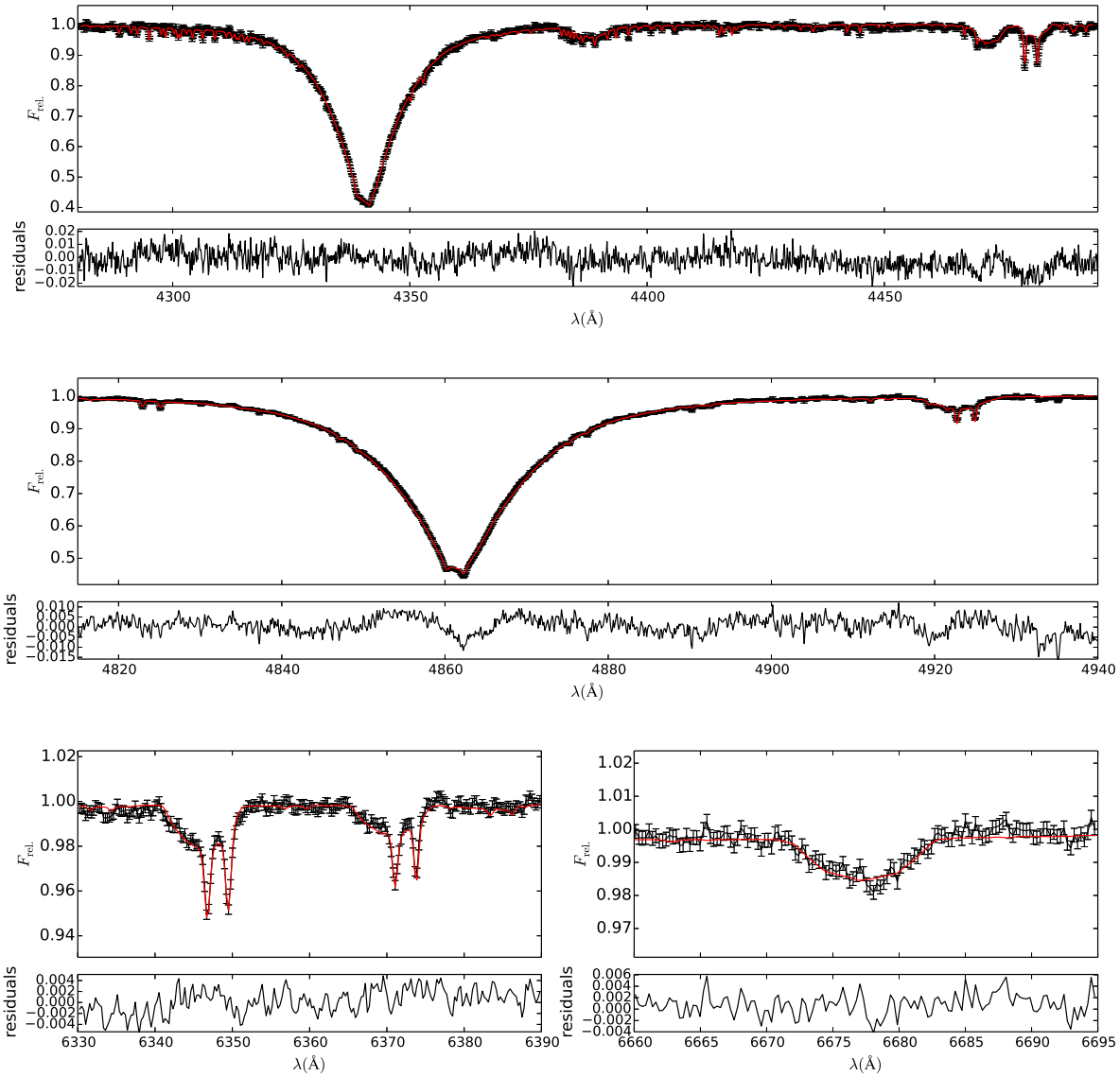

Fig. 4. Example of the fit of the synthetic spectra (red) to three observed spectra (black) in spectral regions: 1) $\mathbf{\Delta\lambda_1} = [4280, 4495]$ Å (top), 2) $\mathbf{\Delta\lambda_2} = [4815, 4940]$ Å (middle), 3) $\mathbf{\Delta\lambda_3} = [6330, 6390]$ Å (bottom, left), 4) $\mathbf{\Delta\lambda_3} = [6660, 6695]$ Å (bottom, right). The synthetic spectra are given by parameters listed in Table 7.

transform (FT hereafter), and is implemented in the program PERIOD04 (Lenz & Breger 2004). The second one uses the phase dispersion minimisation technique (PDM) (Stellingwerf 1978) and is implemented in the program HEC27[4]. The periodogram of the whole light curve is dominated by the orbital period of the eclipsing binary $P_1 \approx 7.147$ d. In order to study the rapid low-amplitude oscillation we removed the eclipses (see Fig. 7, top).

The periodogram of the rapid oscillations (see Fig. 6) shows a basic frequency of $f_0 = 2.38\,\mathrm{d}^{-1}$, most likely due to rotation of component B, the first harmonics of the eclipsing binary orbital frequency $f_1 = 2/P_1 = 0.279\,\mathrm{d}^{-1}$; the frequencies of $f_\mathrm{d} = 1.002738\,\mathrm{d}^{-1}$ and $f_\mathrm{MOSTorbit} = 14.2\,\mathrm{d}^{-1}$ are instrumental (i.e. the orbital frequency of the satellite). The remaining prominent frequencies $f_\mathrm{alias} = \{15.1734, 17.5385, 28.3896, 42.5825, 56.7745, 70.9720\}\,\mathrm{d}^{-1}$. seem to be either integer multiples of f_orb or its splittings with f_0 or f_d. Remaining peaks (e.g. $f = 87.1609\,\mathrm{d}^{-1}$) have relatively low S/N ratios. We are not aware of any instrumental effect, which would induce oscillations at $f_0 = 2.38\,\mathrm{d}^{-1}$, hence the low-amplitude variations arise from a physical process in ξ Tau.

[4] The program and a short user's guide are available at http://astro.troja.mff.cuni.cz/ftp/hec/HEC27.

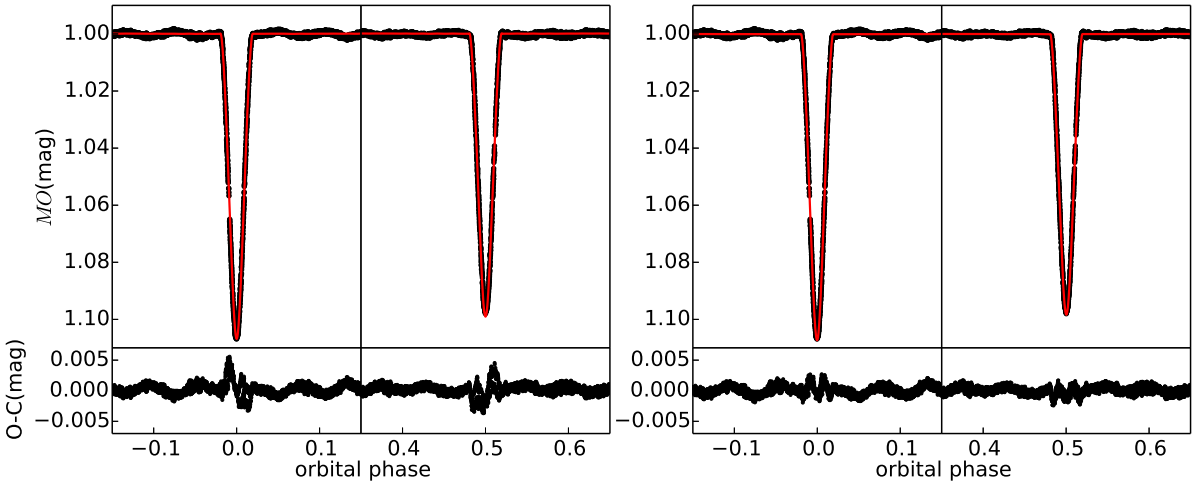

Fig. 5. Fit of the light curve from the satellite MOST. Only the light curve minima and their surroundings are shown. The primary (secondary) minimum is on the left (right) on each panel. The left panel corresponds to the global circular solution $e_1 = 0.0$ and to orbital period $P_1 = 7.14664$ d. The right panel corresponds to a local solution, where small adjustment of the eccentricity and the orbital period was allowed. MO denotes the satellite broad-band filter.

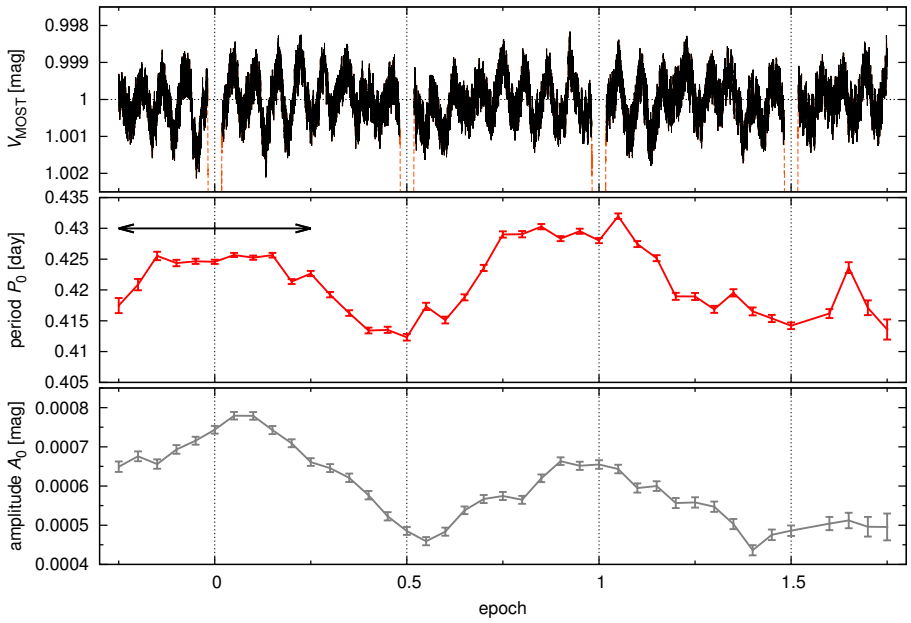

Fig. 7. The normalised light curve as reduced from MOST photometry, but without intervals of primary and secondary eclipses (top panel), together with the corresponding period P_0 (middle) and amplitude A_0 (bottom) of the harmonic function $f(t) = 1 + C_0 + A_0 \sin[2\pi(t - T_0)/P_0 + \phi_0]$, which was sequentially fitted to the light curve, always in limited intervals $\Delta E_1 = 0.5$ of the epoch (indicated by the black double arrow), shifted with a step $\Delta E_2 = 0.05$. We can see that the oscillations exhibit both frequency and amplitude modulations, with periods spanning $P_0 = (0.42 \pm 0.01)$ d and amplitudes $A_0 = (0.00060 \pm 0.00015)$ mag. It seems that the longest P_0 and the largest A_0 are observed at around primary eclipses and *vice versa*.

A closer look at Fig. 7 shows that the amplitude of the curve varies. To quantify these changes a harmonic function $f(t) = 1 + C_0 + A_0 \sin[2\pi(t - T_0)f_0 + \phi_0]$ was sequentially fitted to segments of the light curve $\Delta t_1 = P_1/2$ d wide, and shifted with a step $\Delta t_2 = P_1/20$, where P_1 is the period of the eclipsing binary. The scan revealed that both the basic frequency f_0 and its amplitude A_0 vary on the time-span of two orbital periods of the eclipsing binary (see Fig. 7, middle and bottom panels).

4.2. On the nature of quasiperiodic oscillations

The quasiperiodic oscillations clearly visible in the MOST light curve — with an approximate period $P_0 \simeq (0.42 \pm 0.01)$ d and an amplitude $A_0 = (0.00060 \pm 0.00015)$ mag — exhibit both a frequency (FM) and an amplitude modulation (AM) on the time-span of about the two shortest orbital periods P_1 (see Fig. 7). We can think of several possibilities regarding their origin: (i) an instrumental effect, (ii) a fifth component and ellipsoidal variations, (iii) rotation with spots, (iv) rotation and pulsations.

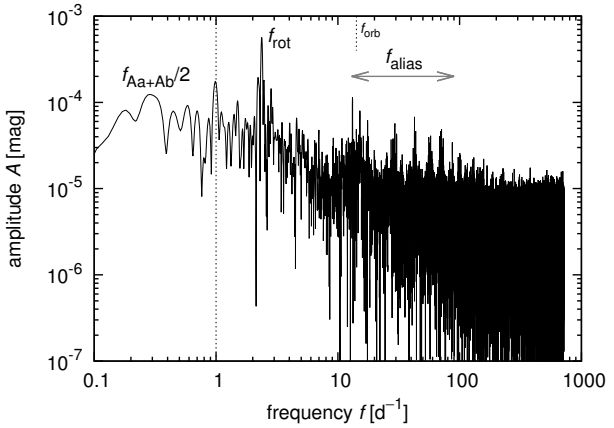

Fig. 6. The Fourier spectrum of the MOST light curve from Fig. 7 (i.e. outside eclipses). Prominent frequency peaks are marked (see their description is Sect. 4.1).

The option (i) does not seem very likely though, because we do not know about any instrumental period of $0.42\,\mathrm{d}$ (like 1 day, or satellite orbital period 0.07042 d in this case).

A hypothetical fifth component (option ii) orbiting either component B, Aa or Ab with a period $2P_0$ can induce ellipsoidal variations of the order of A_0, but they should be pretty regular (without large AM, FM) and moreover manifest themselves in one of the RV curves too, which is not the case. We do not see any peak in the Fourier spectrum at $f_0 = 1/P_0 = 2.38\,\mathrm{d}^{-1}$, even though the Nyquist frequency for our spectroscopic dataset is $f_{\mathrm{Ny}} = 7.1\,\mathrm{d}^{-1}$. Nevertheless, the coverage and cadence are not uniform at all and the expected amplitude is small ($5\,\mathrm{km\,s}^{-1}$), which makes this particular argument weak. We would also expect to see some frequency modulation due the (classical) Doppler effect, $P'_{\mathrm{obs}} = (1 - \frac{v}{c})\gamma P_{\mathrm{src}}$, with $v \simeq 2v_{\mathrm{kepl}}$. However, for $0.423\,\mathrm{d}$ we would only get a change by $0.001\,\mathrm{d}$, which is one order of magnitude smaller than the observed total variation.

Regarding the rotation, the lower limit for its period is the critical rotation, $P_{\min} = 2\pi(GM/R^3)^{-1/2}$, and the upper limit is determined by rotational broadening, $P_{\max} = 2\pi R/(v \sin i)$ (cf. Table 8). For component Aa or Ab the admissible range is from about $P_{\mathrm{rot}} = 0.180\,\mathrm{d}$ to $3.85\,\mathrm{d}$; for component B 0.325 to $0.634\,\mathrm{d}$. The observed oscillations are within both ranges, so that we cannot distinguish the source component at this point. One can argue that small axial inclination for components Aa, Ab is unlikely when their orbital inclination is large, so that their true $P_{\mathrm{rot}} > P_0$. We thus prefer to attribute these oscillations to component B. Additionally, this star is relatively brighter so that it is 'easier' to induce the oscillations of given amplitude A_0.

It seems difficult to distinguish between spots and pulsations (options iii and iv; as in Degroote et al. 2011). Especially for early-type stars, spots are not that common, unless a star is chemically peculiar or magnetically active (Bp), but we have no observations and analyses at our disposal which could prove or disprove this for ξ Tau.

Pulsating B stars (like β Cep, SPB) always exhibit a low-frequency signal corresponding to the rotation and then a series of pulsation modes, either pressure (high-frequency) or gravity (low-frequency). The cadence of MOST photometric observations allows us to compute the Fourier spectrum up to $f_{\mathrm{Ny}} = 719\,\mathrm{d}^{-1}$, corresponding to $0.00139\,\mathrm{d} = 2\,\mathrm{min}$ (Fig. 6). Unfortunately, apart from the basic rotational period, its aliases with the orbital period P_1 of the eclipsing binary, 1-day and P_{orb} instrumental periods, we cannot unambiguously detect any pulsation modes with signal-to-noise ≥ 5, to say nothing about rotational splittings which would be conclusive.

4.3. Eclipse timing variations

The orbital period of the eclipsing binary $P_1 = 7.14664\,\mathrm{d}$ introduces a small but clearly detectable shift $\Delta_{\mathrm{PHASE}} \approx 0.0003$ between the two minima recorded with the MOST satellite. The shift disappears if the orbital period and the eccentricity are optimised. The local period and eccentricity, which do not cause the phase shift, are $P_1 = 7.14466\,\mathrm{d}$, $e_1 \simeq 0.002$. The problem is illustrated in Fig. 5, where the comparison of an eccentric model with local value of the orbital period and a global circular model is shown. Even larger phase shift $\Delta p \sim 0.004$ was detected when similar analysis was carried out for all photometric observations.

This led us to investigate the eclipse timing variations (ETVs) in all available photometry, divided into subsets covering time intervals shorter than $P_2/4$ (individual minima are shown in Figs B.1, and B.2). The ETVs are very noisy and the delays themselves have an amplitude $\Delta t_{\mathrm{OBS}} \approx 0.025 \pm 0.01\,\mathrm{d}$, which cannot be explained by LITE ($\Delta t_{\mathrm{LITE}} \approx 0.006\,\mathrm{d}$). Moreover, they seem to vary on a time scale comparable to the orbital period P_2. Hence we suspected the dynamical interaction between orbits 1 and 2 to be the reason for these delays. The first order model of the physical delay (Eq. 8 from Rappaport et al. 2013), which is only a part of the total ETV, arising from dynamical interaction of two orbits in hierarchical triple systems gives an estimate of the amplitude of the effect $\Delta t_{\mathrm{MODEL}} \approx 0.02\,\mathrm{d}$, (i.e. in rough agreement with the detected value). This is another proof of the dynamical interaction in ξ Tau (the first is the apsidal motion reported by Nemravová et al. 2013) and led us to development of an N-body model (see **Sect. 8**) and a perturbation theory (see Sect. 9).

4.4. A global orbital model for all light curves

The program PHOEBE 1.0 (Prša & Zwitter 2005, 2006) was used to derive the light-curve solution. The mass ratio q_1 was taken from the analysis of the RVs (see Table 5), because only light curves were modelled and those do not constrain the mass ratio for a detached system. The eccentricity was assumed to be $e_1 = 0.0$ **(although Sect. 8 shows that the orbit 1 is slightly eccentric).** The value of the semi-major axis a was adjusted after each iteration based on $a_1 \sin i$ given by the fit of the directly measured RVs (see Table 5). The linear limb-darkening law was adopted and the coefficients were interpolated in a precalculated grid distributed along with PHOEBE. The bolometric albedos were taken from Claret (2001) and the gravity brightening coefficients from Claret (1998) for the corresponding temperatures of components of the eclipsing binary. The spin-orbit synchronisation, i.e. the synchronicity ratios $F^{\mathrm{Aa}} = F^{\mathrm{Ab}} = 1$, was assumed[5]. The primary effective temperature $T_{\mathrm{eff}}^{\mathrm{Aa}}$ was set to the value found through a comparison of synthetic and observed spectra.

The orbital inclination i_1, Kopal surface potentials $\Omega_{\mathrm{K}}^{\mathrm{Aa}}, \Omega_{\mathrm{K}}^{\mathrm{Ab}}$ of both components, and the epoch of the primary minimum $T_{\mathrm{min},1}$, the secondary temperature $T_{\mathrm{eff}}^{\mathrm{Aa}}$, and the relative lumi-

[5] The radii R^{Aa} and R^{Ab} from Nemravová et al. (2013) and rotational velocities from Table 7 give synchronicity ratios $F^{\mathrm{Aa}} = 1.12 \pm 0.26$, and $F^{\mathrm{Ab}} = 0.74 \pm 0.20$; the deviations from the corotation are small and probably arise from an incorrect determination of the radii.

nosity of component B $L^{\rm B}$ in each spectral band were optimised. Initial estimates of these parameters were taken from (Nemravová et al. 2013), initial relative luminosities $L^{\rm B}$ of component B were estimated from the comparison of synthetic and observed profiles (Table 7). The primary luminosities $L^{\rm Ab}$ were adjusted after each iteration.

The fitting was carried out in the Python environment of `PHOEBE` and the minimum was searched with the differential evolution algorithm (Storn & Price 1997). A large portion of the parametric space was searched[6]. The parametric space was densely sampled with models during the fitting ($\approx 300\,000$ light curve models were computed). This showed that the relative luminosity of component B $L^{\rm B}$ is poorly constrained.

After a global minimum was found, we split our data and optimised the ephemeris, relative luminosity of component B, and surface potentials using only observations from the MOST satellite, after which we optimised the effective temperature of component Ab, and relative luminosity of component B, using the Johnson UBV photometry. The epoch of the primary minimum was also fitted for the UBV dataset to adapt slightly for the ETVs discussed in Sect. 4.3.

The parameters corresponding to the best-fitting model are listed in Table 9. Our model is unable to account for either the rapid light oscillations or the ETVs; therefore we raised the uncertainty of observations from the MOST satellite to deal with the former ($\Delta m_{\rm MOST} = 0.006$ given by the sinusoidal fit). The uncertainties of parameters are estimated as 68 % confidence intervals computed from a scaled χ^2 (scaled to an ideal situation, where the reduced chi-square $\chi^2_{\rm R} = 1$), although in this case the scaling was almost unnecessary, since the reduced chi-square of the best solution is $\chi^2_{\rm R} = 1.134$.

Table 9. Parameters of the best-fitting circular orbital model obtained with the program `PHOEBE 1.0`. All available photometric observations were fitted. $\Omega_{\rm K}$ denotes the Kopal surface potential here, and L the relative luminosity in the filter given by the subscript. U, B, and V denote Johnson filters, MO denotes the broad-band filter in the MOST satellite, and Hp denotes the broad-band filter of the satellite Hipparcos.

Element	Unit	Value	
		Orbital properties	
P	(d)	7.14664±0.00010	
$T_{\rm min}$	(RJD)	56 224.72482±0.00022	
a	($R_\odot$)	25.552±0.097	
q		0.9439[1]	
e		0.0[1]	
i	(deg)	86.85±0.22	
ω	(deg)	90	
		Component properties	
Comp.		Aa	Ab
$T_{\rm eff}$	(K)	10 700[1]	10 450±150
$\Omega_{\rm K}$		15.97±0.25	15.93±0.32
$L_{\rm V}$		0.204±0.020	0.174±0.017
$L_{\rm B}$		0.196±0.021	0.165±0.018
$L_{\rm U}$		0.157±0.012	0.130±0.010
$L_{\rm MO}$		0.203±0.008	0.162±0.006
$L_{\rm Hp}$		0.212±0.023	0.180±0.020
		Passband luminosity of component B	
$L^B_{\rm V}$		0.622±0.060	
$L^B_{\rm B}$		0.639±0.069	
$L^B_{\rm U}$		0.713±0.071	
$L^B_{\rm MO}$		0.634±0.024	
$L^B_{\rm Hp}$		0.608±0.067	
$\chi^2_{\rm R}$		1.134	

Notes. [1] The parameter was kept fixed.

5. Astrometry of orbit 3

We used the existing astrometric positions listed in the WDS catalogue (see Mason et al. 1999, and references therein) to improve the orbital elements of orbit 3 published by Rica Romero (2010). The solution was carried out with the help of the program written by PZ (see Zasche & Wolf 2007, and references therein). The solution is in Table 10 and the orbit is shown in Fig. 8.

Table 10. Orbital elements of orbit 3 based on a fit to astrometric measurements published in WDS. The listed parameters are the orbital period P, the periastron epoch $T_{\rm p}$, the eccentricity e, the semimajor axis a, the inclination i, the argument of the periastron ω, the position angle of the nodal line Ω.

Element	Unit	Value
P	(yr)	51.01±0.78
$T_{\rm p}$	(RJD)	54 615±251
e		0.5728±0.0028
a	(mas)	441.5±2.4
i	(deg)	25.4[1]±7.7
ω	(deg)	10.6±8.9
Ω	(deg)	106.4±2.2

Notes. [1] The inclination is determined ambiguously. A solution with $i = -25.4$ deg has exactly the same χ^2.

6. Spectro-interferometry

In this Sect. we present an orbital analytic model of the ξ Tau system, which we fit to spectro-interferometric observations to estimate orbital elements, radii, and fractional luminosities of ξ Tau.

6.1. A global model for all available spectro-interferometric observations

The calibrated visibilities from VEGA/CHARA were fitted night-by-night with a model consisting of three uniform disks using the tool LitPro[7] (Tallon-Bosc et al. 2008). The observations obtained during each single night were not numerous enough to safely estimate the positions and radii of components Aa, Ab, and B on the celestial sphere[8].

To circumvent the problem we created a global orbital model, which computes instantaneous positions of compo-

[6] Following parametric space was searched: $T_{\rm min,1} \in [56\,224.68, 56\,224.78]$ **RJD**, $i_1 \in [84, 90]$ deg, $\Omega_{\rm K}^{\rm Aa} \in [11, 20]$, $\Omega_{\rm K}^{\rm Ab} \in [11, 20]$, $T_{\rm eff}^{Ab} \in [10\,000, 10\,700]$ K, $L^{\rm B} \in [0.55, 0.78]$. The last interval applies to each studied spectral filter (U, B, V, MOST).

[7] LITpro software available at `http://www.jmmc.fr/litpro`

[8] In contrast to it, the NPOI observations are numerous enough to provide good estimates of the relative position of component B and the photocentre of the eclipsing binary for each night. They are presented in Table C.1 along with details on their acquisition – see Appendix C.

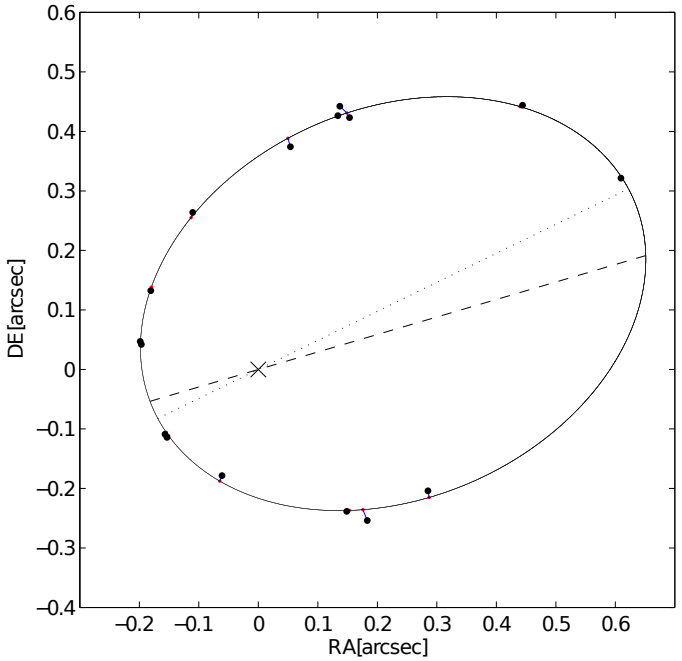

Fig. 8. The speckle-interferometric outer orbit 3 corresponding to the solution of Table 10. The dotted line stands for the line of apsides, while the dashed line for the line of nodes.

nents B, Aa, and Ab with the following formulæ:

$$\alpha_i(t) = \arctan\left(\tan\left(v_i(t)+\omega_i(t)\right)\cos i_i\right)+\Omega_i, \quad (5)$$

$$\rho_i(t) = a_i\frac{1-e_i^2}{1+e_i\cos v_i(t)}\frac{\cos\left(\omega_i(t)+v_i(t)\right)}{\cos\left(\alpha_i(t)-\Omega_i\right)}, \quad (6)$$

$$x_i = \rho_i \sin\alpha_i, \quad (7)$$

$$y_i = \rho_i \cos\alpha_i, \quad (8)$$

where index i denotes the component of a binary, v is the true anomaly, ω the argument of periastron, i the orbital inclination with respect to the celestial sphere, Ω is the position angle of the nodal line, a the angular semimajor axis, e the eccentricity. The position angle α_i is measured counter-clockwise from the North direction and ρ_i is the angular separation of a component and the centre of mass, (x_i, y_i) is the same in Cartesian coordinates. The instantaneous value of the argument of periastron is given as follows: $\omega(t) = \omega_0 + \dot{\omega}\,(t - T_\mathrm{p})$, where T_p is the reference periastron epoch and ω_0 is the value of the periastron argument at the reference epoch. Instead of computing the semimajor axis for each component of a binary, the semimajor axis a and the mass ratio $q = M_1/M_2$ are used; the semimajor axes of primary and secondary can be computed with the following formulæ: $a_1 = aq/\,(1+q)$, $a_2 = a/\,(1+q)$. The periastron argument of the secondary is $\omega_2 = \omega_1 + \pi$.

In our application of Eqs. (5) – (8) component B is fixed at the beginning of the coordinate system, because the observations are sensitive to relative positions of the stars only, not the system as whole.

Once positions of all three components are known, objects representing each component can be placed at these positions. The uniform disk was chosen, because all three components are detached and so only minor departures from the spherical symmetry can be expected. The squared visibility V^2 and closure phase $T_3\phi$ for such a model can be computed analytically with the following formulæ:

$$|V_{\mathrm{S},k}(\mathbf{f})|^2 = \left|\frac{\sum_{j=1}^{N} L_{j,k}\frac{2J_1(\pi\theta_j B/\lambda_k)}{\pi\theta_j B/\lambda_k}e^{-2\pi i(\mathbf{f}\cdot\mathbf{r})}}{\sum_{j=1}^{N} L_{j,k}}\right|^2, \quad (9)$$

$$T_3\phi_{\mathrm{S},k}(\mathbf{f}_1,\mathbf{f}_2) = \arg\left[V_{\mathrm{S},k}(\mathbf{f}_1)V_{\mathrm{S},k}(\mathbf{f}_2)V_{\mathrm{S},k}(-\mathbf{f}_1-\mathbf{f}_2)\right], \quad (10)$$

where index j denotes a component of the triple system, k the spectral band, V the visibility, $\mathbf{f} = (u, v)$ the spatial frequency, L the luminosity fraction, B the length of the baseline, θ the diameter of the uniform disk, λ the effective wavelength (the central wavelength of the spectral band), J_1 the first-order Bessel function, $\mathbf{r} = (x_j, y_j)$ the Cartesian coordinates of a component computed with Eqs. (5)–(8), and N the total number of components in the system. The uniform disk diameter θ is also a wavelength-dependent quantity, so a different radius should be derived for each spectral band. Nonetheless the dependency is very weak (order of 10^{-3} for the whole wavelength span of our data).

6.2. An orbital solution for all available spectro-interferometric observations

The model given by Eqs. (5) – (10), was fitted to calibrated squared visibilities from all **four** instruments, i.e. CHARA/VEGA, NPOI, MARK III, and **VLTI/AMBER**. The optimal set of parameters was searched using the least squares method, i.e. by minimising the following chi-square:

$$\chi^2 = \sum_{k=1}^{N_\mathrm{F}}\sum_{j=1}^{N_\mathrm{V}}\left|\frac{|V_k|^2(\mathbf{f}_j)-|V_{\mathrm{S},k}|^2(\mathbf{f}_j)}{\sigma_k(\mathbf{f}_j)}\right|^2 + \sum_{k=1}^{N_\mathrm{F}}\sum_{j=1}^{N_\mathrm{T}}\left|\frac{T_3\phi_k(\mathbf{f}_{1,j},\mathbf{f}_{2,j})-T_3\phi_{\mathrm{S},k}(\mathbf{f}_{1,j},\mathbf{f}_{2,j})}{\sigma_k(\mathbf{f}_{1,j},\mathbf{f}_{2,j})}\right|^2 \quad (11)$$

where V^2 ($T_3\phi$) is the observed squared visibility (the observed closure phase), V_S^2 ($T_3\phi_\mathrm{S}$) the synthetic squared visibility computed with Eq. (9) (the synthetic closure phase, Eq. 10), $\mathbf{f} = (u, v)$ the spatial frequency, σ the standard deviation of **an** observation, N_V the total number of squared visibility observations, N_T the total number of closure phase observations, and N_F the total number of spectral bands.

The phase coverage of the inner and the outer orbits is good enough (see Fig. 1) to allow fitting of all orbital elements. Our strategy was to keep as many parameters free as possible, since this model is independent of those presented in Sects. 3, and 4. However, the angular size of the inner orbit is small and its ephemeris is obtained with greater precision by the photometry and spectroscopy. The eccentricity of orbit 1 was set to zero (see Table 5), because there were no signs of a significant eccentricity in previous analyses. A number of trial runs have shown that the inclination i_1, and the mass ratio q_1 are poorly constrained by the interferometric observations. If optimised, both converged to values not consistent with previous analyses ($i \approx 78 \pm 5$ deg, $q_1 = 0.8 \pm 0.10$). Investigation of chi-square maps surrounding these values, have shown large shallow valleys, which spread up to regions having values consistent with photometric and spectroscopic models. To stay on the safe side we fixed both parameters at values obtained from the spectroscopy and photometry, because they were estimated with much higher precision.

The global minimum of Eq. (11) was searched with the differential evolution algorithm (Storn & Price 1997) and locally

optimised with the sequential least squares routine (Kraft 1988). The parameters of the best-fitting model are listed in Table 11. A large portion of the parametric space was searched.[9] The initial parametric space was equally sampled with a population which consisted of 1 500 members. The population evolved until the mean energy of the population (i.e. the mean chi-square divided by its standard deviation and multiplied by the tolerance) was greater than one. The tolerance was set to 10^{-3} and the procedure took from 50 to 100 iterations to finish.

The final reduced $\chi^2_{\rm R} \approx 5.806$ is much larger than 1 because: 1) underestimation of the true uncertainty of the V^2 derived with the reduction pipeline, because the high $\chi^2_{\rm R}$ is given mainly by data which were acquired at low spatial resolution and should be easiest to reduce, 2) the angular slit width of all interferometric instruments is comparable to the angular separation of component C and the triple, i.e. it cannot be guaranteed that it was recorded. The full amplitude of squared visibility variations caused by component C ranges from 0.035 in the V band to 0.050 in the K band. It introduces systematic errors, which we cannot correct, and 3) imperfections of the model — we had to accept several simplifications in order to stabilise the fit. Uncertainties of the best-fit parameters were estimated as $68\,\%$ confidence intervals from the $\chi^2_{\rm R}$ scaled to one.

Several attempts have shown that we are insensitive to diameters of components Aa and Ab, because we lack enough observations at very long baselines (reaching up to 300 m). If they were set free, the solution then converged to unrealistic values ($\gtrsim 1.0$ mas), so they had to be fixed at values given by the parallax of the system and the light curve solution (see Table 9). Convergence of orbital parameters of orbit 1 was in general slow, because the bulk of observations (NPOI, AMBER) were taken at low spatial resolution, at which this orbit is almost mainly on observations from VEGA/CHARA.

Our model allows fitting of separate sets of relative luminosities $L_{\rm R}$ for each passband, because the visibilities were estimated in narrow passbands: i) four for CHARA/VEGA, ii) sixteen for NPOI, and iii) ≈ 40 for VLTI/AMBER. It was not possible to divide the data into a large number of small groups and to densely sample the relative luminosity of components Aa, Ab, and B as a function of the wavelength. After a set of trial attempts we split the data into two subsets: 1) visible (MARKIII, NPOI, CHARA/VEGA), and 2) infrared (AMBER). This sampling is justified by very low variability of luminosity ratios with wavelength of all stars within the visible and infrared regions, which we checked using synthetic spectra from the PHOENIX grid (Husser et al. 2013). The relative luminosities of components Aa, and Ab did not converge to plausible values for the infrared subset (generally it predicted too low luminosity ratio between the two components of orbit 1), therefore we decided to use the estimate based on the PHOENIX grid and radii obtained from the light-curve analysis for components Aa, Ab, and the radius of component B was taken from Harmanec (1988).

The optimal set of parameters is listed in Table 11, and a plot of the model vs. the observations is in Figs. C.1 – C.10. The model qualitatively fits very well the variations of the V^2 (i.e. the curvature of the model data agrees with the curvature of the observed V^2) for all spectro-interferometric data.

[9] The investigated parametric space is given by the following ranges: $\theta_{\rm B} \in [0.0, 1.0]$ mas; $L_{\rm B} \in [0.4, 0.8]$; $L_{\rm Aa} \in [0.1, 0.3]$; $T_{\rm p,2} \in [55\,600.0, 55\,620.0]$ RJD; $a_2 \in [13, 18]$ mas; $e_2 \in [0.1, 0.3]$; $i_2 \in [50, 130]$ deg; $\omega_2 \in [0, 180]$ deg; $\Omega_2 \in [0, 360]$ deg; $\dot{\omega}_2 \in [1.5, 4.0]$ deg yr^{-1}; $a_1 \in [1.0, 3.0]$ mas; $\Omega_1 \in [0, 360]$ deg;

7. Summary of analyses based on simple analytic models

Here the results of individual observational methods are critically compared and the properties of the system are derived.

7.1. Performance of different observational methods

Despite the subtitle, the individual models, which were used to evaluate different observational methods, were not completely independent, since the results from one method often served as a starting point for another one. In some cases it was mandatory to take a parameter value from another model to stabilise the convergence to a steady solution. In the following paragraphs we discuss the outcome of different methods and their accuracy. An overview of all fitted parameters is given in Table 12 obtained through different methods (i.e. more values are given for some parameters). Corresponding properties of the orbits and stars are also listed. **Orbital elements of orbit 3 are not listed, since their properties were constrained only by astrometry, and are presented separately in Table 10. The mass of component C is briefly discussed here.**

- **The spectroscopic elements:** Elements (K, e, $T_{\rm p}$, P, ω, $\dot{\omega}$) of both orbits are estimated better from the fit of directly measured RVs with an analytic model (see Tab 5, Eqs. 2, 3). The spectral disentangling works with a much more complex model and the resulting orbital elements depend on the shape of disentangled profiles (and vice-versa), which come out warped (the degree of the warp is shown by grey line in Fig A.1). The warp is the most pronounced for component B meaning that especially mass ratio q_2 coming from the method cannot be trusted. On the other hand, the thin lines of components Aa and Ab constrain the RVs very well even if the disentangled spectrum is not perfect, and so for the remaining orbital parameters the disentangling provides values, which agree with the fit of directly measured RVs.
- **The ephemeris of orbit 1:** The photometric solution presented in Table 9 yields the best ephemeris ($T_{\rm min,1}$, P_1) of orbit 1 especially thanks to high precision observations from the satellite MOST. The ephemeris for orbit 1 estimated from the RVs does not agree within uncertainties with the photometric one. It can be caused by the lower precision of RV measurements around eclipses.
- **The eccentricity of orbit 1:** It was set to zero throughout the analyses, because the precision of data does not allow its reliable determination. The analysis of the light curve from the satellite MOST shows a hint of a small eccentricity, but the relative position of minima is also affected by ETVs and we are unable to discern one from another with the analytic models. The dynamics of the system (see Sects. **8** and 9) shows that the eccentricity should oscillate with an amplitude $\Delta e \approx 0.01$. This introduces "a jitter" of the relative position of the primary and secondary minimum, and increases uncertainty of the radii if a circular model is applied.
- **The inclination of orbit 1:** It is determined accurately using the light curve analysis presented in Table 9. The value obtained from the interferometric model suffers from large uncertainty and is about 10 deg off the photometric solution. It is probably caused by low number of observations at high spatial frequencies and the calibration systematic errors, which are likely more pronounced for high-frequency data.
- **The longitude of the ascending node:** The longitude of the ascending node of orbit 1 has a mirror solution $\Omega_1 = \Omega_1 +$

Table 11. Parameters corresponding to the best-fit of all available interferometric observations with the model defined by Eqs. (5) – (10). θ denotes the angular (uniform-disk) diameter.

Elements	Units	Values		
		Component properties		
Component		B	Aa	Ab
θ	(mas)	0.407±0.031	0.252[1,2]	0.231[1,2]
$L_{\rm R}^{\Delta\lambda_1}$		0.6373±0.0085	0.197±0.014	0.166±0.016
$L_{\rm R}^{\Delta\lambda_2}$		0.60[1]	0.22[1]	0.18[1]
		Orbital properties		
Orbit		2		1
$P_{\rm AN}$	(d)	145.471±0.045		–
$P_{\rm S}$	(d)	145.150±0.061		7.14664[1]
$T_{\rm p}$	(RJD)	55 609.36±0.64		–
$T_{\rm min}$		–		56 224.7248[1]
a	(mas)	15.93±0.070		1.89±0.11
e		0.212±0.0040		0.0[1]
q		–		0.945[1]
i	(deg)	86.67±0.12		86.85[1]
ω	(deg)	8.4±1.6		90.0[1]
Ω	(deg)	148.453±0.066		148.435[3]±1.9
$\dot{\omega}$	(deg yr^{-1})	2.02±0.31		0.0[1]
$\chi^2_{\rm R}$		5.806		

Notes. [1]The parameter was kept fixed. [2]Estimated from the solution from Table 9 and the Hipparcos parallax. [3]A solution shifted by 180 deg is also possible and has identical reduced chi-square. $\Delta\lambda_1 = [500, 800]$ nm, and $\Delta\lambda_2 = [1200, 2410]$ nm.

180 deg with (almost) the same value of the $\chi^2_{\rm R}$, while the Ω_2 is determined uniquely, because NPOI instrument acquired a large number of closure phase measurements. This means that it is not possible to say whether the motion of orbit 1 relative to orbit 2 is prograde or retrograde using solely the spectro-interferometric data.

– **The relative luminosities:** They were determined from: i) the light curve solution, ii) the comparison of synthetic and observed spectra, and iii) the interferometric solution.
  - The light curve solution gives the best description of their variations with the wavelength, but the values suffer from large uncertainties, because of correlations between the fitted parameters.
  - The fit of synthetic spectra to observed ones turned to be quite insensitive to relative luminosities, but it is so only because small parts of red spectra, containing only three weak spectral lines, were fitted. The relative luminosities obtained in the regions around $H\gamma$, and $H\beta$ roughly agree with the values obtained for the B band from the light-curve solution.
  - The bulk of the interferometric observations falls somewhere between the V and R bands. Therefore the relative luminosities detected with the spectro-interferometry are close to the V band value obtained from the light-curve solution. We were not able to obtain plausible estimates of relative luminosities for the infrared subset (AMBER), because the observations have low spatial resolution and do not resolve the eclipsing binary well.
– **The effective temperatures:** They are given better by the fits of observed spectra to synthetic ones, because the fitted regions contain many spectral lines (especially the region $\Delta\lambda = [4280, 4495]$ Å), where the photometry relies on four broad-band filters only. Also Prša & Zwitter (2006) stated that it is not possible to obtain accurate effective temperatures of both components of an eclipsing binary from the light-curve solution, unless the colour-constraining method (described by them) is employed. According to the authors the problem is even more pronounced if the two components are alike. Therefore we fixed the primary temperature and optimised the secondary one only. The result is in agreement with that obtained from the comparison of observed and synthetic profiles within the respective errors. The spectral types corresponding to these temperatures are B9 for components Aa and Ab, and B5-6 for component B.
– **The semimajor axes and masses:** The physical size of semimajor axes derived from the spectro-interferometry and the Hipparcos parallax (orbits 1, and 2) and those derived from the spectroscopy and photometry (orbit 1) and spectroscopy and spectro-interferometry (orbit 2) agree with each other within their uncertainties. The same applies to masses, which seem to fall within the limits of normal main-sequence (MS hereafter) masses corresponding to the respective spectral types (Harmanec 1988) – $m^{\rm Aa} = 2.25 \pm 0.03 \in [1.71, 2.41]\,{\rm M}_\odot$, $m^{\rm Ab} = 2.13 \pm 0.03 \in [1.71, 2.41]\,{\rm M}_\odot$, $m^{\rm B} = 3.89 \pm 0.25 \in [3.63, 4.6]\,{\rm M}_\odot$.
– **The total mass of the system and mass of component C** Using **the parallax** $\pi_{\rm a_2} = 14.96 \pm 0.51$ and the solution presented in Table 10 one can estimate the total mass of the system $m^{\rm Aa+Ab+B+C} = 9.88 \pm 1.06\,{\rm M}_\odot$. A comparison with the masses of the inner triple subsystem gives an estimate of the mass of component C $m^{\rm C} = 1.61 \pm 1.18\,{\rm M}_\odot$, **which is compliant with early F-type or late A-type star.**
– **The component radii:** All components seem to have normal radii for their respective spectral type (again checked against Harmanec 1988) — $R^{\rm Aa} = 1.70 \pm 0.04 \in [1.40, 2.06]\,{\rm R}_\odot$, $R^{\rm Ab} = 1.62 \pm 0.04 \in [1.40, 2.06]\,{\rm R}_\odot$, $R^{\rm B} = 2.8 \pm 0.3 \in [2.13, 2.85]\,{\rm R}_\odot$.
– **The dereddened colour index B-V:** These are derived with high level of uncertainty, because of high uncertainty of the luminosity ratios in different bands and the uncertainty of bolometric magnitudes. We compared the dereddened colour indices against tables computed by Flower (1996) —

$T^{\rm B}_{\rm teff,FLOWER}(-0.120) = 12\,370$ K,
$T^{\rm Aa}_{\rm teff,FLOWER}(-0.018) = 9\,810$ K,
$T^{\rm Aa}_{\rm teff,FLOWER}(-0.015) = 9\,760$ K,
— which are in very rough agreement with the values found by the comparison of the observed and synthetic spectra.T he uncertainty bars of the colour indices are very "generous" and match a wide range of temperatures.

– **The distance:** The number of applied observational methods allow us to estimate the distance of ξ Tau: 1) from the ratio of the physical and angular size of the semimajor axes, 2) from the distance modulus. The former seems to prefer parallax, which is slightly lower than the Hipparcos parallax (but still within error bars), the latter also puts ξ Tau farther than the Hipparcos observations, but their uncertainties are large, i.e. do not contradict the Hipparcos parallax. The parallax estimated from the ratio of the physical and angular size of semimajor axis of the outer orbit yields the most precise parallax $\pi_{\rm a_2} = 14.96 \pm 0.51$ mas.

7.2. Conclusion of the analytic models

The spectroscopy, the photometry, and the interferometry were studied with traditional (semi)analytic models. We found, that results obtained from different methods are consistent with each other, although some of them give better estimates of a particular set of parameters than the others. We took advantage of this differential sensitivity and compiled a resulting set of fundamental properties of the system.

During the analyses described in previous Sects. we noticed two effects pointing to the dynamical interaction in ξ Tau: (i) the advance of the apsidal line of the orbit 2, and (ii) the eclipse timing variations (ETVs) in the system 1. The first effect was explicitly taken into account, because omitting it would cause significant inconsistency between the observations and the model. The latter effect was "almost overlooked", if not for its hint in the very accurate photometric data from the MOST satellite. However, the analytic models above give only limited insights into dynamical effects in the four-body system such as ξ Tau. Nonetheless, we find they provide results that are very good, and also needed, as a starting point for a more sophisticated solution based on approach that includes dynamical evolution in a more complete way. We proceed in two steps.

In Sec. 8 we try to take the bull by the horns and develop a numerical model which takes into account gravitational interaction of all stars in the ξ Tau consistently. We use a fully numerical implementation, basically a standard N-body integrator which we extended by subroutines allowing us to model several types of observables relevant for the ξ Tau dataset.

Next, in Sec. 9, we summarise relevant analytic formulæ obtained by methods of perturbation theory, which provide insights into results from the fully numerical approach in Sec. 8. Despite their limitations, we find the analytic formulation of the most important orbital perturbations useful. Not only does it allow us to understand basic features in the numerical integrations, but its also readily provides the parametric dependencies.

8. N-body model of ξ Tauri with mutual interactions

Given the quadruple nature of ξ Tauri, and its relatively compact packing, it is necessary to proceed with an advanced N-body model which would account for mutual gravitational interactions of *all* four components. To this point, we shall now describe our numerical integrator, a definition of a suitable χ^2 metric, and overall results of our fitting procedure.

8.1. Numerical integrator and χ^2 metric

We use a standard Bulirsch–Stoer N-body numerical integrator from the SWIFT package (Levison & Duncan 2013). Our method is quite general – we can model classical Keplerian orbits, of course, but also non-Keplerian orbits (involving N-body interactions). We treat all stars as point masses only though; we have no higher-order gravitational terms and no tides in our model.

As explained below, this is a significant improvement of our previous application in Brož et al. (2010), because we can now account not only for the light-time effect but for complete eclipse timing variations (ETVs) of the inner binary, arising from both direct and indirect gravitational perturbations. At the same time, we do not use the simplification of Brož et al. (2010) and we consider all the components separately, because the equivalent gravitational moment:

$$J_2 \simeq \frac{1}{2}\left(\frac{a_1}{r}\right)^2 \frac{m^{\rm Aa} m^{\rm Ab}}{(m^{\rm Aa}+m^{\rm Ab})^2} \doteq 2\times 10^{-3} \tag{12}$$

of the inner eclipsing binary Aa+Ab is large at the distance of the component B.

We use five different coordinate systems: (i) Aa-centric (usually, for a specification of initial conditions and eclipse detection); (ii) barycentric (for the numerical integration itself); (iii) Aa+Ab photocentric (for a comparison with interferometric observations of component B); (iv) Aa+Ab+B photocentric (ditto for component C); (v) Jacobian (for computations of hierarchical orbital elements).

Initial conditions at a given epoch T_0 can be specified either in Cartesian coordinates – with x, y in the sky plane and z in the radial direction – or in *osculating* orbital elements. This very choice has a substantial role, because the outcome of the fitting procedure will be generally (slightly) different. The orbital elements can be considered less correlated quantities than Aa-centric Cartesian coordinates.

We try to account for as much observational data as we can using the following joint metric:[10]

$$\chi^2 = \chi^2_{\rm rv} + \chi^2_{\rm etv} + \chi^2_{\rm edv} + \chi^2_{\rm sky}\,, \tag{13}$$

$$\chi^2_{\rm rv} = \sum_{j=1}^{4}\sum_{i=1}^{N_{{\rm rv}\,j}} \frac{\left(v'_{z{\rm b}\,ji} + \gamma - v_{{\rm rad}\,ji}\right)^2}{\sigma^2_{{\rm rv}\,ji}}\,, \tag{14}$$

$$\chi^2_{\rm etv} = \sum_{i=1}^{N_{\rm etv}} \frac{\left(t'_{{\rm A}i} - t_{{\rm A}i}\right)^2}{\sigma^2_{{\rm etv}\,i}}\,, \tag{15}$$

$$\chi^2_{\rm edv} = \sum_{i=1}^{N_{\rm edv}} \frac{\left(\epsilon'_{{\rm A}i} - \epsilon_{{\rm A}i}\right)^2}{\sigma^2_{{\rm edv}\,i}}\,, \tag{16}$$

$$(\Delta x_{ji}, \Delta y_{ji}) = \mathbf{R}\left(-\phi_{\rm ellipse} - \frac{\pi}{2}\right) \times \begin{pmatrix} x'_{{\rm p}\,ji} - x_{{\rm p}\,ji} \\ y'_{{\rm p}\,ji} - y_{{\rm p}\,ji} \end{pmatrix}\,, \tag{17}$$

$$\chi^2_{\rm sky} = \sum_{j=3}^{4}\sum_{i=1}^{N_{{\rm sky}\,j}} \left\{ \frac{(\Delta x_{ji})^2}{\sigma^2_{{\rm sky\,major}ji}} + \frac{(\Delta y_{ji})^2}{\sigma^2_{{\rm sky\,minor}ji}} \right\}\,, \tag{18}$$

[10] The program used for these computations, including sources and all input data, is available at `http://sirrah.troja.mff.cuni.cz/~mira/xitau/`.

Table 13. Notation used for various coordinates, velocities and uncertainties, which we use in our N-body model.

x, y, z	Aa-centric coordinates
v_x, v_y, v_z	Aa-centric velocities
$x_{\rm pB}, y_{\rm pB}$	Aa+Ab photocentric sky-plane coordinates (of component B)
$x_{\rm pC}, y_{\rm pC}$	Aa+Ab+B photocentric coordinates (of component C)
$v_{z\rm b}$	barycentric radial velocity
γ	systemic velocity
$v_{\rm rad}$	observed radial velocity
$t_{\rm A}$	mid-epoch of an eclipse of the Aa+Ab pair
$\epsilon_{\rm A}$	eclipse duration
$\sigma_{\rm rv}$	uncertainty of the radial velocity
$\sigma_{\rm etv}$	uncertainty of the eclipse mid-epoch timing
$\sigma_{\rm edv}$	uncertainty of the eclipse duration
$\sigma_{\rm sky\,major,\,minor}$	uncertainty of the astrometric position, angular sizes of the uncertainty ellipse
$\phi_{\rm ellipse}$	position angle of the ellipse
$\mathbf{R}(\dots)$	the corresponding 2×2 rotation matrix

where the notation is briefly described in Table 13. The dashed quantities are the model values linearly interpolated to the exact times t_i of observations. The index j goes over the list of components Aa, Ab, B, C (i.e. $j = 1 =$ Aa, …), while the index i corresponds to the observational data.

Regarding the observational data, we have radial-velocity measurements for the three components (Aa, Ab, B), altogether $N_{\rm rv} = 843$, minima timings for the eclipses in the inner binary (Aa+Ab), $N_{\rm etv} = 35$, and astrometric observations for components B and C, $N_{\rm sky} = 49$. The latter is a subset of measurements from NPOI and WDS, for which it was possible to convert fringe visibilities (averaged over one night) to distance–angle values.[11] The individual uncertainties of the observations used in this Sect. were modified as follows: $\sigma_{\rm rv} \geq 2\,{\rm km\,s^{-1}}$ due to calibration uncertainties, $\sigma_{\rm etv} \geq 0.001\,{\rm d} = 1.5\,{\rm min}$, because the quasi-periodic oscillations visible in the MOST light curve shift minima timings in a random fashion, and $\sigma_{\rm sky} = 3\,{\rm mas}$ (as in Tokovinin et al. 2015) or 5 mas if not reported in WDS.

We assumed the nominal distance $d = 64.1\,{\rm pc}$ for ξ Tau. The stellar radii for an eclipse detection were $R^{\rm Aa} = 1.700\,R_\odot$ and $R^{\rm Ab} = 1.612\,R_\odot$, in accord with the photometric inversion. Note that a to-be-expected correlation among $R^{\rm Aa}$, $R^{\rm Ab}$, eclipse depth, eclipse duration and third light contribution is removed to some extent thanks to spectroscopic observations (cf. Table 9).

The synthetic minimum distance Δ' between the components Aa and Ab in the sky plane was determined analytically as the distance of the piece-wise straight line $(x_{\rm Ab}, y_{\rm Ab})$ from the origin in the Aa-centric coordinates, as provided by the numerical integration. The condition for an eclipse is then simply $\Delta' \leq R^{\rm Aa} + R^{\rm Ab}$ and the corresponding time $t'_{\rm A}$ is linearly interpolated from neighbouring points. The eclipse duration is then given by a simple geometry, $\epsilon'_{\rm A} = 2\sqrt{(R^{\rm Aa} + R^{\rm Ab})^2 - \Delta'^2}/\bar{v}$, where $\bar{v}$ denotes the average velocity between the points. We thus straightforwardly account for disappearing eclipses and their durations, but we do not model (possible) eclipse depth variations at this stage.

[11] In our N-body model we do *not* fit the observed spectra using synthetic ones, individual light curve points, or interferometric fringes. We use higher-level observational data instead which were reduced and derived in previous Sects..

Table 14. A subset of minima timings $t_{\rm A}$ and eclipse durations $\epsilon_{\rm A}$ determined from MOST light curves, which were corrected for quasi-periodic oscillations by means of Eq. (19), and corresponding uncertainties $\sigma_{\rm etv}$ and $\sigma_{\rm edv}$.

$t_{\rm A}$ RJD	$\sigma_{\rm etv}$ day	$\epsilon_{\rm A}$ day	$\sigma_{\rm edv}$ day
56 224.7242	0.0010	0.2656	0.0069
56 228.3017	0.0012	0.2611	0.0035
56 231.8686	0.0010	0.2678	0.0069
56 235.4452	0.0010	0.2573	0.0035

In order to remove minor systematics in minima timings and eclipse duration, we attempted to suppress quasi-periodic oscillations visible in the MOST light curve by subtracting a function of the following form:

$$f(t) = C_0 + C_1(t - T_1) - [A_0 + A_1(t - T_1)] \sin\left[\frac{2\pi(t - T_1)}{P_0 + P_1(t - T_1)}\right]; \quad (19)$$

its coefficients $(C_0, C_1, T_1, A_0, A_1, P_0, P_1)$ were always determined by a *local* fit in the surroundings of the given minimum. The resulting data are reported in Table 14.

The relative luminosities for photocentre computations were set to $L^{\rm Aa} = 0.204$, $L^{\rm Ab} = 0.174$, and $L^{\rm B} = 0.622$ – again, in accord with photometric observations.

There are also mass constraints arising from the spectroscopic classification of the ξ Tau components (A9 V, A9 V, B5 V, and F V). We can easily enforce reasonable limits for the component masses with the following artificial term:

$$\chi^2_{\rm mass} = \sum_{j=1}^{4} \left[\left(m_j - \frac{m_{j\,\rm min} + m_{j\,\rm max}}{2}\right) \frac{2}{m_{j\,\rm max} - m_{j\,\rm min}}\right]^{100}, \quad (20)$$

where we used $m^{\rm Aa}$ and $m^{\rm Ab} \in (0.9, 3.0)\,M_\odot$, $m^{\rm B} \in (3.5, 3.9)\,M_\odot$, $m^{\rm C} \in (0.9, 2.0)\,M_\odot$ as the limits; the exponent is rather arbitrary.

The integrator and its *internal* time step was controlled by the parameter $\epsilon_{\rm BS} = 10^{-8}$ (unitless) which ensures a sufficient accuracy. The integration time span was 1 000 d forward and 11 000 d backward, and the output timestep $\Delta t = 0.5\,{\rm d}$ for initial runs. We verified that this sampling is sufficient even for the trajectory with the largest curvature and all necessary interpolations to the times of observations. For the final optimisation we decreased the value further down to $\Delta t = 0.1\,{\rm d}$ to suppress interpolation errors.

We use a standard simplex algorithm (Press et al. 1993) to search for local minima of χ^2. We have 23 potentially free parameters – masses m_j, coordinates x_j, y_j, z_j, velocities v_{xj}, v_{yj}, v_{zj} in the Aa-centric frame – or, alternatively, masses m_j and three sets of orbital elements $a_j, e_j, I_j, \Omega_j, \omega_j, M_j$ in Jacobian coordinates, and the systemic velocity γ. The convergence tolerance for χ^2 was set to $\epsilon_{\rm tol} = 10^{-6}$, and the maximum number of iterations 10 000 or as low as 300 for extended surveys of the parameter space. We confirmed that this low number is sufficient to quickly detect local minima or to exclude their existence.

The initial epoch $T_0 = 2\,456\,224.724705$ is very close to the first precise minimum of the MOST light curve. We can thus (almost) fix $x_{\rm Ab} \doteq y_{\rm Ab} = 0$. At the same time, it is possible to

(approximately) fix positions $x_{\rm pB}, y_{\rm pB}$ and $x_{\rm pC}, y_{\rm pC}$, derived by interferometry for an epoch close to T_0.

8.2. Resulting best fits

As expected, the 23-dimensional parameter space is vast and full of local minima, even at high χ^2. In order to be safe from headaches, we proceeded sequentially and we used: (i) 2012 data only, (ii) 2011–2013, and (iii) all observational data. Next we performed: (iv) a survey of the parameter space (to be sure we did not miss an obvious global minimum), (v) an optimisation of individual orbits (2 and 3), (vi) the mutual inclination of orbits 1 and 2, (vii) we switched from Cartesian coordinates to orbital elements, (viii) we let all parameters be free. The optimisation means that we started the simplex from scratch many times (with different initialisation) and let it converge (for a limited number of iterations). Our largest survey consisted of 10^5 simplex runs, 300 steps each, i.e. 3×10^7 models in total, so that we can be pretty sure there is no other "hidden" minimum, at least within the ranges searched so far.[12]

We are aware of *three* mirror solutions (and 2^3 combinations), namely the inner binary can orbit in a retrograde or prograde sense with respect to orbit 2, so that $i'_1 = 180^\circ - i_1$. Moreover, its node can be shifted by 180°, $\Omega'_1 = \Omega_1 + 180^\circ$. Last but not least, orbit 3 can have the opposite inclination, $i'_3 = -i_3$ (we have no direct RV measurements). These ambiguities are discussed and partly resolved in following paragraphs.

Our best fit is presented in Fig. 9 and Table 15. Note this is *not* the only fit which seems reasonable; there are many more available in the surroundings. This can be partially seen in Fig. 10 where 1-dimensional χ^2 maps exhibit relatively broad minima for the plotted parameters. Consequently, if we would use simplex within these ranges, we can surely find a different minimum with slightly larger χ^2 (or even slightly smaller).

We clearly see that the value of $\chi^2 = 2\,578$ is still about three times larger than the number of degrees of freedom, $\nu = N_{\rm data} - M_{\rm free} = 931 - 23 = 908$, and formally speaking we should be ready to admit that our model is plainly wrong. Nevertheless, the residua seem to be distributed normally and realistic uncertainties (including some systematics) may be larger than expected. In order to obtain $\chi^2 \simeq \nu$ we would need measurement uncertainties as large as $\sigma_{\rm rv} \simeq 3.5\,{\rm km\,s^{-1}}$, $\sigma_{\rm etv} \simeq 10\,{\rm min}$, $\sigma_{\rm sky} \simeq 1\,{\rm mas}$ (for component B) or $10\,{\rm mas}$ (for component C). We consider these numbers to be quite realistic given the heterogeneous data set we have. We can also imagine additional problems that may contribute to the error budget, e.g. nightly and night-to-night variations of dispersion relations, unaccounted blending of spectral lines, systematics due to the rectification procedure and disentangling, or photocentre motions of the inner binary affecting astrometric positions.

8.3. Differences between traditional and N-body models

Most importantly, orbital elements do change in the course of time; especially $i_1, \Omega_1, \omega_1, \Omega_2, \omega_2$ seem to be critical in the case of ξ Tau (see Fig. 11). While the precession of ω_2 was already accounted for, the remaining terms were not. The precession of nodes Ω_1, Ω_2 about the total angular momentum axis occurs with a ≈ 19 year period. In the Laplace plane, which is perpendicular to the total angular momentum, it would cause a circulation of Ω's from 0° to 360°, but we can only see an oscillation, of at most 3.5° — due to the purely geometrical projection to the plane of the sky. There are also inevitable *coupled* oscillations of inclinations, with i_1 ranging from 84.5° to 88.2°. All these rather expected secular effects are discussed in much more detail in Sect. 9.1.

Additionally, there are short-periodic oscillations not described by the secular theory. While a_1, a_2 only oscillate about constant mean values, there seems to be a 'mid-term' evolution of both e_1, e_2, with amplitudes reaching 0.008 which is larger than the uncertainty of their initial values, e.g. $e_2 = 0.1974^{+0.0009}_{-0.0010}$. In this particular case, it is related to the periastron passage of component C.

Let us emphasise, that it is absolutely necessary to use an N-body model (like ours), otherwise traditional methods assuming *constant* orbital elements (or precessing ω's only) may result in systematic discrepancies or artefacts. If we compare the parameters reported in Table 15 to those derived by classical models (Table 12), we see there is a rough agreement between the elements, but their uncertainty intervals do not always overlap. This is probably not surprising, as we compare (osculating) apples and (fixed) oranges.

An outstanding example how classical methods may fail, is a detailed analysis of MOST light curves and the corresponding minima timings from 2012. At first, we thought that the uneven spacing of minima indicates a non-zero eccentricity of the inner orbit, $e_1 \simeq 0.002$. However, this is in stark contrast with past RV measurements, which constrain forcing of $e_1(t)$ due to perturbations by component B and require $e_1(t = T_0) \to 0$. Looking carefully at Fig. 12, we realised that the oscillation of the semi-major axis a_1 has a period 3.76 days, which is *half* of the synodic period $P_{\rm syn1}$ of orbit 1, in a system which corotates with orbit 2. Moreover, its amplitude slightly decreases, as component B moves further away. These tiny perturbations are the *real* cause of the observed eclipse timing variations. They also allow us to discard mirror models with $\Omega'_1 \neq \Omega_2$ and prefer those with $\Omega_1 \simeq \Omega_2$, because the resulting $\chi^2_{\rm etv} = 390$ vs 150 is significantly different. Again, the eclipse variations are explained in more detail in Sect. 9.2.

8.4. A model with closure phases to resolve mirror solutions

The admissible solutions presented in Table 15 are degenerate in the sense that we cannot distinguish among several mirror models (in particular i'_1, i'_3). In order to resolve this degeneracy, hereinafter, we construct an N-body model which accounts for interferometric visibilities and closure phases. The latter are especially suitable to detect any asymmetries, while the former are necessary to get (symmetric) angular positions and separations right.

Apart from Eqs. (14) to (18) we have a few more relations:

$$V'(u,v) = \frac{1}{L_{\rm tot}} \sum_{j=1}^{4} L_{ij}\, 2\frac{J_1\left(\pi\theta_j\sqrt{u^2+v^2}\right)}{\pi\theta_j\sqrt{u^2+v^2}}\, {\rm e}^{-2\pi{\rm i}(ux'_{{\rm a}j}+vy'_{{\rm a}j})}\,, \tag{21}$$

$$L_{ij}(T_{{\rm eff}\,j}, R_j) \doteq \int_{\lambda_i-\Delta\lambda_i/2}^{\lambda_i+\Delta\lambda_i/2} 4\pi R_j^2\, \pi B_\lambda(T_{{\rm eff}\,j})\,{\rm d}\lambda\,, \tag{22}$$

[12] The ranges expressed in Cartesian coordinates were: $z_{\rm Ab} \in (-0.148, -0.088)\,{\rm au}$, $z_{\rm B} \in (-1.47, -0.87)\,{\rm au}$, $z_{\rm C} \in (-8.72, -2.72)\,{\rm au}$, $v_{x{\rm Ab}} \in (-0.092, -0.032)\,{\rm au\,d^{-1}}$, $v_{y{\rm Ab}} \in (0.050, 0.110)\,{\rm au\,d^{-1}}$, $v_{x{\rm B}} \in (-0.078, -0.018)\,{\rm au\,d^{-1}}$, $v_{y{\rm B}} \in (0.042, 0.102)\,{\rm au\,d^{-1}}$, $v_{z{\rm B}} \in (-0.022, 0.038)\,{\rm au\,d^{-1}}$, $v_{x{\rm C}} \in (-0.082, -0.022)\,{\rm au\,d^{-1}}$, $v_{y{\rm C}} \in (0.025, 0.085)\,{\rm au\,d^{-1}}$, and $v_{z{\rm C}} \in (-0.030, 0.030)\,{\rm au\,d^{-1}}$.

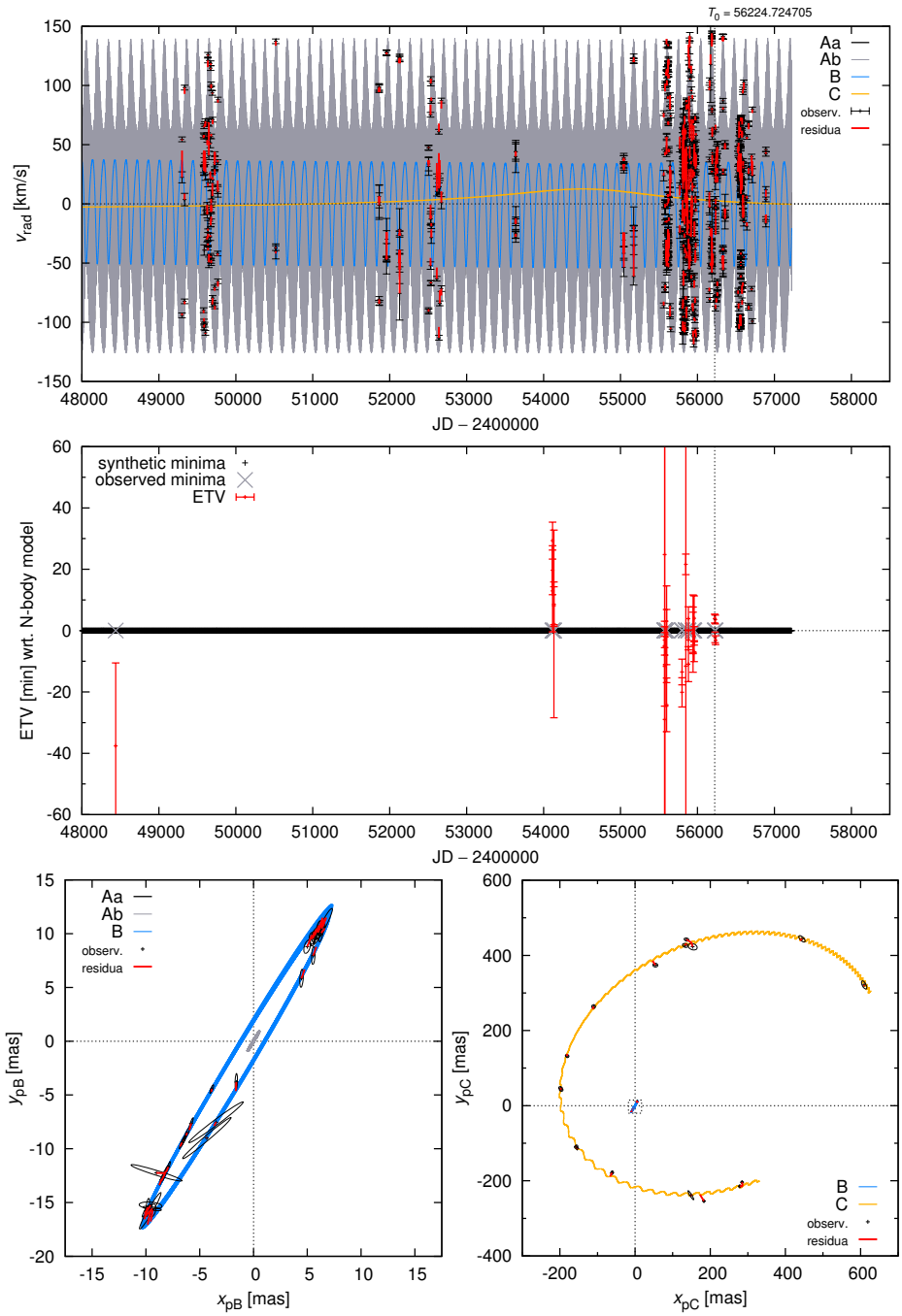

Fig. 9. One of the best-fit solutions for the ξ Tau system with our N-body model and using all available observational data. In this case, the resulting total χ^2 is 2 578, while the number of degrees of freedom $\nu = 908$. Top: Radial velocities $v_{z\mathrm{bAa}}$, $v_{z\mathrm{bAb}}$, $v_{z\mathrm{bB}}$, $v_{z\mathrm{bC}}$ of the individual components; model values are denoted by lines (component Aa is black, actually not clearly visible, Ab grey, B blue, and C orange), observations by black error bars and residuals by thick red lines. Middle: $O - C$ values for both primary and secondary minima timings; model timings are denoted by black points (very densely packed), observations by grey crosses and $O - C$ with its uncertainty by red error bars. Bottom left: Astrometric positions of component B based on NPOI interferometric observations; model orbit x_{pB}, y_{pB} with respect to photocentre Aa+Ab (i.e. not wrt. B, as usually) is again denoted by a blue line, observations by black error bars and residuals by thick red lines. The orbit is *not* a single ellipse, but rather a complex trajectory which is quickly precessing and moreover affected by (slight) photocentre motions. Bottom right: Similarly, astrometric positions of the distant component C x_{pC}, y_{pC} with respect to the Aa+Ab+B photocentre is denoted by an orange line. Component B is relatively luminous, which makes the orbit in these photocentric coordinates a bit jagged.

$$\chi^2_{\mathrm{vis}} = \sum_{i=1}^{N_{\mathrm{vis}}} \frac{\left(|V'(u_i,v_i)|^2 - |V|_i^2\right)^2}{\sigma^2_{\mathrm{vis}\,i}}\,, \tag{23}$$

$$T'_3 = V'(u_1,v_1)V'(u_2,v_2)V'(-(u_1+u_2),-(v_1+v_2))\,, \tag{24}$$

$$\chi^2_{\mathrm{clo}} = \sum_{i=1}^{N_{\mathrm{clo}}} \frac{(\arg T'_3 - \arg T_{3i})^2}{\sigma^2_{\mathrm{clo}\,i}}\,, \tag{25}$$

with the notation described in Table 16. The complex visibilities V' and their triple products T'_3 are computed assuming uniform disks for individual components. Relative luminosities L_{ij}

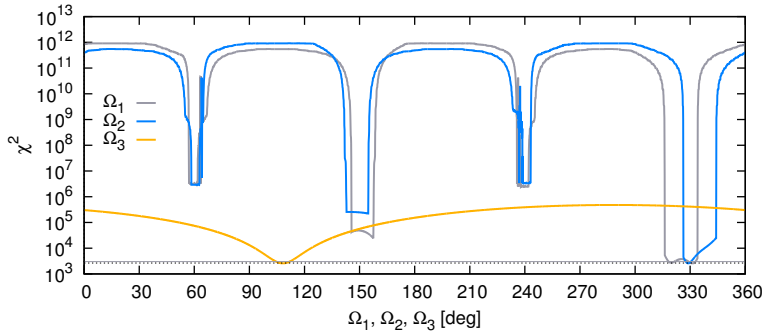

Fig. 10. An example of a 1-dimensional χ^2 mapping used to derive uncertainties of orbital elements for the ξ Tau system. The dependencies of the χ^2 values on the three nodes $\Omega_1, \Omega_2, \Omega_3$ are shown, while the remaining elements correspond to the best-fit values from Table 15. One can clearly see the preferred solution for $\Omega_1 \simeq 331°$, with $\chi^2 = 2\,578$, and a hint of a mirror solution at $\Omega_1 \simeq 151°$. If the latter is optimised separately, one would obtain χ^2 as low as 2 749. The sudden increase of $\chi^2_{\rm etv}$ corresponds to the disappearance of eclipses of the inner binary, which naturally results in extreme $O-C$'s.

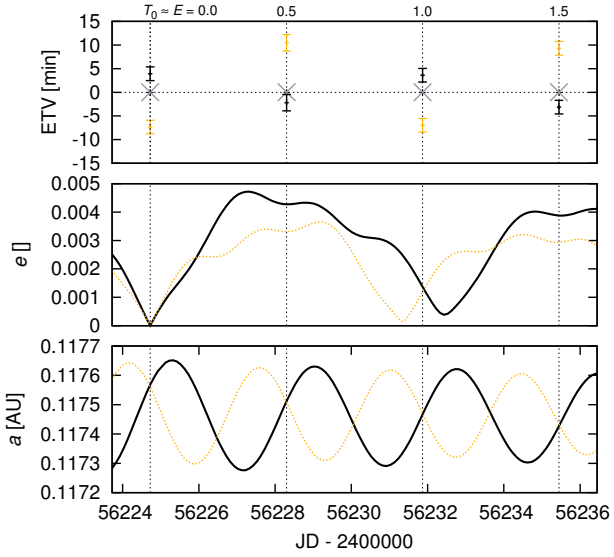

Fig. 12. A comparison of the osculating semimajor axis a_1 (bottom) and eccentricity e_1 evolution (middle) as computed by our N-body model for two mirror solutions with $\Omega_1 \doteq 331°$ (bold solid) and $\Omega'_1 \doteq 151°$ (red dashed). Only a short time span of 12 days is shown, close to the epoch T_0. The corresponding ETVs of minima observed by MOST are also shown at the top. The former solution $\Omega_1 \simeq 331°$ has the corresponding $\chi^2_{\rm etv}$ (for all $N_{\rm etv} = 35$ measurements) significantly lower than the latter, 150 vs 390, so that we consider it as the preferred value.

Table 16. Notation used for additional coordinates and quantities needed in our extended N-body model.

$x_{\rm a}, y_{\rm a}$	Aa-centric angular coordinates
V	complex visibility; squared visibility is $\|V\|^2$
T_3	complex triple product; closure phase is $\arg T_3$
u, v	projected baselines (expressed in cycles, B/λ)
$\theta = \frac{2R}{d}$	angular diameter
d	distance to the system
$L, L_{\rm tot}$	component luminosity and the total luminosity
$T_{\rm eff}$	effective temperature
R	stellar radius (uniform-disk)
$\lambda, \Delta\lambda$	effective wavelength and bandwidth
$B_\lambda(T)$	the Planck function
$\sigma_{\rm vis}$	uncertainty of the squared visibility
$\sigma_{\rm clo}$	uncertainty of the closure phase

at a given effective wavelength λ are computed by a black-body approximation.

This extended model minimises $\chi^2 = \chi^2_{\rm rv} + \chi^2_{\rm etv} + \chi^2_{\rm edv} + \chi^2_{\rm sky} + \chi^2_{\rm vis} + \chi^2_{\rm clo}$ and has nine additional free parameters: distance d to ξ Tau , uniform-disk radii R_j, and effective temperatures $T_{{\rm eff}\,j}$ of all the components, even though the contribution of component C is only minor (definitely less than 10 % at the longest wavelength, $\lambda = 2.6\,\mu$m).

We use all observational data from the MARKIII, NPOI, CHARA/VEGA and VLTI/AMBER spectro-interferometers, with $N_{\rm vis} = 17\,391$ measurements of the squared visibility $|V|^2$ and $N_{\rm clo} = 4\,856$ measurements of the closure phase $\arg T_3$ (from NPOI and VLTI/AMBER). The total number of degrees of freedom is thus $\nu = N_{\rm data} - M_{\rm free} = 28\,019 - 32 = 27\,987$. At the same time we do *not* use astrometric positions ($\chi^2_{\rm sky}$) of component B, because they are not independent; all the information should be contained in $|V|^2$ and $\arg T_3$ measurements.

Initially, we used nominal uncertainties and weights $w_{\rm vis} = 1$, $w_{\rm clo} = 1$, but the resulting $\chi^2_{\rm vis} + \chi^2_{\rm clo}$ value was too large ($\approx 10^5$), even for our best-fit models (cf. Fig. 13). The most likely reason is that we did not account properly for all calibration uncertainties. To resolve this issue an internal re-calibration would be necessary. Possible explanation for the too high χ^2 has been given in Sect. 6. For example, CHARA/VEGA interferometry from **Sep 29 2012** exhibits unrealistically quick changes of $|V|^2$ at an almost constant baseline $B/\lambda \doteq 1.3$ to 1.4×10^8 cycles (see Fig. C.8). In our case, we simply decreased the weight $w_{\rm vis} = 0.1$ in order not to dominate over other χ^2 contributions (e.g. eclipse timing variations).

We focused on a limited set of seven mirror models, always with one or two modified orbital elements (see Table 17). For each of them, we performed one simplex run, verified by simulated annealing[13] — so that *other* free parameters can adapt themselves to a new situation — and we computed χ^2's, which are reported in the same table. If the final value remains relatively large, it means the model is not compatible with the respective interferometric data.

Clearly, we are sufficiently sensitive to resolve Ω_2 and i_2, i.e. the longitude of the ascending node and the inclination of component B (see Fig. 14), but not directly to resolve Ω_1, i_1, or i_3 elements. Consequently, we can discard Ω'_2, i'_2 and prefer $\Omega_2 \simeq 331°$, $i_2 \simeq 86°$ solution on the basis of the closure phase measurements alone.

[13] with the initial "temperature" 100 000 "kelvin", schedule $T^{i+1} = 0.99T^i$ and 100 iterations at given T^i

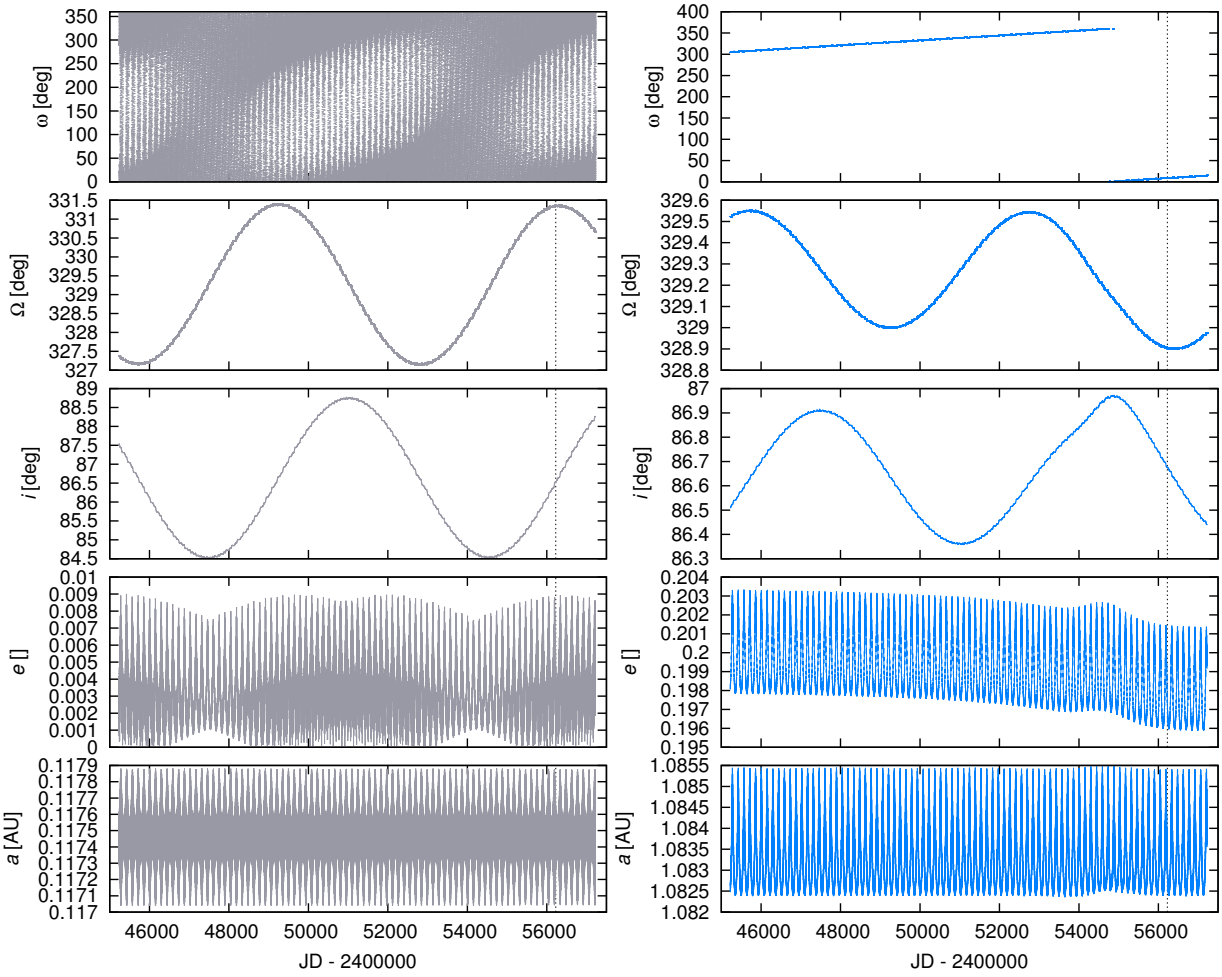

Fig. 11. Time evolution of the osculating orbital elements over a time span −11 000 to +1 000 days from the epoch $T_0 = 2\,456\,224.724705$, covered by observations of ξ Tau. Left: The semimajor axis a_1, eccentricity e_1, inclination i_1, longitude of ascending node Ω_1, and the argument of pericentre ω_1 (poorly defined because $e_1 \to 0$) of the inner, eclipsing binary orbit (components Aa and Ab). Right: The same parameters $a_2, e_2, i_2, \Omega_2, \omega_2$ for the orbit 2 (i.e. components (Aa+Ab) and B). All these plots correspond to the simulation with $\chi^2 = 2\,578$, presented in Fig. 9. Variations in the inclination i_1 and argument of pericentre ω_2 are of major interest, since they result in observable effects. On the other hand, the distant orbit 3 (not shown here) exhibits only minor variations of its elements. The "bump" in the osculation elements of orbit 2 at JD ≈ 2 455 500 is related to the passage of component C through its pericentre.

Moreover, because our N-body model is all the time constrained by RV, ETV, ETD and astrometric data, which prevent a convergence to unrealistic values of all the parameters, we can spot (in Table 17) that the squared visibility measurements are not compatible with Ω_1' and i_1', so they are discarded too and the $\Omega_1 \simeq 329°$, $i_1 \simeq 86°$ solution is preferred.

Finally, as already demonstrated in Sect. 8.3, the N-body dynamics and ETV measurements allow us to safely discard any $\Omega_1 \neq \Omega_2$, so we definitely prefer $\Omega_1 = 329°$. The only remaining ambiguity is thus the inclination i_3 vs i_3'. To conclude this Sect., a combination of more-or-less orthogonal measurements (RV, ETV, ETD, $|V|^2$, $\arg T_3$) leads to interesting and solid results, which is *not* surprising at all.

Let us also comment on the fact that even this kind of model may be actually insufficient. There exist other physical effects we did not account for, e.g. tidal interactions of non-spherical stars, spin–orbital coupling, various magneto-hydrodynamic phenomena, or pulsations of (all) components. Their importance for the dynamics of ξ Tau is yet to be assessed.

Table 17. Summary of $\chi^2_{\rm vis}$ and $\chi^2_{\rm clo}$ values for squared visibility $|V|^2$ and closure phase $\arg T_3$ measurements. Only a limited set of mirror models is shown — with respect to the nominal model ($\Omega_1 \simeq 331°$, $\Omega_2 \simeq 329°$, $\Omega_3 \simeq 110°$, $i_1 \simeq 86°$, $i_2 \simeq 86°$, $i_3 \simeq -24°$). The closure phase measurements allow us to discard four of them, namely those with Ω_2' and i_2', because the 3-σ level corresponds to a relative increase by 1.051, i.e. $\chi^2_{\rm clo} \simeq 24\,331$. Moreover, the $|V|^2$ measurements do not favour Ω_1' and i_1' (3σ is at 1.028, $\chi^2_{\rm vis} \simeq 137\,229$). The symbol × in the last column indicates we discard this possibility.

Orbital elements	$\chi^2_{\rm vis}$	$\chi^2_{\rm clo}$	Note
nominal	133 492	23 151	
$\Omega_1' = \Omega_1 + 180° \simeq 151°$	**162 632**	23 053	×
$\Omega_2' = \Omega_2 + 180° \simeq 149°$	355 456	**105 975**	×
(Ω_1', Ω_2')	322 079	**100 480**	×
$i_1' = 180° - i_1 \simeq 94°$	**149 901**	24 683	×
$i_2' = 180° - i_2 \simeq 94°$	734 267	**69 102**	×
$i_3' = -i_3 \simeq 24°$	138 316	23 393	
(i_1', i_2')	755 013	**69 463**	×

9. Dynamical evolution of the Aa+Ab+B subsystem

Osculating orbital elements shown in Fig. 11 exhibit many variations over different timescales, from the short period of the inner

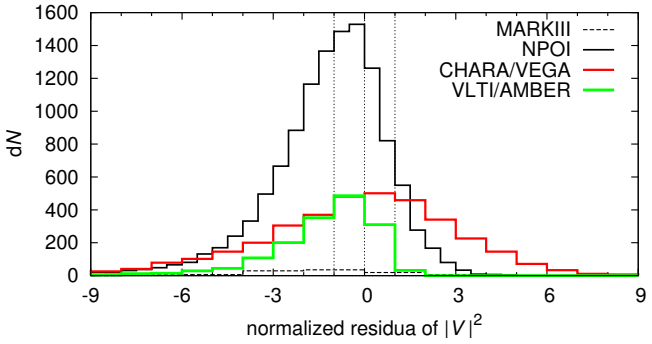

Fig. 13. Distributions of normalised residuals $(|V'|^2 - |V|^2_i)/\sigma_{\mathrm{vis}\,i}$ of the squared visibility for our 'best-fit' model with $\chi^2_{\mathrm{vis}} = 133\,492$, while the total number of measurements is $N_{\mathrm{vis}} = 17\,391$. Four separate datasets are shown, corresponding to the MARKIII, NPOI, CHARA/VEGA and VLTI/AMBER interferometers. Note the distributions are not perfectly symmetric about zero and that for CHARA/VEGA data is significantly wider, probably due to unaccounted calibration uncertainties.

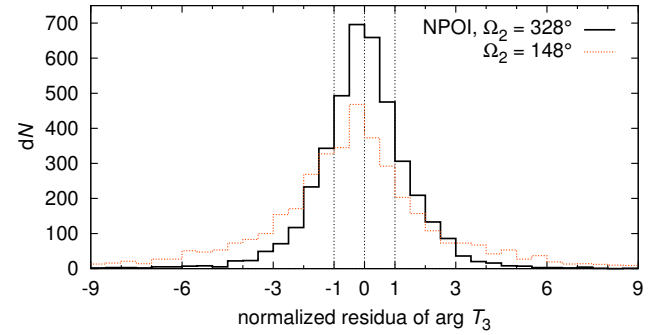

Fig. 14. Distributions of normalised residuals $(\arg T'_3 - \arg T_{3i})/\sigma_{\mathrm{clo}\,i}$ of the closure phase measured with the NPOI instrument for two 'best-fit' models with different values of the longitude of the ascending node $\Omega_2 = 329°$ and $\Omega'_2 = 149°$. Both distributions seem symmetric about the origin, indicating there are no serious systematics in $\arg T_3$ measurements. However, the former distribution is substantially narrower than the latter, so that the mirror solution Ω'_2 can be discarded.

eclipsing binary, to the intermediate period of the orbital motion of component B with respect to the eclipsing binary, up to long periods of tens to hundreds of years. Could we understand some of these terms, including their amplitude, and determine parametric dependencies on stellar masses and periods of orbits 1 and 2? To do so we need to turn to perturbation theory. In this Sect., we neglect dynamical effects of the distant component C and focus on the triple subsystem Aa+Ab+B.

The hierarchy of the ξ Tau system implies a preferential choice of Jacobi coordinates for the description of its dynamics, in which i) $\mathbf{r}$ is the relative position of Ab with respect to Aa, and ii) $\mathbf{R}$ is the relative position of component B with respect to the barycentre of orbit 1. The conjugate momenta involve reduced masses $m'_1 = m^{\mathrm{Aa}}m^{\mathrm{Ab}}/M^1$ and $m'_2 = m^{\mathrm{B}}M_1/M_2$ of orbits 1 and 2, with $M_1 = m^{\mathrm{Aa}} + m^{\mathrm{Ab}}$ and $M_2 = M_1 + m^{\mathrm{B}}$. To zero order approximation, both systems evolve on Keplerian orbits, but their interaction introduces a perturbation that makes $\mathbf{r}$ and $\mathbf{R}$ follow more complicated trajectories as described by numerical integrations in Sect. 8. The elliptical approximation may be only applicable to a certain interval of time. The latter becomes short especially for compact systems. ξ Tau is a good representative of this class.

In the world of perturbation theory, both orbits 1, and 2 are represented by a set of osculating orbital elements that evolve in time due to their mutual interaction. From a plethora of perturbations described in this way, we recall two results relevant for the observed features of the ξ Tau system. We first describe the secular effects, whose duration is conveniently short for this compact system to be detected, and then some of the long- and short-period eclipse time variations in the eclipsing binary.

9.1. Secular effects

We define Delaunay momenta $L_1 = m'_1\sqrt{GM_1a_1} = m'_1n_1a_1^2$ and $L_1 = m'_2\sqrt{GM_2a_2} = m'_2n_2a_2^2$ of orbits 1 and 2 (e.g., Harrington 1968, 1969; Soderhjelm 1975; Breiter & Vokrouhlický 2015). Here n_1 and n_2 are the mean motion values of the orbits 1 and 2, both related to the semimajor axes a_1 and a_2 via the third Kepler's law: $n_1^2a_1^3 = GM_1$ and $n_2^2a_2^3 = GM_2$ (G is the gravitational constant). In a secular approximation, when the orbital longitude for both orbits 1 and 2 is removed from the interaction (e.g., Harrington 1969; Breiter & Vokrouhlický 2015), the semimajor axes a_1 and a_2 are constant.

The dynamics of the Aa+Ab+B system may be, in principle, studied in an arbitrary reference frame. However, its description becomes very simple in a preferred, often called Laplacian, frame. The z-axis of this frame is aligned with the total orbital angular momentum of the system. In order to distinguish osculating orbital elements in the observer-oriented frame, used above, we shall denote the elements in the Laplacian frame with a tilde. For instance the orbital inclinations for orbits 1 and 2 will be denoted $\tilde{\imath}_1$ and $\tilde{\imath}_2$, and the corresponding longitudes of nodes $\tilde{\Omega}_1$ and $\tilde{\Omega}_2$.

The secular evolution of the triple system is particularly simple when (i) the eccentricity e_1 of the inner orbit is negligible, (ii) the mutual angle[14] $\tilde{J}$ of orbital planes 1 and 2 small, and (iii) the system is wide enough, such that on the timescale of interest only the quadrupole interaction of the inner and outer orbits is relevant. Luckily (i)-(iii) currently apply to the ξ Tau system.[15] Then, $e_1 = 0$ is a stable solution, and e_2 and $\tilde{J}$ are constant in time. In fact, referring the orbital elements to the invariable plane, normal to the total angular momentum, orbital inclinations $\tilde{\imath}_1$ and $\tilde{\imath}_2$ of orbits 1 and 2 are constant too, and both orbital planes uniformly precess in the inertial space about the total angular momentum direction. Their nodes $\tilde{\Omega}_1 = \tilde{\Omega}$ and $\tilde{\Omega}_2 = \tilde{\Omega} + \pi$ linearly advance with a rate (e.g., Soderhjelm 1975; Breiter & Vokrouhlický 2015):

$$\frac{\dot{\tilde{\Omega}}}{n_2} \simeq \frac{3}{4\eta_2^3}\frac{m^{\mathrm{B}}}{M_2}\frac{n_2}{n_1}\cos\tilde{J}\sqrt{1+\gamma^2+2\gamma\cos\tilde{J}}, \qquad (26)$$

where $\gamma = L_1/(L_2\eta_2)$ is the ratio of the angular momenta of the two orbits, and $\eta_2 = \sqrt{1-e_2^2}$. In triple systems usually the outer orbit has a dominant share of the total angular momentum

[14] The mutual angle $\tilde{J} = \tilde{\imath}_1 + \tilde{\imath}_2$ may be determined by the orbital elements in the observer frame using:

$$\cos\tilde{J} = \cos i_2\cos i_1 + \sin i_2\sin i_1\cos(\Omega_1 - \Omega_2)\ .$$

[15] As to (iii), note that the octupole interaction is very small because of nearly equal masses in orbit 1, i.e., $m^{\mathrm{Aa}} \simeq m^{\mathrm{Ab}}$. The next secular contribution would arise from the non-linear quadrupole effect (e.g., Breiter & Vokrouhlický 2015), which is small on a timescale of a couple of decades.

of the system, thus $\gamma < 1$. Indeed, for ξ Tau we have approximately $\gamma \simeq 0.132$. Unless precisely coplanar, the main effect of the orbital-plane precession is in periodic changes of inclinations i_1 and i_2 in the observer's system. These variations directly affect magnitude depths of the eclipses, or eventually could make the system non-eclipsing for a certain period of time.

Apart from the steady precession of the orbital planes, the second secular effect in the given setup consists in precession of the pericentre of the outer orbit. Denoting its longitude $\tilde{\varpi}_2$, we have:

$$\frac{\dot{\tilde{\varpi}}_2}{n_2} \simeq \frac{3}{8\eta_2^3}\frac{m^{\rm B}}{M_2}\frac{n_2}{n_1}\gamma\left(3\cos^2\tilde{J}-1 - \frac{\gamma\,\sin\tilde{J}\sin 2\tilde{J}}{1+\gamma\cos\tilde{J}+\sqrt{1+\gamma^2+2\gamma\cos\tilde{J}}}\right). \quad (27)$$

Comparing (26) and (27), we note that the pericentre precession frequency of the outer orbit is slower by a factor $\simeq \gamma$ than the nodal frequency (assuming $\tilde{J}$ sufficiently small). Thus nodes and inclinations vary on shorter times-scales than the argument of pericentre of orbit 2.

9.2. Long- and short-period eclipse variations

The mutual interaction of the orbits results also in a palette of periodic perturbations. So far the long-period effects, namely those having a period P_2 of orbit 2, have been extensively studied (e.g., Soderhjelm 1975, 1982; Borkovits et al. 2003, 2011, 2015). Out of them we shall focus on the ETVs, i.e. advances and delays $\delta t_{\rm LP}$ in epochs of eclipse of the orbit 1 due to the variations in its mean motion n_1 caused by component B. Assuming for simplicity coplanar orbits $\tilde{J} = 0\,$deg, one obtains (e.g., Soderhjelm 1975; Borkovits et al. 2011, 2015; Rappaport et al. 2013, which also contain terms proportional to $\propto \tilde{J}^2$)

$$n_1\delta t_{\rm LP} \simeq \frac{m^{\rm B}}{M_2}\frac{n_2}{n_1}\,W\,(e_2,\ell_2)\,, \quad (28)$$

with

$$W\,(e_2,\ell_2) = f_2 - \ell_2 + e_2\sin f_2, \quad (29)$$

where f_2 and ℓ_2 are the true and mean anomalies of orbit 2. For small eccentricity e_2 we have $W \simeq 3e_2\sin\ell_2$. Obviously, the principal component of ETV in (28) becomes zero for circular orbit 2, because it is related to variations of n_1 triggered by variations in the distance R to component B.

In the course of this work, we noted that also the dominant short-period effect may be of interest (those having the period of the inner orbit 1), provided high-quality eclipse data are collected. Using methods of first-order perturbation theory we found that the leading short-period term reads:

$$n_1\delta t_{\rm SP} \simeq \frac{21}{8}\frac{m^{\rm B}}{M_2}\left(\frac{n_2}{n_1}\right)^2\left(\frac{a_2}{R}\right)^3\sin 2\left(\lambda_1-\tilde{F}_2\right), \quad (30)$$

where R is the distance of component B to the barycentre of the inner binary system, and $\tilde{F}_2 = \tilde{\varpi}_2 + f_2$ is its true orbital longitude. Note the term has a period equal to half the synodic period of the Aa+Ab system in a reference frame corotating with the motion of component B.

This effect is not primarily dependent of the eccentricity e_2, because it is triggered by variations in the mutual positions of components Aa and Ab with respect to component B. Its magnitude is smaller by a factor 0.4 at periastron and by 0.1 at apoastron of orbit 2. Nevertheless, the effect is not entirely negligible and we found that it contributes to the observed eclipse shift in the MOST data (see Fig. 12).

9.3. Comparison of the secular theory with the results of the analytic and numerical models

Here we confront the apsidal motion detected with both analytic and numerical methods and additional secular and periodical variations of orbital elements predicted by the numerical model presented in Sec. 8.1

- **The apsidal motion of orbit 2:** First, we use results of the analytic theory above. Using nominal orbital parameters from Table 12 we obtain $\tilde{\mathbf{J}} = \mathbf{0.19 \pm 1.89}\,$deg, and consequently $\dot{\omega}_{\mathbf{2}} = \mathbf{2.185 \pm 0.045}\,\mathrm{deg\,yr^{-1}}$. Note that $\dot{\omega}_2$ may be directly obtained from Eq. (27), because the nodal longitude Ω_2 in the observer frame oscillates without any secular drift. This is about a third lower than the value detected with the analytic RV curve model (see Table 5), but in excellent agreement with the N-body model, whose prediction is $\dot{\omega}_2 = 2.11\,\mathrm{deg\,yr^{-1}}$, and with fit of the interferometric observations (see Table 11).
- **The nodal motion of orbits 1 and 2:** Inserting nominal parameters from Table 12 provides the mean nodal drift $\dot{\tilde{\mathbf{\Omega}}} = \mathbf{18.98 \pm 0.53}\,\mathrm{deg\,yr^{-1}}$ (Eq. 26), which is again in excellent agreement with results of the N-body model; note the periods of the nodal oscillations are effectively $\simeq 19.43\,\mathrm{deg\,yr^{-1}}$ for orbit of component A (Ω_1) and $\simeq 19.81\,\mathrm{deg\,yr^{-1}}$ for orbit B (Ω_2). Values not exactly the same, likely due to interaction with component C, which was not included in the perturbation theory. There is a hint of a shallower depth of the Hvar photometric observations from early 2007 when our model predicts a larger value of the inclination i_1. However, to pin down the inclination variations we need more accurate photometric observations in the future.
- **Eclipse-timing variations – orbit 1:** Eqs. (28, 29, 30) provide amplitudes of the ETVs (assuming that component B is at periastron) of orbit 1 $\delta t_{\rm ETV,long} = 0.0162 \pm 0.0007\,$d, $\delta t_{\rm ETV,short} = 0.0068 \pm 0.0003\,$d. Their sum is in agreement with the detected amplitude of ETVs ($\delta t_{\rm ETV,OBS} = 0.025 \pm 0.010\,$d). Note also, that the two primary eclipse minima in the MOST data were found to be phase-shifted by $\simeq 0.0003$ in Sect. 4.3. This is about 0.1° in orbital longitude of inner orbit 1. Combining results in Eqs. (28, 29, 30), and taking into account $\ell_2 \simeq 86^\circ$ and $\lambda_1 \simeq F_2$ from Table 15, we obtain very good agreement with the observed shift.

10. Motivations for future observations of ξ Tauri

First, it seems desirable to continue the observations of the times of minima and, more importantly, eclipse duration and depth. At an epoch after approximately RJD 59 405.0, i.e., summer 2021, one would expect either persisting, or disappearing eclipses of the inner pair Aa+Ab for different mirror solutions. Consequently, this is a direct and independent test of our analysis of closure phase measurements in Sec. 8.4. Note that the nominal solution shown in Fig. 11 exhibits too small variations of i_1, such that the eclipsing binary would be eclipsing all the time.

Nevertheless, even the nominal solution predicts nearly 4° full amplitude of variation in i_1 and one should expect fairly well

observable effects. We are suggesting, for instance, a space-born observation of a similar quality to that of MOST, obtained at the turn of 2016 and 2017, when the predicted i_1 value would be maximum (about $88.2°$). The change in eclipse depth, as compared to the MOST data, should be about 0.05 magnitude, very easily detectable. Such a single observation would further constrain parameters of ξ Tau with an exceptional accuracy.

It would be of great help if the line spectra of the faint component C, separated by 200 to 600 mas from the triple Aa+Ab+B, were obtained and the corresponding radial velocity measured. This would also allow us to distinguish between the remaining two mirror orbital solutions for the motion of this component.

Precise and uninterrupted space-based photometry on a longer time-span would be useful to unambiguously resolve oscillation modes and splittings. Given the high rotation frequency $f_{\rm rot} = 2.38\,{\rm d}^{-1} \simeq 27.5\,\mu$Hz, it should not be that difficult (the minimum time-span $\Delta t \simeq 1/f_{\rm rot}$), but currently aliases with instrumental frequencies seem to limit the S/N in the Fourier spectrum.

As an alternative, series of high-resolution high-S/N spectra would be needed to detect the oscillation modes independently, as the travelling sub-features in the line profiles of component B are broadened by a relatively high rotation. Precise RV measurements of components Aa and Ab may also "reveal" the Rossiter-McLaughlin effect, which gives the rotational sense of both components.

A new series of long baseline optical spectro-interferometric observations *including* measurements of closure phase are highly desirable, because they would: 1) provide a *fully* independent estimate of the orbital elements of the orbit 1, 2) independently determine the sense of revolution of the components of orbit 1 with respect to orbit 2, and 3) provide an independent estimate of the radii of components Aa and Ab.

11. Conclusion

We have conducted an in-depth study of the quadruple stellar system ξ Tau, starting from simple analytic models for different kinds of observations (see Sects. 3-7), and ending up with a complex N-body model, which combines astrometric, photometric, spectroscopic, and **spectro-interferometric** observations to a certain degree (see Sect. 8). We were able to put tight constraints on three components of ξ Tau, and they will provide an excellent test case for models of stellar evolution, while the full description of the geometry of the hierarchy will provide a test of the binary formation.

The analytic models allowed us to estimate properties of components Aa, Ab and B, which show a great deal of consistency (see critical summary of the analytic models in Sect. 7) and mean orbital elements of orbits 1, 2, and 3 using different methods – again consistent with each other, but provided limited-to-no insight into the dynamic evolution of orbits of the ξ Tau.

This discrepancy was fixed with the N-body model, which properly accounts for the dynamic interaction within the system and is able to fit RVs, ETVs, and astrometric positions simultaneously. It provided a set of osculating elements and component masses, whose evolution fits the observables (see Table 13). It also provided insight into long-term and short-term evolution of the osculating elements (see Fig. 11) and also resolved between the prograde and retrograde solution (between orbits 1 and 2) solely from ETVs. The result also gives credibility to previous analyses, because it did not drift far away from their outcome.

Perturbation theory shows that the most pronounced secular evolution of elements — the advance of the apsidal line of orbit 2, and the harmonic variation of the inclination $i_{1,2}$, and the longitude of the ascending node $\Omega_{1,2}$ — are explained by a quadrupole interaction between orbits 1 and 2. The same applies to the predicted size of ETVs, which are in good agreement with observations.

Acknowledgements. The research of JN, PH, MW, and PZ was supported by the grants P209/10/0715 and GA15-02112S of the Czech Science Foundation. The research of JN and PH was also supported by the grant no. 678212 of the Grant Agency of the Charles University. The Navy Prototype Optical Interferometer is a joint project of the Naval Research Laboratory and the US Naval Observatory, in cooperation with Lowell Observatory and is funded by the Office of Naval Research and the Oceanographer of the Navy. The authors thank Jim Benson and the NPOI observational support staff whose efforts made this project possible. This research has made use of the SIMBAD astronomical literature database, operated at CDS, Strasbourg, France. The CHARA Array is operated with support from the National Science Foundation through grant AST-0908253, the W. M. Keck Foundation, the NASA Exoplanet Science Institute, and from Georgia State University. This publication is supported as a project of the Nordrhein-Westfälische Akademie der Wissenschaften und der Künste in the framework of the academy programme by the Federal Republic of Germany and the state Nordrhein-Westfalen. HB acknowledges financial support by Croatian Science Foundation under the project 6212 "Solar and Stellar Variability". The project is based on data obtained from the ESO Science Archive Facility under request number jnemravova217453, on spectral data retrieved from the ELODIE archive at Observatoire de Haute-Provence (OHP), and on observations made at the South African Astronomical Observatory (SAAO). PZ wish to thank the staff at SAAO for their warm hospitality and help with the equipment. AFJM is grateful for financial assistance to NSERC (Canada) and FQRNT (Quebec). The observations with the MPG 2.2 m telescope were supported by the Czech Ministry of Education, Youth and Sports project LG14013 ("Tycho Brahe: Supporting Ground-based Astronomical Observations") during run P2 in May 2015. We acknowledge the use of the electronic database from the CDS, Strasbourg and electronic bibliography maintained by the NASA/ADS system. **We acknowledge the constructive criticism by the referee Peter P. Eggleton, which helped us to improve the paper.**

References

Aller, L. H., Appenzeller, I., Baschek, B., et al., eds. 1982, Landolt-Börnstein: Numerical Data and Functional Relationships in Science and Technology - New Series " Gruppe/Group 6 Astronomy and Astrophysics " Volume 2 Schaifers/Voigt: Astronomy and Astrophysics / Astronomie und Astrophysik " Stars and Star Clusters / Sterne und Sternhaufen
Armstrong, J. T., Mozurkewich, D., Rickard, L. J., et al. 1998, ApJ, 496, 550
Baranne, A., Queloz, D., Mayor, M., et al. 1996, A&AS, 119, 373
Benisty, M., Malbet, F., Millour, F., Absil, O., & Duvert, G. 2015
Bolton, C. T. & Grunhut, J. H. 2007, in IAU Symposium, Vol. 240, IAU Symposium, ed. W. I. Hartkopf, P. Harmanec, & E. F. Guinan, 66
Bonneau, D., Clausse, J.-M., Delfosse, X., et al. 2006, A&A, 456, 789
Borkovits, T., Csizmadia, S., Forgács-Dajka, E., & Hegedüs, T. 2011, A&A, 528, A53
Borkovits, T., Érdi, B., Forgács-Dajka, E., & Kovács, T. 2003, A&A, 398, 1091
Borkovits, T., Rappaport, S., Hajdu, T., & Sztakovics, J. 2015, MNRAS, 448, 946
Breiter, S. & Vokrouhlický, D. 2015, MNRAS, 449, 1691
Brož, M., Mayer, P., Pribulla, T., et al. 2010, AJ, 139, 2258
Butterworth, S. 1930, Wireless Engineer, 7
Campbell, W. W. 1909, Astrophysical Journal, 29, 224
Claret, A. 1998, A&AS, 131, 395
Claret, A. 2001, MNRAS, 327, 989
de Laverny, P., Recio-Blanco, A., Worley, C. C., & Plez, B. 2012, A&A, 544, A126
Degroote, P., Acke, B., Samadi, R., et al. 2011, A&A, 536, A82
Drimmel, R., Cabrera-Lavers, A., & López-Corredoira, M. 2003, A&A, 409, 205
Eggleton, P. P. & Kiseleva-Eggleton, L. 2001, ApJ, 562, 1012
Eggleton, P. P. & Tokovinin, A. A. 2008, MNRAS, 389, 869
ESA. 1997, VizieR Online Data Catalog, 1239
Fabrycky, D. & Tremaine, S. 2007, ApJ, 669, 1298
Fekel, J. F. C. 1981, ApJ, 246, 879
Flower, P. J. 1996, ApJ, 469, 355
Fuhrmann, K., Chini, R., Hoffmeister, V. H., et al. 2011, MNRAS, 411, 2311
Glindemann, A., Albertsen, M., Andolfato, L., et al. 2004, in Proc. SPIE, Vol. 5491, New Frontiers in Stellar Interferometry, ed. W. A. Traub, 447
Hadrava, P. 1995, A&AS, 114, 393
Hadrava, P. 1997, A&AS, 122, 581
Hadrava, P. 2009, ArXiv e-prints [arXiv:0909.0172]

Harmanec, P. 1988, Bulletin of the Astronomical Institutes of Czechoslovakia, 39, 329
Harmanec, P. 1998, A&A, 335, 173
Harmanec, P. & Horn, J. 1998, Journal of Astronomical Data, 4, 5
Harmanec, P., Horn, J., & Juza, K. 1994, A&AS, 104, 121
Harrington, R. S. 1968, AJ, 73, 190
Harrington, R. S. 1969, Celestial Mechanics, 1, 200
Hummel, C. A., Benson, J. A., Hutter, D. J., et al. 2003, AJ, 125, 2630
Hummel, C. A., Mozurkewich, D., Armstrong, J. T., et al. 1998, AJ, 116, 2536
Hummel, C. A., Zavala, R. T., & Sanborn, J. 2013, Central European Astrophysical Bulletin, 37, 127
Husser, T.-O., Wende-von Berg, S., Dreizler, S., et al. 2013, A&A, 553, A6
Kaufer, A., Stahl, O., Tubbesing, S., et al. 1999, The Messenger, 95, 8
Kraft, D. 1988, A software package for sequential quadratic programming, Deutsche Forschungs- und Versuchsanstalt für Luft- und Raumfahrt Köln: Forschungsbericht (Wiss. Berichtswesen d. DFVLR)
Lafrasse, S., Mella, G., Bonneau, D., et al. 2010, VizieR Online Data Catalog, 2300, 0
Lenz, P. & Breger, M. 2004, in IAU Symposium, Vol. 224, The A-Star Puzzle, ed. J. Zverko, J. Ziznovsky, S. J. Adelman, & W. W. Weiss, 786–790
Levison, H. F. & Duncan, M. J. 2013, SWIFT: A solar system integration software package, Astrophysics Source Code Library
Mason, B. D., Martin, C., Hartkopf, W. I., et al. 1999, AJ, 117, 1890
Moultaka, J., Ilovaisky, S. A., Prugniel, P., & Soubiran, C. 2004, PASP, 116, 693
Mourard, D., Clausse, J. M., Marcotto, A., et al. 2009, Astronomy and Astrophysics, 508, 1073
Mozurkewich, D., Armstrong, J. T., Hindsley, R. B., et al. 2003, AJ, 126, 2502
Nemravová, J. A., Harmanec, P., Bencheikh, J., et al. 2013, Central European Astrophysical Bulletin, 37, 207
Palacios, A., Gebran, M., Josselin, E., et al. 2010, A&A, 516, A13
Petrov, R. G., Malbet, F., Weigelt, G., et al. 2007, A&A, 464, 1
Press, W. H., Teukolsky, S. A., Vetterling, W. T., & Flannery, B. P. 1993, Numerical Recipes in FORTRAN; The Art of Scientific Computing, 2nd edn. (New York, NY, USA: Cambridge University Press)
Prša, A. & Zwitter, T. 2005, ApJ, 628, 426
Prša, A. & Zwitter, T. 2006, Ap&SS, 304, 347
Rappaport, S., Deck, K., Levine, A., et al. 2013, ApJ, 768, 33
Rica Romero, F. M. 2010, Rev. Mexicana Astron. Astrofis., 46, 263
Shao, M., Colavita, M. M., Hines, B. E., et al. 1988, A&A, 193, 357
Simon, K. P. & Sturm, E. 1994, A&A, 281, 286
Soderhjelm, S. 1975, A&A, 42, 229
Soderhjelm, S. 1982, A&A, 107, 54
Steiner, I., Stahl, O., Seifert, W., Chini, R., & Quirrenbach, A. 2008, in Society of Photo-Optical Instrumentation Engineers (SPIE) Conference Series, Vol. 7014, Society of Photo-Optical Instrumentation Engineers (SPIE) Conference Series, 4
Stellingwerf, R. F. 1978, ApJ, 224, 953
Storn, R. & Price, K. 1997, Journal of Global Optimization, 11, 341
Tallon-Bosc, I., Tallon, M., Thiébaut, E., et al. 2008, in Society of Photo-Optical Instrumentation Engineers (SPIE) Conference Series, Vol. 7013, Society of Photo-Optical Instrumentation Engineers (SPIE) Conference Series
ten Brummelaar, T. A., McAlister, H. A., Ridgway, S. T., et al. 2005, ApJ, 628, 453
Tody, D. 1986, in Society of Photo-Optical Instrumentation Engineers (SPIE) Conference Series, Vol. 627, Instrumentation in astronomy VI, ed. D. L. Crawford, 733
Tody, D. 1993, in Astronomical Society of the Pacific Conference Series, Vol. 52, Astronomical Data Analysis Software and Systems II, ed. R. J. Hanisch, R. J. V. Brissenden, & J. Barnes, 173
Tokovinin, A., Mason, B. D., Hartkopf, W. I., Mendez, R. A., & Horch, E. P. 2015, AJ, 150, 50
Tokovinin, A. A. 1997, A&AS, 124, 75
van Belle, G. T., Creech-Eakman, M. J., & Hart, A. 2009, MNRAS, 394, 1925
van Leeuwen, F. 2007, A&A, 474, 653
Walker, G., Matthews, J., Kuschnig, R., et al. 2003, PASP, 115, 1023
Zasche, P., Uhlář, R., Kučáková, H., Svoboda, P., & Mašek, M. 2014, Information Bulletin on Variable Stars, 6114, 1
Zasche, P. & Wolf, M. 2007, Astronomische Nachrichten, 328, 928

[1] Astronomical Institute of the Charles University, Faculty of Mathematics and Physics, V Holešovičkách 2, CZ-180 00 Praha 8 - Troja, Czech Republic
[2] Laboratoire Lagrange, OCA/UNS/CNRS UMR7293, BP4229, 06304 Nice Cedex, France
[3] European Southern Observatory, Karl–Schwarzschild–Str. 2, 85748 Garching bei München, Germany
[4] Department of Mathematics, Physics & Geology, Cape Breton University, 1250 Grand Lake Road, Sydney, NS B1P 6L2, Canada
[5] Department of Physics & Astronomy, University of British Columbia, 6224 Agricultural Road, Vancouver, BC V6T 1Z1, Canada
[6] Department of Astronomy and Astrophysics University of Toronto 50 St. George Street, Toronto, Ontario Canada M5S 3H4
[7] Hvar Observatory, Faculty of Geodesy, Zagreb University, Kačićeva 26, 10000 Zagreb, Croatia
[8] Astronomisches Institut, Ruhr-Universität Bochum, Universitätsstraße 150, D-44780 Bochum, Germany
[9] Instituto de Astronomía, Universidad Católica del Norte, Avenida Angamos 0610, Casilla 1280 Antofagasta, Chile
[10] Department of Astronomy and Astrophysics, Villanova University, Villanova, PA 19085, USA
[11] CHARA Array, Mount Wilson Observatory, Mount Wilson, CA 91023, USA
[12] Department of Astronomy and Physics, Saint Mary's University, Halifax, N.S., B3H 3C3, Canada
[13] Astronomical Institute, Academy of Sciences of the Czech Republic, 251 65 Ondřejov, Czech Republic
[14] Institute of Astronomy, University Vienna, Türkenschanzstrasse 17, A-1180 Vienna, Austria
[15] Department de Physique, Université de Montréal, C.P. 6128, Succursale Centre-Ville, Montréal, QC H3C 3J7, Canada
[16] Observatório do Instituto Geográfico do Exército, R. Venezuela 29 3 Esq., 1500-618, Lisbon, Portugal
[17] NASA Ames Research Center, Moffett Field, CA 94035, USA; SETI Institute, Mountain View, CA 94043, USA
[18] Université de Lyon, Université Lyon 1, Ecole Normale Supérieure de Lyon, CNRS, Centre de Recherche Astrophysique de Lyon UMR5574, F-69230, Saint-Genis-Laval, France
[19] U.S. Naval Observatory, Flagstaff Station, 10391 West Naval Observatory Road, Flagstaff, AZ 86005-8521

Table 12. Summary of parameters derived from the spectroscopic, photometric, and spectro-interferometric analyses. In some cases more values are listed for a parameter, to show that the methods do not contradict each other. **Being safely resolved only with the astrometry, elements of orbit 3 are not listed here, but in Table 10 and the mass of component C is estimated and briefly discussed in Sect. 7.** The listed parameters are the anomalistic period $P_{\rm AN}$, the sidereal period $P_{\rm S}$, the periastron epoch $T_{\rm p}$, the epoch of the primary minimum $T_{\rm min}$, the semimajor axis a, the mass ratio q, the eccentricity e, the inclination i, the periastron argument ω, the position angle of the nodal line Ω, the effective temperature $T_{\rm eff}$, the surface gravitational acceleration $\log g$, the projected rotational velocity $v \sin i$, the mass m, the radius R, the angular diameter θ, the bolometric magnitude $M_{\rm BOL}$, the Johnson V magnitude and colour indices V, $B-V$, $U-B$, the dereddened Johnson V magnitude and colour index V_0, B_0-V_0, **and** the parallax π.

Parameter	Unit	Source	Value		
			Orbital properties		
Orbit			2	1	
$P_{\rm AN}$	(d)	RV/LC	145.579±0.048	7.14664±0.00002	
$P_{\rm S}$	(d)	RV/LC	145.113±0.071	7.14664±0.00002	
$T_{\rm p}$	(RJD)	RV/–	55 609.46±0.52	–	
$T_{\rm min}$	(RJD)	–/LC	–	56 224.72482±0.00022	
a	($R_\odot$)	IF+HP/IF+HP	219±15	26.1±2.3	
	($R_\odot$)	IF+RV/IF+RV	*229.0±7.7	–	
	($R_\odot$)	–/RV+LC	–	*25.550±0.090	
$a_{\rm angular}$	(mas)	IF/IF	15.93±0.10	1.89±0.11	
e		RV/–	*0.2101±0.0053	0.0[1]	
		IF/–	0.2120±0.0040	0.0[1]	
q		RV/RV	0.889±0.056	0.9438±0.0036	
i	(deg)	IF/IF	86.67±0.12	86.85[1]	
	(deg)	–/LC	–	*86.85±0.22	
ω	(deg)	RV/–	*9.25±1.42	90.0[1]	
	(deg)	IF/–	8.4±1.6	90.0[1]	
$\dot{\omega}$	(deg yr^{-1})	RV/–	2.90±0.33	0.0[1]	
$\dot{\omega}$	(deg yr^{-1})	IF/–	2.02±0.31	0.0[1]	
Ω	(deg)	IF/IF	148.453±0.066	148.4[2]±1.9	
			Component properties		
Component			B	Aa	Ab
$T_{\rm eff}$	(K)	SP	14 190±150	10 700±160	*10 480±130
	(K)	LC	–	10700[1]	10450±150
$\log g_{\rm [cgs]}$		SP	4.527±0.041	4.08±0.12	4.01±0.10
		RV+LC	4.09±0.11	4.330±0.019	4.348±0.022
$v \sin i$	(km s^{-1})	SP	229.2±1.7	12.6±2.6	14.3±3.1
m	($M_\odot$)	RV+LC	*3.89±0.25	*2.252±0.027	*2.125±0.027
	($M_\odot$)	RV+IF	3.60±0.52	2.08±0.48	1.96±0.45
R	($R_\odot$)	RV+LC	–	1.700±0.035	1.618±0.039
	($R_\odot$)	IF+HP	2.81±0.28	–	–
θ	(mas)	IF	0.407±0.031	–	–
	(mas)	LC+HP	–	0.247±0.017	0.235±0.017
$M_{\rm BOL}$	(mag)	LC+RV+IF	-1.14±0.22	0.923±0.079	1.120±0.075
V	(mag)	LC	4.250±0.10	5.46±0.11	5.63±0.11
$B-V$	(mag)	LC	-0.12±0.16	-0.05±0.16	-0.03±0.14
$U-B$	(mag)	LC	-0.446±0.16	-0.09±0.14	-0.07±0.14
V_0	(mag)	LC	4.24±0.65	5.54±0.65	5.68±0.65
B_0-V_0	(mag)	LC	-0.120±0.085	-0.018±0.167	-0.015±0.162
				Parallax	
$\pi_{\rm a_1}$	(mas)			15.91 ± 0.93	
$\pi_{\rm a_2}$	(mas)			$*14.96 \pm 0.51$	
$\pi_{\rm DM,Aa}$	(mas)			14.3 ± 4.3	
$\pi_{\rm DM,Ab}$	(mas)			14.4 ± 4.4	
$\pi_{\rm DM,B}$	(mas)			13.3 ± 2.2	

Notes. [1]Assumed. [2]A solution, where $\mathbf{\Omega_1 = 328.4 \pm 1.9}$, is also plausible and has identical χ^2. *Parameters which are likely the closest to the true nature of ξ Tau. Sources: RV.. solution of the RV curve presented in Table 5, SP.. comparison of the observed and synthetic spectra presented in Table 7, LC.. solution of the light curve presented in Table 9, IF.. solution of the V^2 **and** $T_3\phi$ presented in Table 11, HP.. the Hipparcos parallax $\pi = 15.60 \pm 1.04$ mas. The parallaxes: $\pi_{\rm a_1}$ estimated from the size of the semimajor axis of orbit 1 (physical and angular), $\pi_{\rm a_2}$ estimated from the size of the semimajor axis of orbit 2 (physical and angular), $\pi_{\rm DM,Aa}$ estimated from the distance modulus of component Aa, $\pi_{\rm DM,Ab}$ estimated from the distance modulus of component Ab, $\pi_{\rm DM,Ab}$ estimated from the distance modulus of component B.

Table 15. Initial osculating orbital elements $a_j, e_j, i_j, \Omega_j, \omega_j, M_j$ of the ξ Tau system as derived by our N-body model. The epoch is $T_0 = 2\,456\,224.724705$. The values below correspond to that of best-fit solutions with $\chi^2 = 2\,578$, with individual contributions: $\chi^2_{\rm rv} = 2\,237$, $\chi^2_{\rm etv} = 151$, $\chi^2_{\rm edv} = 3.3$ and $\chi^2_{\rm sky} = 185$. The masses of components in $M_\odot$ units were: $m^{\rm Aa} = 2.232911^{+0.000091}_{-0.000093}$, $m^{\rm Ab} = 2.009948^{+0.000092}_{-0.000093}$, $m^{\rm B} = 3.7343^{+0.0070}_{-0.0073}$ and $m^{\rm C} = 0.90^{+0.73}_{-0.04}$. Component B is on its lower limit $m^{\rm B}_{\rm min}$. The mass of component C is very poorly constrained, being rather a distant test mass compared to the others. The 3-σ uncertainties of the elements were determined by a simplified 1-dimensional χ^2 mapping, assuming a relative increase of χ^2 by a factor of 1.13, i.e. suitable for the number of degrees of freedom we have ($\nu = 908$). The uncertainty values were verified using the bootstrap method — with 100 random selections of datasets and corresponding simplex optimisation — but realistic uncertainties are likely to be larger than that because there are a number of local minima with statistically equivalent χ^2 values. We do not report a full correlation matrix of our solution here. Its non-diagonal terms indicate larger values of uncertainties for those elements which are strongly correlated or anti-correlated with others (e.g. $r_{m^{\rm Aa},\omega_2} = 0.74$, $r_{a_1,\Omega_2} = -0.77$, $r_{a_1,\omega_2} = -0.80$, $r_{a_3,i_3} = -0.79$).

Parameter	Value					Unit	Note
a_1	$0.1175673^{+0.0000007}_{-0.0000007}$	a_2	$1.08296^{+0.00033}_{-0.00031}$	a_3	$28.35^{+0.81}_{-0.78}$	au	
e_1	$0.0000^{+0.0020}_{-0.0000}$	e_2	$0.1974^{+0.0009}_{-0.0009}$	e_3	$0.569^{+0.022}_{-0.023}$		
i_1	$86.5^{+3.8}_{-1.5}$	i_2	$86.7^{+2.1}_{-1.9}$	i_3	$-26.3^{+11.6}_{-\ 8.0}$	deg	
Ω_1	$331.4^{+1.4}_{-2.0}$	$\Omega_2^\dagger$	$328.9^{+1.4}_{-1.2}$	Ω_3	$108.3^{+3.3}_{-3.3}$	deg	
ω_1	$274.11^{+0.15}_{-0.15}$	ω_2	$9.62^{+0.14}_{-0.14}$	ω_3	$9.0^{+3.2}_{-3.2}$	deg	
M_1	$176.02^{+0.15}_{-0.15}$	M_2	$85.68^{+0.13}_{-0.12}$	M_3	$31.3^{+1.4}_{-1.4}$	deg	
γ	$8.5^{+1.6}_{-1.6}$					$\mathrm{km\,s^{-1}}$	
i'_1	$93.5^{+1.5}_{-2.8}$					deg	mirror solution with $\chi^2 = 2,545$, Aa+Ab eclipses partially disappear
Ω'_1	$148.5^{+5.8}_{-2.9}$					deg	mirror solution with $\chi^2 = 2,749$, Aa+Ab eclipses partially disappear, orbit 1 is retrograde wrt. orbit 2
				i'_3	$25.6^{+\ 9.3}_{-15.2}$	deg	mirror solution with $\chi^2 = 2,678$

Notes. † The value is expressed in hierarchical Jacobian elements, with respect to Aa+Ab barycentre, because this pair is the most compact and massive. If the reference point would be the photocentre of brightest component B instead, the longitude of the ascending node would be shifted by -180°.

Appendix A: Supplementary material to the spectroscopic observations and their analyses

Details on the reduction procedure of the spectroscopic observations used in this study along with supplementary material to its analysis are given in this Sect..

Appendix A.1: Acquisition and reduction of the spectroscopic observations

The reduction procedure applied to spectra from different observatories (the labelling of observatories corresponds to that introduced in Table 2) were the following:

i) *OND*: All slit spectra were secured at the coudé focus of the 2 m reflector in Ondřejov, Czech Republic,and recorded with the CCD detector PyLoN 2048x512BX. The bias subtraction, flat-fielding, and wavelength calibration were carried out using IRAF[16] (Tody 1986, 1993). The spectra were normalised with Hermite polynomials (order $k \leq 10$).
ii) *FER*: The echelle spectra were acquired with the 2.2 m ESO/MPG reflector at La Silla, Chile and reduced (bias-subtraction, flat-fielding, and wavelength calibration) with a MIDAS pipeline developed specifically for the instrument (Kaufer et al. 1999). The studied regions of the reduced spectra were normalised with Hermite polynomials (order $k \leq 10$).
iii) *BES*: The spectra were acquired with an echelle spectrograph mounted at the 1.5 m Hexapod Telescope at Cerro Amazones, Chile, which is a clone of the FEROS spectrograph and the same MIDAS pipeline was used to carry out the reduction (bias subtraction, flat-fielding, wavelength calibration). The studied regions were normalised with Hermite polynomials (order $k \leq 10$).
iv) *ELO*: The echelle spectra were obtained with the 1.93 m reflector at Observatory Haute Provence. The initial reductions (bias subtraction, flat-fielding, wavelength calibration) were carried out with a pipeline described in Baranne et al. (1996). The studied regions were normalised with Hermite polynomials (order $k \leq 10$).
v) *DDO*: The slit spectra were acquired with the 1.88 m reflector at the David Dunlap Observatory. The initial reductions (bias subtraction, flat-fielding, wavelength calibration) were carried out using IRAF. The spectra were normalised with Hermite polynomials (order $k \leq 10$).
vi) *LIS*: The slit spectra were acquired with the 0.356 m reflector at the Astronomical Observatory of the Instituto Geográfico do Exército, Lisbon. The dark-frame subtraction and flat-fielding were carried out in Maxim DL[17]. The wavelength calibration was carried out using Neon comparison spectra and telluric lines in the program Visual Spec[18]. Removal of the instrumental response was also carried out therein using Castor as a reference star. The spectra were normalised with Hermite polynomials (order $k \leq 10$).

[16] IRAF is distributed by the National Optical Astronomy Observatories, which are operated by the Association of Universities for Research in Astronomy, Inc., under cooperative agreement with the National Science Foundation.
[17] Maxim DL is a commercial software designed for astronomical imaging `http://www.cyanogen.com/maxim/main.php`.
[18] Visual Spec is a freeware designed for the wavelength calibration and the instrumental response removal `http://www.astrosurf.com/vdesnoux/index.html`.

Appendix A.2: Supplementary materials to the analysis of spectroscopic observations

The spectroscopic supplementary material consists of the following Tables and Figs.:

i) Fig. A.1 shows comparison of the disentangled and synthetic profiles. The related analyses are described in Sects. 3.5 and 3.3.

Appendix B: Supplementary material to the photometric observations and their analysis

Details on the reduction procedure of the photometric observations used in this study along with supplementary material to their analysis are given in this Sect..

Appendix B.1: Acquisition and reduction of the photometric observations

The reduction procedure applied to photometric observations from different observatories (the labelling of observatories corresponds to the one introduced in Table 3) were the following:

i) *HVAR*: The differential observations were obtained with the 0.65 m reflector at the Hvar Observatory, Croatia, which is equipped with a photoelectric photometer with an EMI 6256 tube. The observations were acquired relative to the comparison star 4 Tau with the check star 6 Tau observed as frequently as ξ Tau and transformed to the standard UBV system ($UBVR$ for observations acquired after RJD = 56 000) using the non-linear transformations implemented in the reduction package HEC22[19] (see Harmanec et al. 1994; Harmanec & Horn 1998). All observations were reduced with the latest release 18, which allows for time variation in the linear extinction coefficients in the course of the observing night.
ii) *HIPP*: The all-sky observations were acquired with the 0.29 m reflector of the Hipparcos satellite and transformed to V magnitude using the formulæ derived by Harmanec (1998).
iii) *SAAO*: The differential observations were acquired at the South African Astronomical Observatory, South Africa with 0.5 m reflector equipped with a photoelectric photometer. The observations were acquired relative to the comparison star 4 Tau and 6 Tau served as a check star and were transformed to the standard Johnson system using HEC22.
iv) *VILL*: The differential observations were acquired with the Automatic Photometric Telescope at Villanova, USA. The observations were taken relative to the comparison star 4 Tau and 6 Tau served as a check star.
v) *MOST*: The all-sky observations were obtained with the 0.15 m reflector in the MOST satellite. The initial reduction was carried out according to Walker et al. (2003) and references therein. Removal of the remaining instrumental artefacts and the stray light from Earth's atmosphere is described in Sect. 4.

[19] The whole package along with a detailed manual, auxiliary data files, and results is available at `http://astro.troja.mff.cuni.cz/ftp/PHOT`

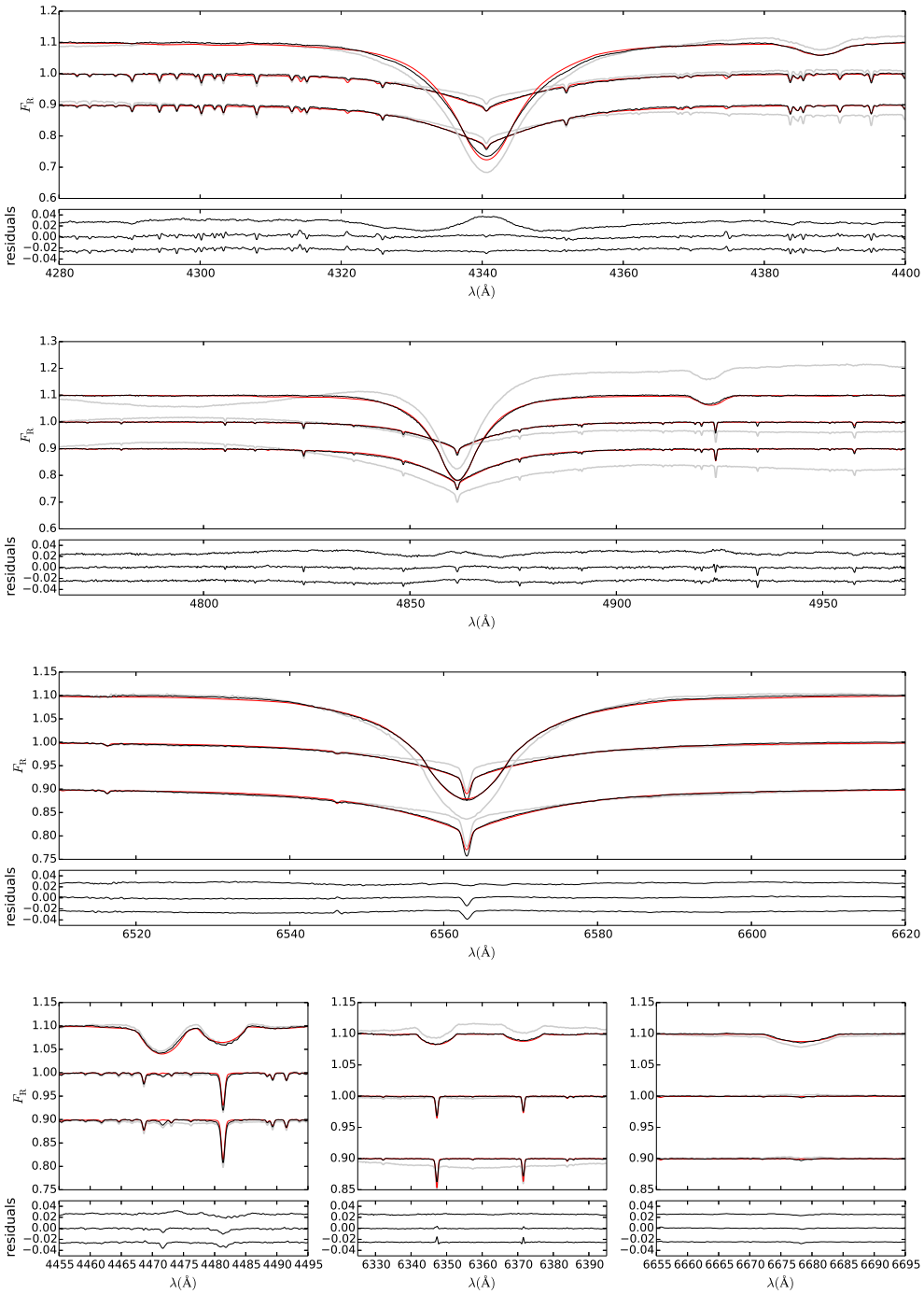

Fig. A.1. A comparison of the disentangled and synthetic spectra. The parameters defining the synthetic spectra are listed in Sect. 3.5. In each panel: top spectrum - component B, middle spectrum - component Aa, bottom spectrum - component Ab, thick grey line - disentangled spectra, thin black line - disentangled and re-normalised spectra, thin red line - synthetic spectra. The residuals are computed for synthetic and re-normalised disentangled spectra.

Appendix B.2: Supplementary materials to the analysis of the photometric observations

The photometric supplementary material consists of the following Tables and Figs.:

i) Fig. B.1 (B.2) shows the available primary (secondary) light curve minima. All minima cover a time interval no longer than 30 d. See Sect. 4 for related analyses.

Appendix C: Supplementary material to the spectro-interferometric observations and their analyses

Details on the acquisition and reduction of the spectro-interferometric observations, along with Tables and Figs. illustrating the analysis are presented in Sect. 6.

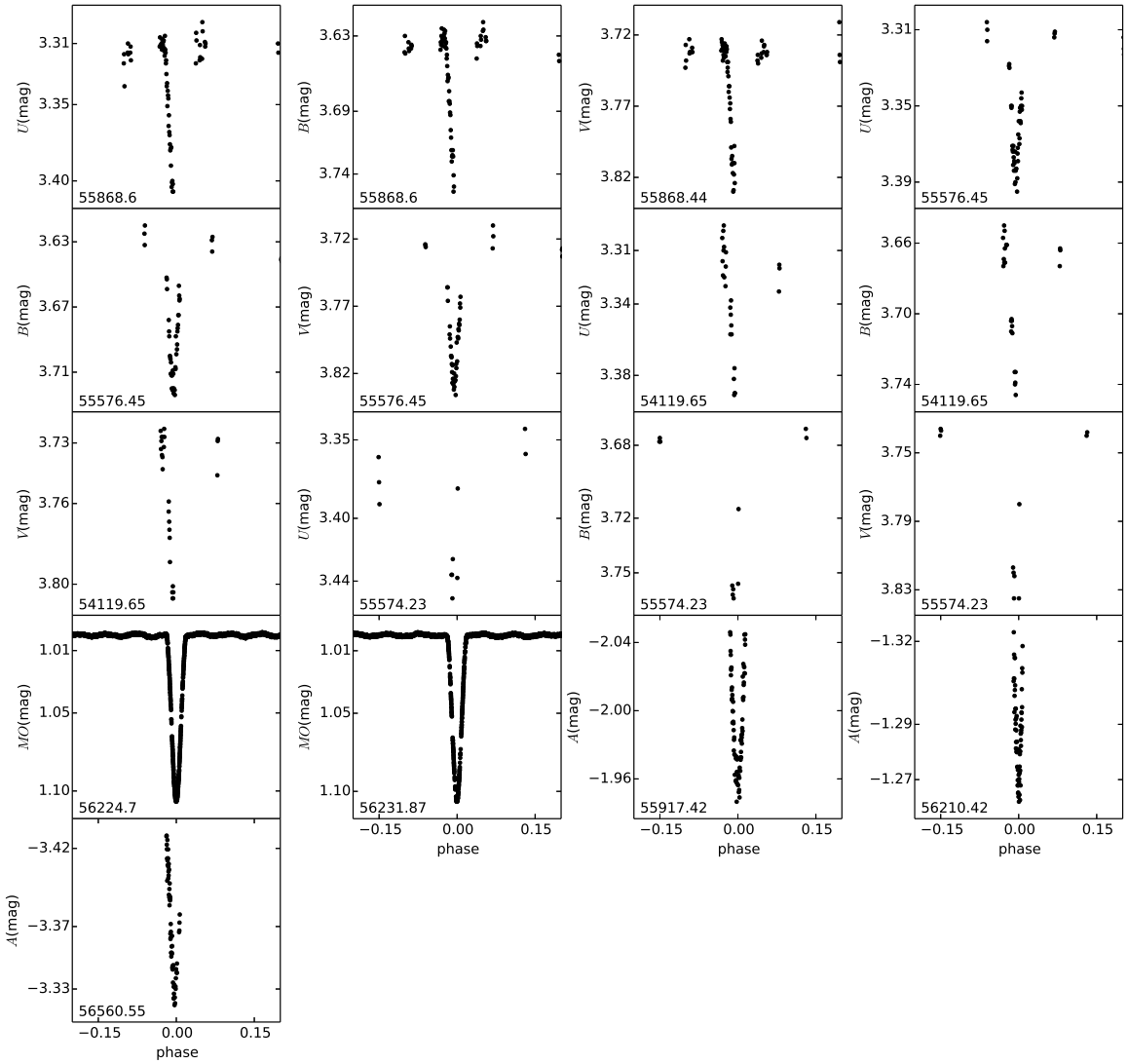

Fig. B.1. All available primary minima of orbit 1. The filters are denoted as follows: UBV - Johnson's UBV filters, MO the MOST filter, and A differential measurements taken in the visible without any filter. Mean RJD is given in the bottom left corner of each panel.

Appendix C.1: Mark III observations

The observations were carried out using a single North-South baseline three times in January 19, October 19, and November 2, 1991. The baseline length was 32 m in the first night, and 15 m in the two other nights. Visibilities were recorded in three narrow-band channels at 5000 Å, 5500 Å, and 8000 Å. μ and η Tau (limb darkened diameters of 0.41 mas and 0.98 mas, respectively, with 10% uncertainties) served as the calibrators. The calibrated visibilities were obtained from the Mark III data archive, which was created using the reduction and calibration methods described by Mozurkewich et al. (2003).

Appendix C.2: NPOI observations

The observations were carried out with the 3-beam combiner in 1998 and 2000, and from 2003 to 2013 with the 6-beam combiner. Visibilities, complex triple amplitudes and closure phases were recorded in 16 narrow-band channels between 5500 Å and 8500 Å. The journal of the NPOI observations including the calibrator stars is given in Table C.2, and the calibrator information is given in Table C.4.

The calibrators were taken from a list of single stars maintained at NPOI with diameters estimated from V and $(V-K)$ using the surface brightness relation by Mozurkewich et al. (2003) and van Belle et al. (2009). Values of $E(B-V)$ were derived from comparison of the observed and theoretical colours as a function of spectral type by Schmidt-Kaler in Aller et al. (1982).

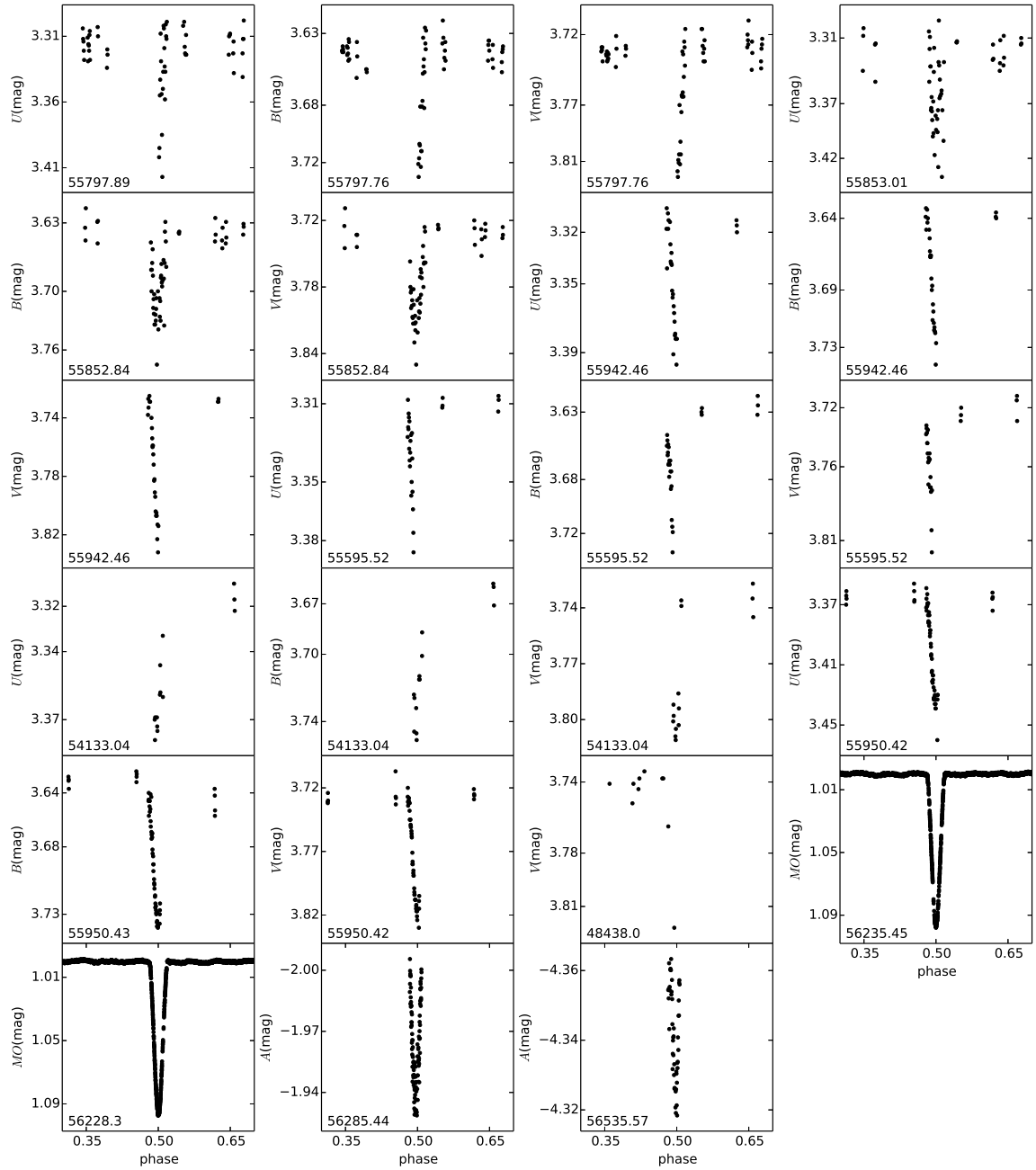

Fig. B.2. All available secondary minima of orbit 1. The filters are denoted as follows: UBV - Johnson's UBV filters, MO the MOST filter, A differential measurements taken in the visible without any filter. Mean RJD is given in the bottom left corner of each panel.

Values for the extinction derived from $E(B-V)$ were compared to estimates based on the maps by Drimmel et al. (2003), and used to correct V if they agreed within $0^{\rm m}.5$. Even though the surface brightness relationship based on $(V-K)$ colours is – to first order – independent of the reddening, we included this small correction. The minimum (squared) visibility amplitudes corresponding to the diameter estimates are given in Table C.4 for all NPOI observations and show that the calibrators are either unresolved or only weakly resolved.

NPOI data and their reductions were described by Hummel et al. (1998) and Hummel et al. (2003). For the first time, we used

a pipeline written in GDL[20] for the OYSTER[21] NPOI data reduction package. The pipeline automatically edits the 1-second averages produced by another pipeline directly from the raw frames, based on expected performance such as the variance of fringe tracker delay, photon count rates, and narrow angle tracker offsets. Visibility bias corrections are derived as usual from the data recorded away from the stellar fringe packet. After averaging the data over the full length of an observation, the closure phases of the calibrators were automatically unwrapped so that their variation with time, as well as that of the visibility amplitude, could be interpolated for the observations of ξ Tau. For the calibration of the visibilities, the pipeline used all calibrator stars observed during a night to obtain smooth averages of the amplitude and phase transfer functions using a Gaussian kernel of 80 minutes in length. The residual scatter of the calibrator visibilities and phases around the average set the level of the calibration uncertainty and was added in quadrature to the intrinsic data errors. The amplitude calibration error of typically a few percent in the red channels up to 15% in the blue channels was added in quadrature to the intrinsic error of the visibilities. The phase calibration was good to about a couple of degrees.

Appendix C.3: VEGA/CHARA observations

The observations were carried out during two runs in 2011 and in 2012. Preliminary results, based on the observations obtained during the first run, were published by Nemravová et al. (2013). The reduction procedure was the same for both runs.

Five observations were acquired in 2011. All observations were obtained in the 3-telescope (3T) mode and included the CHARA baselines E1E2W2, W1W2S2, W2E2S2, ranging from 63 m to 245 m (E1, E2, S1, S2, W1, W2 denote the telescopes in the CHARA telescope array). Ten new observations were secured in 2012. Four of them were taken in the 3T mode and the remaining six were taken in the 2-telescope (2T) mode. The 2T observations included the CHARA baselines S2S1 and E2E1, their projected lengths ranging from 34 m to 66 m. The 3T observations contained the E2E1W2 and W2W1S1 baselines, their projected lengths were from 65 m to 279 m. A detailed journal of all interferometric observations with the instrument CHARA/VEGA is in Table C.3.

The observations were obtained with two cameras centred at 5350 Å (denoted BLUE) and 7300 Å (denoted RED) at spectral resolution $\mathbf{R \sim 5\,000}$. Individual frames were recorded with a frequency of 100 Hz and grouped into blocks containing 2500 frames. Each block was coherently summed up and each observation had from 20 to 90 blocks. Two 20 nm wide bands were chosen in the BLUE region and two 30 nm wide bands in the RED region. The four bands used are $\Delta\lambda_{\rm IF} = \{5320-5520, 5400-5600, 7000-7300, 7300-7600\}$[22] Å. The frames were summed up within these bands and the raw squared visibility $V_{\rm RAW}$ was derived from the sum. The spectral bands have to be narrow because of the limited coherence of the waves due to the atmospheric turbulence. There are no strong stellar lines in any of the four spectral bands used; the spectral band $7300-7600$ Å is affected by the telluric water vapour lines, but even those are smeared out by the low resolution of the spectra.

A calibrator was observed before and after each observation of ξ Tau. Calibrators were selected with the tool SearchCal (Bonneau et al. 2006) and their list along with their basic properties is given in Table C.5. The instrumental visibility was estimated according to the formula:

$$V^2_{\rm SCI}(u,v) = V^2_{\rm SCI-RAW}\frac{V^2_{\rm CAL-UD}}{V^2_{\rm CAL-RAW}}(u,v), \quad \text{(C.1)}$$

where $V^2_{\rm SCI}$ is the calibrated visibility of ξ Tau, $V^2_{\rm SCI-RAW}$ the raw visibility of ξ Tau, $V^2_{\rm CAL-UD}$ the visibility of a uniform disk with a diameter listed in Table C.5, and $V^2_{\rm CAL-RAW}$ the raw visibility of a calibrator. In order to avoid inaccurate observations, we removed all blocks having S/N<2 and whose optical path delay (OPD) differed from the mean OPD by more than 2σ. Such blocks usually represent only random noise rather than a physical signal. In rare cases, when the raw visibility of ξ Tau was close to zero, but safely detected, and there was no suitable observation of a calibrator, the raw visibilities of ξ Tau were used in the analysis as if they were calibrated, but they were assigned an error $\Delta V^2 = 0.05$. This allowed us to save more usable observations for very long baselines giving strong constraints by low visibility measurements.

Appendix C.4: VLTI/AMBER observations

ξ Tau was observed by VLTI/AMBER in 2012 Dec 03. The observations were acquired in a three-telescope mode in J, H, and K bands and the low resolution regime ($R = 35$). The baselines ranged from 41 **m** to 139 m.

The unprocessed observations were downloaded from the ESO archive and the reduction was done with the AMBER data reduction software `amdlib` (Benisty et al. 2015). Following the manual step by step, we applied the bad pixel and flat-field maps, computed pixel-to-visibility matrix, subtracted the dark frame, and performed frame selection based on the fringe S/N ratio (the best 20 % were kept).

Four stars were used as calibrators, as listed along with their basic properties is in Table C.5. The uniform-disk diameters were taken from the JMMC Stellar Diameters Catalogue (Lafrasse et al. 2010). The calibration was done using the library `amdlib`.

Additionally we had to filter the data: 1) Observations having the effective wavelength at the edges of the J, H, and K bands were not removed, although they had large uncertainty and displayed abrupt drop of visibility inconsistent with the remaining data. Only observations whose effective wavelength lied in any of following bands $\Delta\lambda \in \{1.155-1.34; 1.49-1.77; 2.02-2.05; 2.075-2.41\}\,\mu$m were used. 2) Several observations had suddenly very low visibility compared to neighbouring data and are very likely caused by an instrumental and/or atmospheric effect. Those are: i) data taken at RJD = 56 264.767145, ii) all data having $B/\lambda < 1.76\times10^7$, and iii) data taken from RJD = 56 264.776653 to RJD = 56 264.778568 having $B/\lambda > 9.25\times10^7$.

Appendix C.5: Night by night analysis of NPOI observations

The calibrated visibility and phase estimates are rich enough to permit night-by-night estimation of positions of individual com-

[20] `http://gnudatalanguage.sourceforge.net`

[21] `http://www.eso.org/~chummel/oyster`

[22] The only difference between the reduction procedure of the observations acquired in 2011 and 2012 is in the choice of the spectral bands. The following bands were used in 2011 $\Delta\lambda_{\rm IF(OLD)} = \{5350-5450, 5450-5600\}$ Å, and $\Delta\lambda_{\rm IF(OLD)} = \{7000-7200, 7100-7300, 7200-7400\}$ Å.

Table C.1. Astrometric positions of the photocentre of orbit 1 relative to component B derived from night by night analysis of MARK III and NPOI observations. ρ is the separation, θ the position angle measured counter-clockwise from the North, a, b and α are the semimajor axis, semiminor axis, and the position angle (again measured counter-clockwise from the North) of the uncertainty ellipse.

RJD	ρ (mas)	θ (deg)	a (mas)	b (mas)	α (deg)
		NPOI			
51 093.906	9.71	145.08	0.831	0.157	177.1
51 097.971	11.87	148.00	0.838	0.169	169.1
51 171.722	18.31	327.53	0.844	0.153	173.7
51 815.933	7.36	142.65	0.842	0.156	176.2
51 835.927	11.98	149.63	0.853	0.163	171.7
52 913.988	18.72	327.60	0.628	0.111	151.8
52 927.944	18.46	328.68	1.962	0.223	149.7
52 930.924	18.30	329.24	0.608	0.263	167.0
55 463.974	12.48	148.89	1.874	0.256	152.7
55 464.970	12.23	148.82	0.675	0.256	162.2
55 465.970	12.22	149.96	0.666	0.252	162.2
55 466.962	11.74	149.30	0.653	0.254	162.7
55 467.963	11.41	150.01	0.651	0.256	162.8
55 468.959	11.12	150.03	0.650	0.257	162.7
55 469.886	10.93	150.16	0.624	0.274	180.0
55 470.955	10.11	150.39	0.643	0.272	163.5
55 999.608	10.00	334.30	2.952	0.229	130.3
56 001.610	8.30	335.23	3.155	0.250	126.8
56 221.917	5.90	318.92	0.424	0.091	158.9
56 227.894	9.59	322.81	0.544	0.081	160.8
56 228.900	10.52	324.06	0.609	0.098	154.1
56 229.901	11.28	324.86	0.620	0.095	154.8
56 230.899	11.53	324.83	0.631	0.088	156.9
56 235.880	14.12	325.89	0.527	0.081	160.3
56 236.878	14.59	325.94	0.497	0.088	158.4
56 237.869	15.02	326.35	0.552	0.080	161.1
56 238.864	15.45	326.38	0.550	0.080	161.2
56 297.679	4.12	337.15	0.787	0.107	178.3
		MARK III			
48 275.689	18.18	328.84	0.852	0.146	80.6
48 548.925	15.20	323.62	2.490	0.219	72.8
48 562.870	18.02	327.93	1.066	0.314	85.6

ponents. Due to lower resolution, the NPOI interferometer is almost insensitive to orbit 1 and diameters of the three components (Aa, Ab and B) of ξ Tau. Therefore the system was represented by two point sources, and the relative position of component B and the eclipsing binary estimated. The results of the night-by-night analysis are given in Table C.1.

The uncertainty ellipses of position of the photocentre of orbit 1 (which is almost identical with its centre of mass due to similarity of both components of the eclipsing binary) relative to component B were computed from fits to contours of the χ^2 surfaces at the minima rather than deriving them from the interferometric PSF to take into account the limitations of fitting a component position very far from the phase centre. For the contour we chose 25% above minimum to get a reduced $\chi^2_{\rm R}$.

An astrometric fit to positions listed in Table C.1 confirms that NPOI is insensitive to the eclipsing binary, because the derived orbital properties do not differ significantly from those obtained from a global fit to V^2 presented in Table 11.

Appendix C.6: Supplementary materials to the analysis of the spectro-interferometric observations

The spectro-interferometric supplementary material consists of the following Tables and Figs.:

i) Table C.2 lists all available spectro-interferometric observations acquired with the NPOI and MARK III instruments. For each observation the observing stations, its baselines $[B_{\rm min}; B_{\rm max}]$, phase coverage of orbits 1, and 2 ϕ_1, and, ϕ_2, and associated calibrators are given. The numbering of calibrators is given in Table C.4.
ii) Table C.3 lists all available spectro-interferometric observations acquired with the CHARA/VEGA instrument. For each observation the lengths of the projected baselines B and their orientation θ, the phase coverage of orbits 1, and 2 ϕ_1, and, ϕ_2, and associated calibrators are given.
iii) Table C.4 lists all calibrators which were used to calibrate the NPOI observations of ξ Tau. For each calibrator its Johnson V magnitude, spectral type, colour index $V-K$, interstellar reddening $E(B-V)$, the minimum amplitude squared visibility V^2 and the uniform disk diameter $\theta_{\rm V-K}$ for wavelength range from V to K band are given.
iv) Table C.5 lists all calibrators which were used for calibration of the CHARA/VEGA and VLTI/AMBER observations. For each calibrator the spectral type, effective temperature $T_{\rm eff}$, gravitational acceleration $\log g$, Johnson V (K) magnitude V (K), and the uniform disk diameter in these bands $\theta_{\rm V}$, $\theta_{\rm K}$ are given.
v) Figures C.1 – C.10 show fits of the global model given by Eq. (9), and corresponding parameters listed in Table 11.

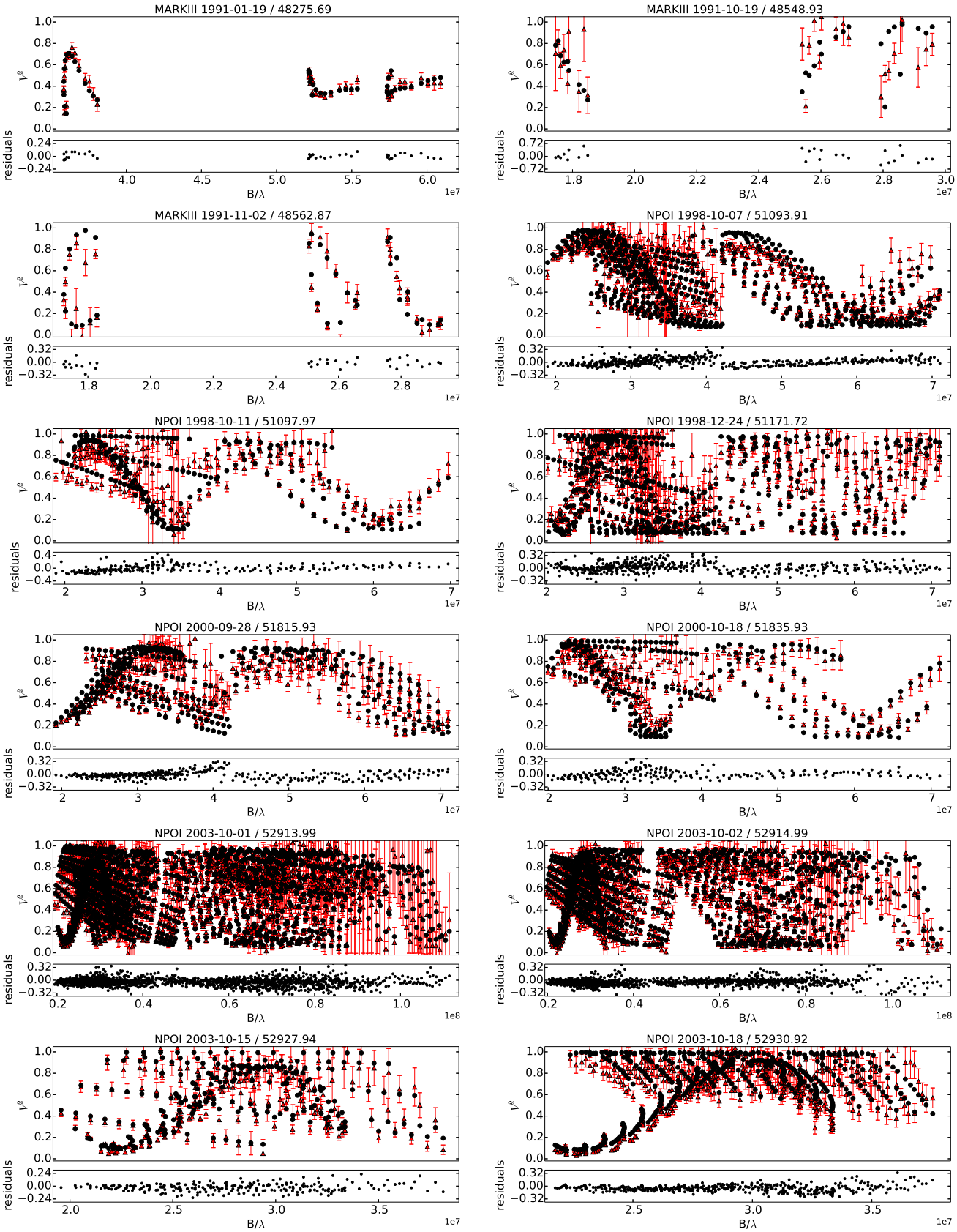

Fig. C.1. Best-fitting model (part one) plotted against the observations from the MARKIII and NPOI spectro-interferometers. In each panel, the observed squared visibility V^2 is plotted with red triangles; the model corresponding to parameters listed in Table 11 is denoted with black points. Residuals of the fit are shown below each panel. The mean acquisition date, the corresponding mean heliocentric Julian date, and the instrument are indicated above each panel.

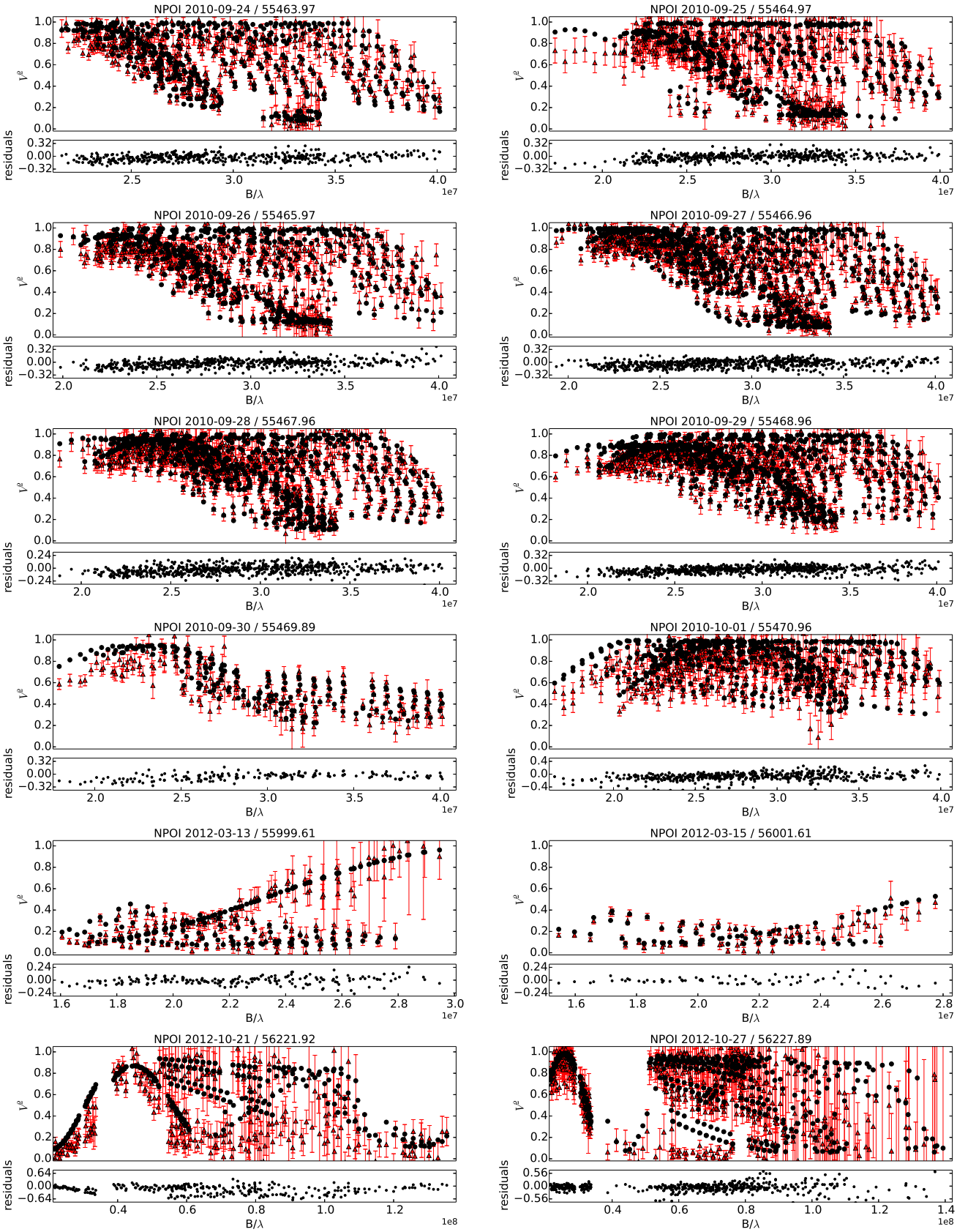

Fig. C.2. Best-fitting model (part two) plotted against the observations from the NPOI spectro-interferometer. In each panel, the observed squared visibility V^2 is plotted with red triangles; the model corresponding to parameters listed in Table 11 is denoted with black points. Residuals of the fit are shown below each panel. The mean acquisition date, the corresponding mean **reduced** heliocentric Julian date, and the instrument are indicated above each panel.

Table C.2. NPOI and MARK III observations of ξ Tau. Column two lists the configuration used as a triple of stations (e.g. "AC-AE-W7", using astrometric stations Centre and East, as well as imaging station W7) if data from all three involved baselines were recorded, including the corresponding closure phase. If a single baseline is listed, only squared visibility data were recorded but no closure phases on that baseline. ϕ_1 (ϕ_2) refers to mean orbital phase of orbit 1 (2) at the given RJD. Calibrator numbers correspond to the numbering in Table C.4.

RJD[1]	Triangles/Baselines	$B_{\min}$ (m)	$B_{\max}$ (m)	ϕ_1	ϕ_2	Calibrators
		NPOI				
51 093.906054	AC-AE-AW	15	37	0.066	0.897	09 11 14 18
51 097.971703	AC-AE-AW	16	37	0.635	0.925	09 11 14 18
51 171.722612	AC-AE-AW	17	37	0.954	0.433	09 11
51 815.933549	AC-AE-AW	16	37	0.096	0.871	01 03 09 08
51 835.927180	AC-AE-AW	17	37	0.894	0.008	20 09 12 14 15 08
52 913.988131	AC-AE-W7, AC-AW-W7	17	63	0.742	0.435	19
52 927.944213	AE-AC, AW-AC	17	49	0.695	0.531	05 19
52 930.924441	AE-AC, AW-AC	19	56	0.112	0.551	05 19
55 463.974404	AC-AE, AC-AW	18	22	0.551	0.000	06 15 16 17 21
55 464.970628	AC-AE, AC-AW	14	22	0.690	0.007	06 15 16 17 21
55 465.970834	AC-AE, AC-AW	17	22	0.830	0.014	06 15 16 17 21
55 466.962039	AC-AE, AC-AW	16	22	0.969	0.021	06 15 16 17 21
55 467.963919	AC-AE, AC-AW	16	22	0.109	0.028	06 15 16 17 21
55 468.959529	AC-AE, AC-AW	15	22	0.248	0.034	06 15 16 17 21
55 469.886574	AC-AE, AC-AW	15	22	0.378	0.041	06 15 16 17 21
55 470.955776	AC-AE, AC-AW	14	22	0.528	0.048	06 15 16 17 21
55 999.608038	AE-AC, AW-AC	13	16	0.500	0.690	10 11 13
56 001.610251	AE-AC, AW-AC	13	15	0.780	0.704	10 11 13
56 221.917782	AC-E6-W7, AC-AE	19	73	0.607	0.221	01 07 11
56 227.894044	AC-AE-W7, AC-E6-W7	19	79	0.443	0.262	07 11 16 02 21
56 228.900174	AC-AE-W7	18	64	0.584	0.269	07 11 16 02 21
56 229.901258	AC-AE-W7	19	67	0.724	0.276	07 11 16 02 21
56 230.899631	AC-AE-W7, W7-E6	18	73	0.863	0.283	07 11 16 02 21
56 235.880496	AC-AE-W7, AC-E6-W7	18	77	0.560	0.317	07 11 16 02 21
56 236.878894	AC-AE-W7, AC-E6-W7	19	75	0.700	0.324	07 11 16 02 21
56 237.869383	AC-AE-W7, AC-E6-W7	19	77	0.839	0.331	07 11 16 02 21
56 238.864654	AC-AE-W7, AC-E6-W7	18	78	0.978	0.338	07 11 16 04 21
56 297.679445	AC-AW-E6	0	53	0.208	0.743	10 11
		Mark III				
48 275.689	NF-SF	29	30	0.725	0.484	μ Tau, η Tau
48 548.925	ND-SC	14	15	0.958	0.366	μ Tau, η Tau
48 562.870	ND-SC	14	15	0.909	0.462	μ Tau, η Tau

Notes. [1]Mean RJD. Ephemeris, which was used to compute the orbital phases: 1 - $T_{\min,1}(\mathrm{RJD}) = 7.1467 \times E + 56\,224.7246$, 2 - $T_{\mathrm{p},2}(\mathrm{RJD}) = 145.17 \times E + 55\,609.05$, where E is the epoch, $T_{\min,1}$ the epoch of the primary minimum of the orbit 1, $T_{\mathrm{p},2}$ the epoch of the periastron passage of the orbit 2.

Table C.4. List of NPOI calibrators used for ξ Tau, where V (K) is the apparent magnitude in the Johnson V (K) filter, $E(B-V)$ the interstellar reddening, V^2 the squared visibility and θ the uniform disk diameter.

No	HD	Type	V	$V-K$	$E(B-V)$	V^2	$\theta_{\mathrm{V-K}}$ (mas)
01	886	B2IV	2.83	-0.940	0.010	0.85	0.498
02	7804	A3V	5.16	0.239	-0.010	0.91	0.366
03	7964	A3V	4.76	0.224	-0.050	0.97	0.434
04	11171	F3III	4.65	0.778	-0.035	0.73	0.653
05	12216	A2V	3.98	0.059	-0.060	0.98	0.562
06	16582	B2IV	4.07	-0.632	0.020	0.99	0.343
07	17081	B7V	4.25	-0.255	-0.010	0.89	0.403
08	20630	G5Vvar	4.83	1.873	0.000	0.86	0.956
09	23630	B7III	2.90	0.264	0.010	0.85	0.981
10	24760	B0.5V	2.88	-0.833	0.110	0.91	0.519
11	25490	A1V	3.91	0.127	0.020	0.77	0.600
12	37128	B0Ia	1.70	-0.573	0.040	0.84	1.012
13	76756	A5m	4.20	0.256	0.190	0.98	0.582
14	184006	A5Vn	3.79	0.192	-0.010	0.93	0.668
15	192696	A3IV-Vn	4.30	0.222	0.030	0.96	0.536
16	195810	B6III	4.03	-0.351	0.020	0.88	0.421
17	196724	A0V	4.82	-0.034	0.000	0.99	0.360
18	213558	A1V	3.77	-0.081	0.000	0.95	0.568
19	214923	B8.5V	3.40	-0.166	0.003	0.85	0.635
20	216735	A1V	4.90	0.060	-0.010	0.99	0.366
21	217891	B6Ve	4.53	-0.220	0.030	0.92	0.360

Table C.5. List of stars used for calibration of CHARA/VEGA and VLTI/AMBER observations. All data were taken from the JMMC Stellar Diameters Catalogue (Lafrasse et al. 2010). T_{eff} denotes the effective temperature, g the gravitational acceleration, θ_{X} the uniform-disk diameter in the passband X, X the magnitude in the passband X.

Calibrator	Parameter								
	T_{eff} (K)	$\log g_{[\mathrm{cgs}]}$	V (mag)	K (mag)	θ_{V} (mas)	θ_{R} (mas)	θ_{J} (mas)	θ_{H} (mas)	θ_{K} (mas)
CHARA/VEGA									
HD 21686	9790	4.1	5.125	5.167	0.245(18)	0.247(18)	0.251(18)	0.252(18)	0.252(18)
HD 18604	13000	3.4	4.703	4.910	0.257(18)	0.257(18)	0.262(18)	0.262(18)	0.263(18)
HD 26793	10500	4.0	5.210	5.357	0.207(15)	0.209(15)	0.212(15)	0.213(15)	0.214(15)
VLTI/AMBER									
HD 25490	9500	4.1	3.891	3.783	0.513(37)	0.518(37)	0.526(37)	0.529(37)	0.530(37)
HD 34909	4660	2.1	7.987	5.775	0.310(23)	0.315(23)	0.323(23)	0.326(23)	0.328(23)
HD 38277	5700	4.4	7.119	5.597	0.318(23)	0.322(23)	0.329(23)	0.331(23)	0.333(23)
HD 38406	5790	4.4	8.197	6.735	0.186(14)	0.188(14)	0.192(14)	0.193(14)	0.194(14)

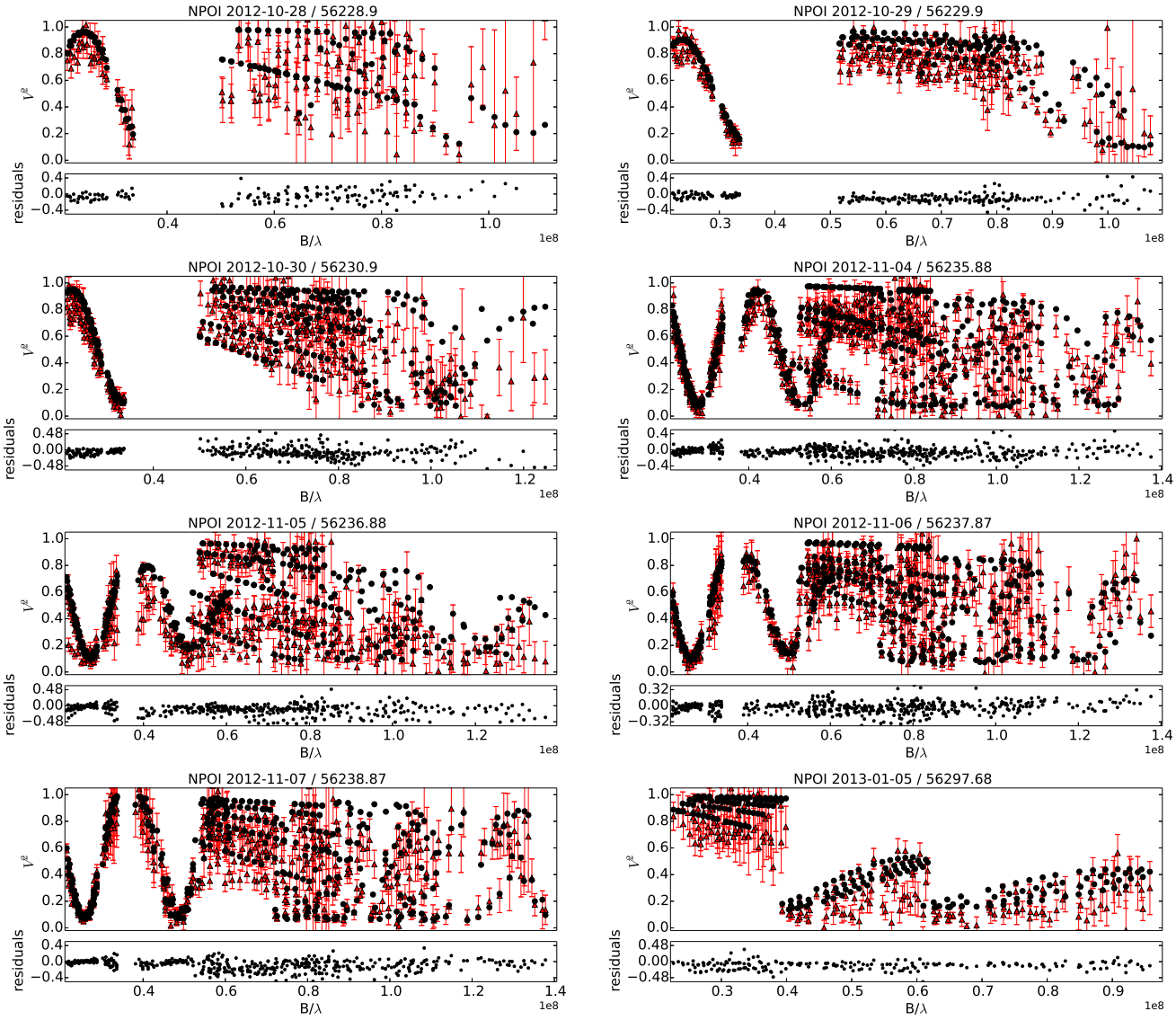

Fig. C.3. Best-fitting model (part three) plotted against the observations from the NPOI spectro-interferometer. In each panel, the observed squared visibility V^2 is plotted with red triangles; the model corresponding to parameters listed in Table 11 is denoted with black points. Residuals of the fit are shown below each panel. The mean acquisition date, the corresponding mean **reduced** heliocentric Julian date, and the instrument are indicated above each panel.

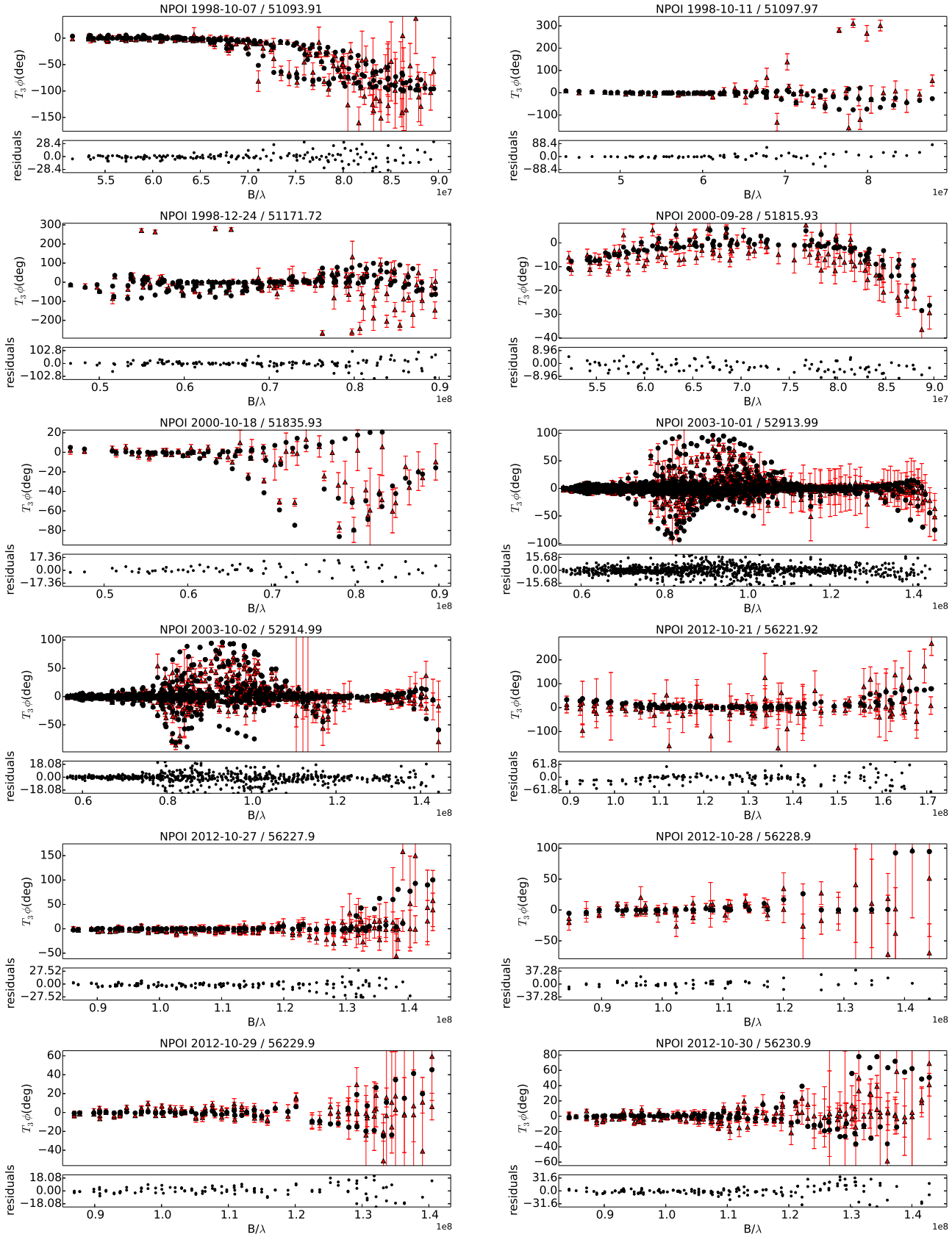

Fig. C.4. Best-fitting model (part four) plotted against the observations from the NPOI spectro-interferometer. In each panel, the observed closure phase $T_3\phi$ is plotted with red triangles; the model corresponding to parameters listed in Table 11 is denoted with black points. Residuals of the fit are shown bellow each panel. The mean acquisition date, the corresponding mean **reduced** heliocentric Julian date, and the instrument are indicated above each panel.

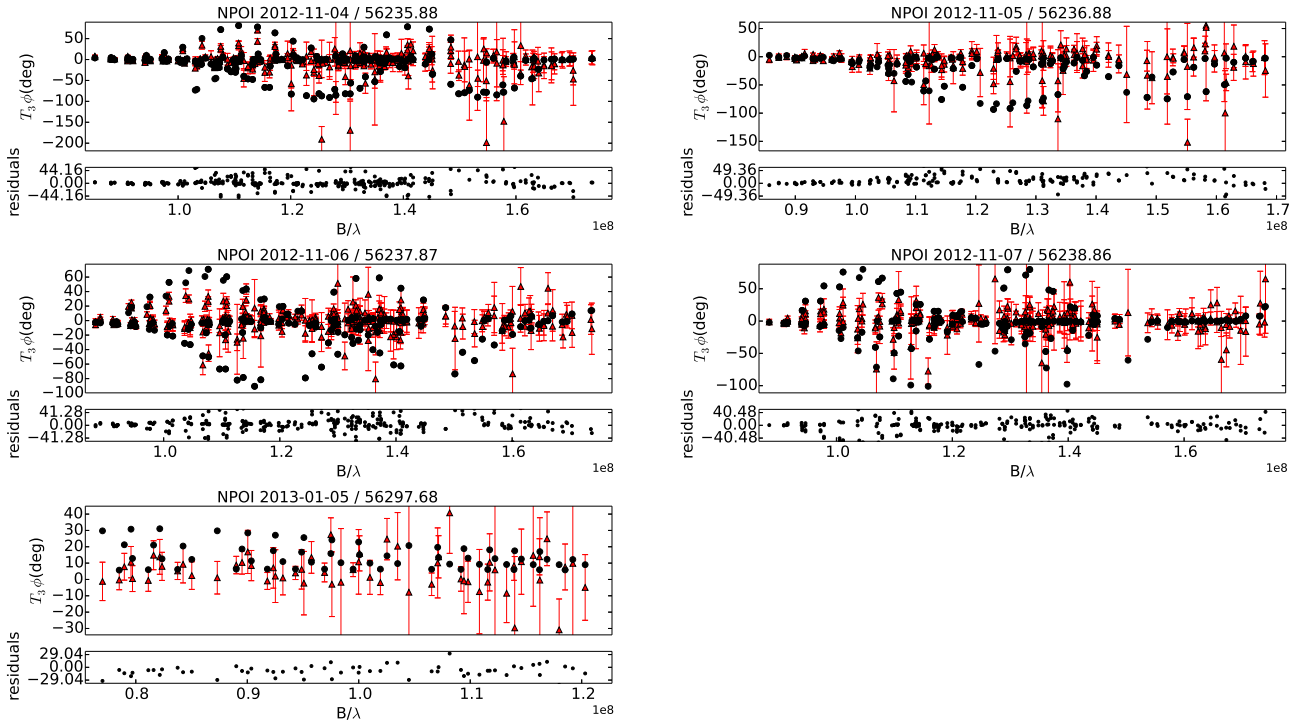

Fig. C.5. Best-fitting model (part five) plotted against the observations from the NPOI spectro-interferometer. In each panel, the observed closure phase $T_3\phi$ is plotted with red triangles; the model corresponding to parameters listed in Table 11 is denoted with black points. Residuals of the fit are shown bellow each panel. The mean acquisition date, the corresponding mean **reduced** heliocentric Julian date, and the instrument are indicated above each panel.

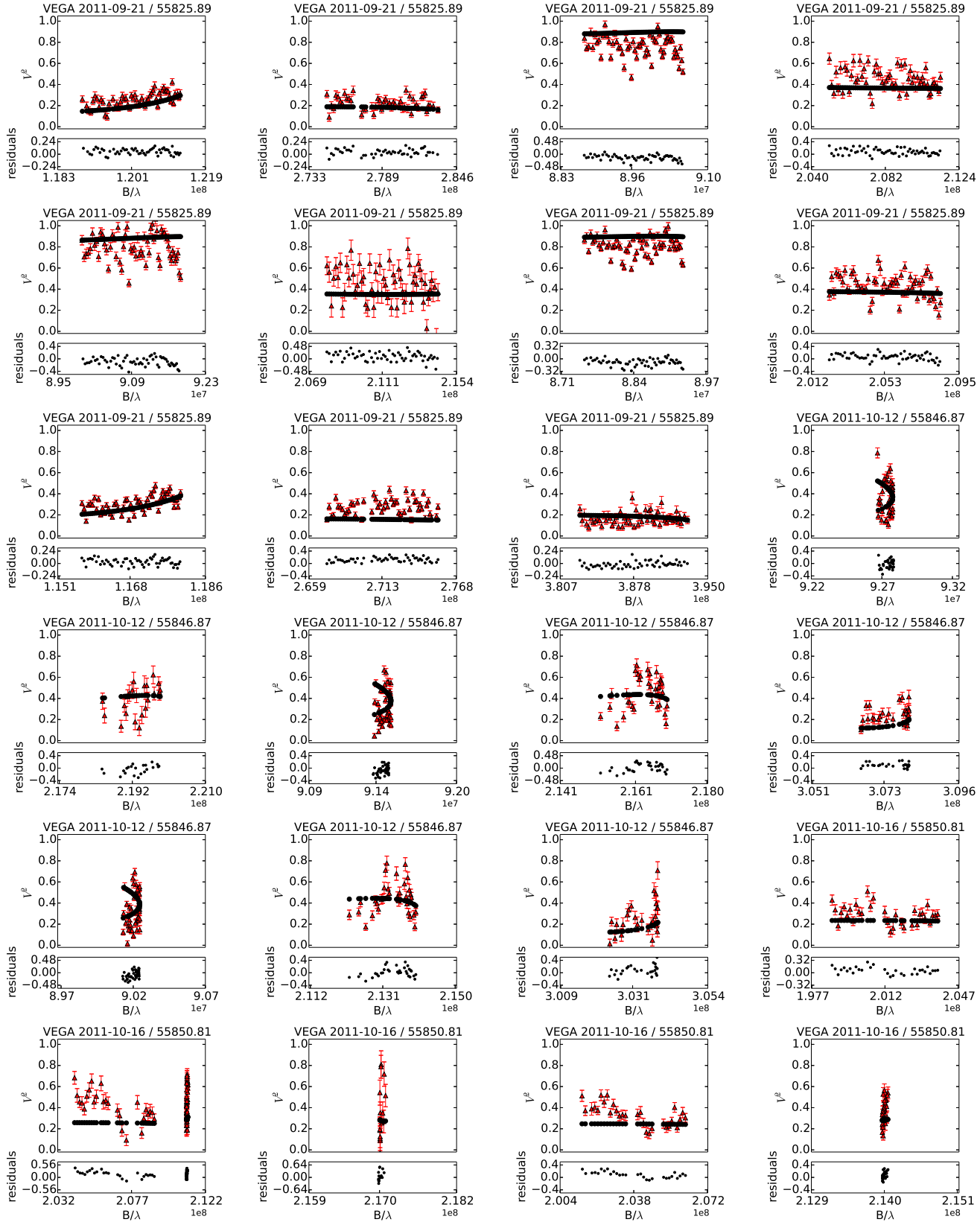

Fig. C.6. Best-fitting model (part six) plotted against the observations from the CHARA/VEGA spectro-interferometer. In each panel, the observed squared visibility V^2 is plotted with red triangles; the model corresponding to parameters listed in Table 11 is denoted with black points. Residuals of the fit are shown below each panel. The mean acquisition date, the corresponding mean **reduced** heliocentric Julian date, and the instrument are indicated above each panel.

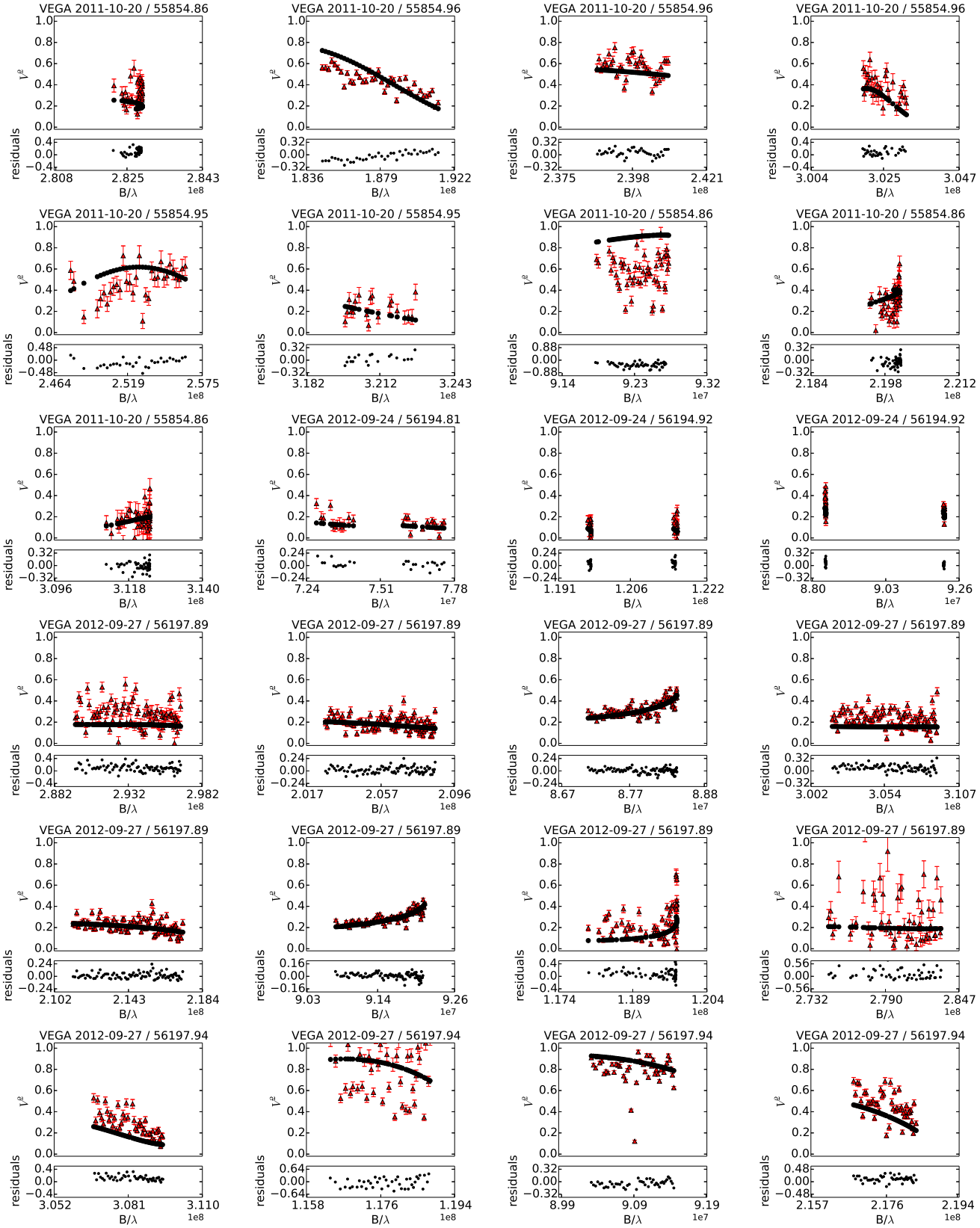

Fig. C.7. Best-fitting model (part seven) plotted against the observations from the CHARA/VEGA spectro-interferometer. In each panel, the observed squared visibility V^2 is plotted with red triangles; the model corresponding to parameters listed in Table 11 is denoted with black points. Residuals of the fit are shown below each panel. The mean acquisition date, the corresponding mean **reduced** heliocentric Julian date, and the instrument are indicated above each panel.

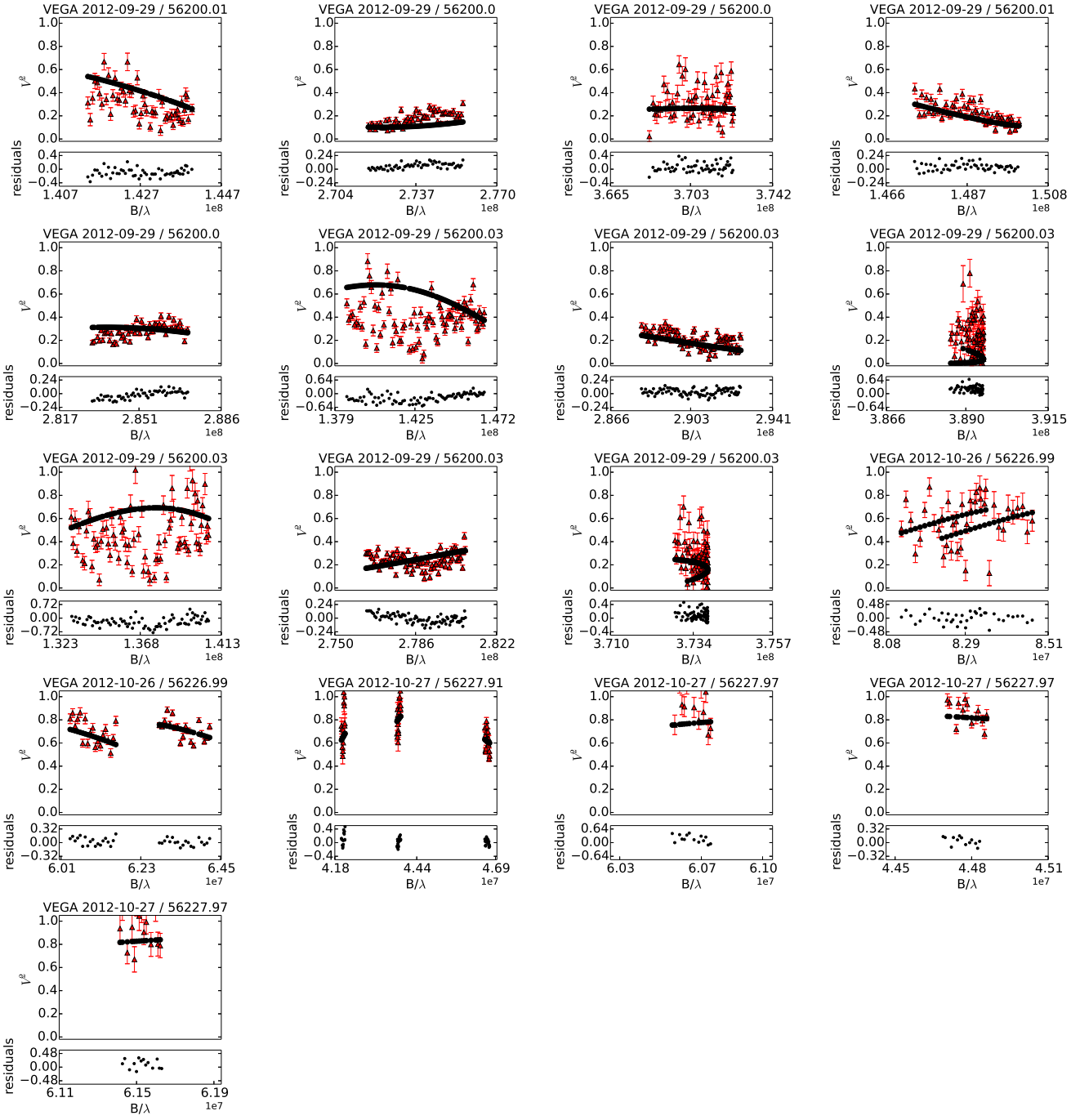

Fig. C.8. Best-fitting model (part eight) plotted against the observations from the CHARA/VEGA spectro-interferometer. In each panel, the observed squared visibility V^2 is plotted with red triangles; the model corresponding to parameters listed in Table 11 is denoted with black points. Residuals of the fit are shown below each panel. The mean acquisition date, the corresponding mean **reduced** heliocentric Julian date, and the instrument are indicated above each panel.

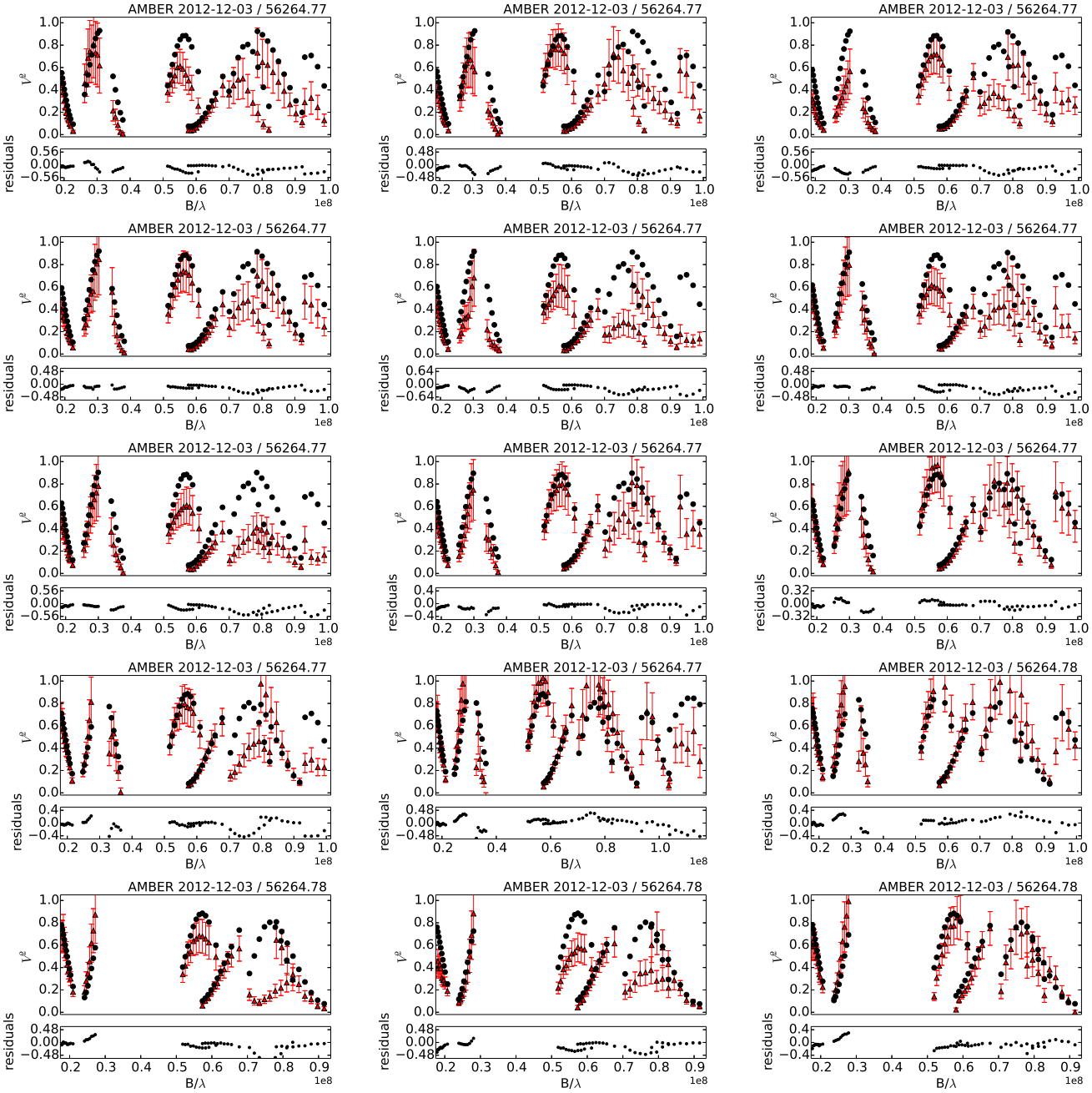

Fig. C.9. Best-fitting model (part nine) plotted against the observations from the VLTI/AMBER spectro-interferometer. In each panel, the observed squared visibility V^2 is plotted with red triangles; the model corresponding to parameters listed in Table 11 is denoted with black points. Residuals of the fit are shown below each panel. The mean acquisition date, the corresponding mean **reduced** heliocentric Julian date, and the instrument are indicated above each panel.

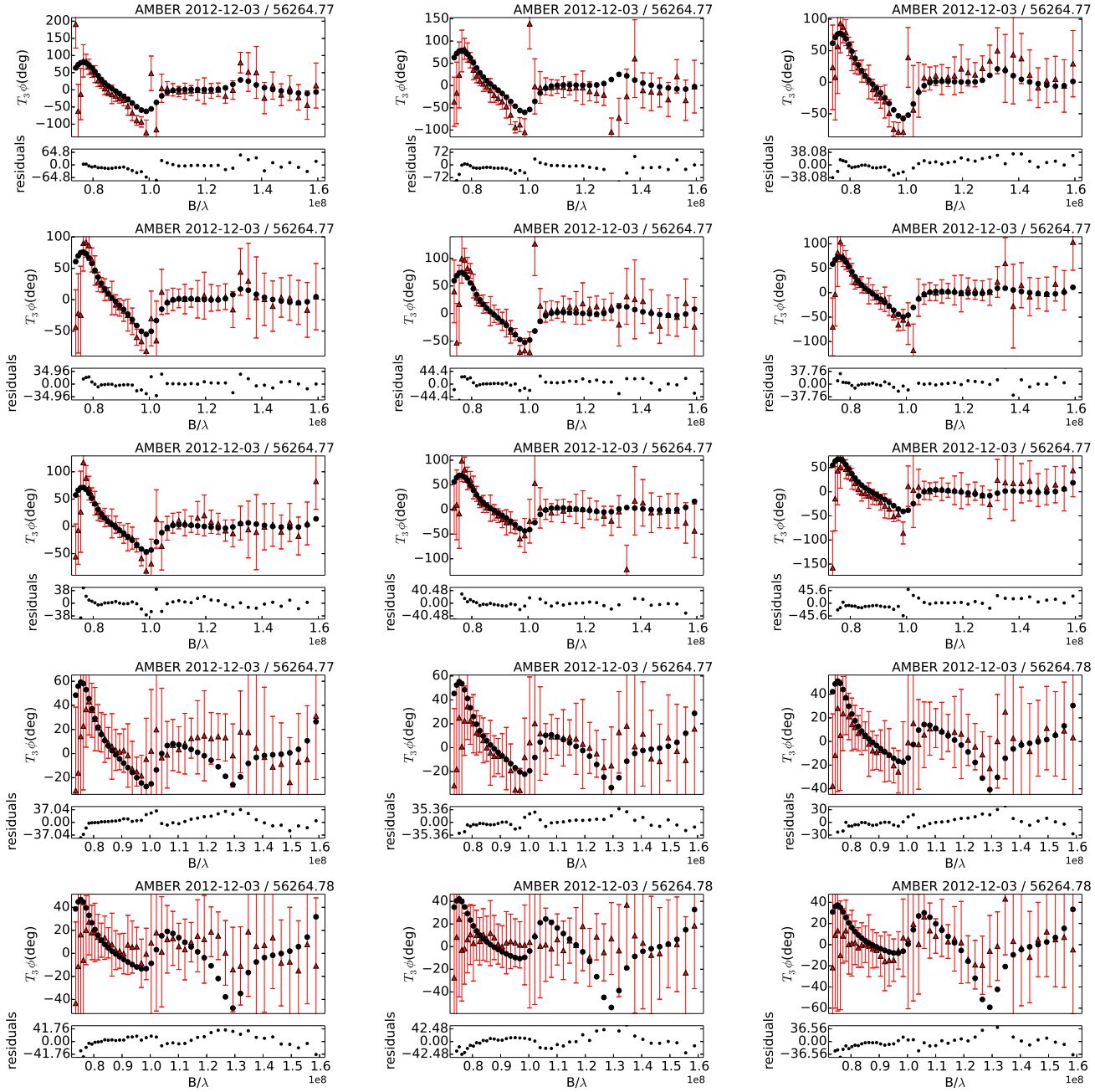

Fig. C.10. Best-fitting model (part ten) plotted against the observations from the VLTI/AMBER spectro-interferometer. In each panel, the observed closure phase $T_3\phi$ is plotted with red triangles; the model corresponding to parameters listed in Table 11 is denoted with black points. Residuals of the fit are shown bellow each panel. The mean acquisition date, the corresponding mean **reduced** heliocentric Julian date, and the instrument are indicated above each panel.

Appendix D: Description of the electronically published observational material

This Sect. contains templates of Tables with observational material, which is published electronically.

- RV measurements are published in Table D.1.
- Photometric observations are published separately for each photometric filter (MO, U, B, $\mathbf{V}$) in Tables D.2, D.3, D.4, D.5.
- The spectro-interferometric observations are published in form of calibrated squared visibility moduli in Table D.6, and closure phases in Table D.7.

Table C.3. Journal of the spectro-interferometric observations of ξ Tau. ϕ_1 (ϕ_2) denotes the orbital phase of orbit 1 (2), B the mean length of the projected baseline, θ the position angle of the projected baseline. The calibrator stars are identified as follows: 1 - HD 21686, 2 - HD 18604, and 3 - HD 26793.

RJD	NB	ϕ_1	ϕ_2	B (m)	θ (deg)	Cal.
The 2011 run						
55 825.8907	3-1	0.193	0.488	064.6	-155.9	1,2
	3-2			150.0	-160.6	1,2
	3-3			217.2	-158.9	1,2
55 846.8703	3-1	0.129	0.633	065.8	-154.2	2
	3-2			155.8	-159.3	2
	3-3			221.4	-157.8	2
55 850.8130	3-1	0.680	0.660	147.0	-160.9	1,2
	3-2			154.1	-090.1	1,2
	3-3			244.8	+056.0	1,2
55 854.8645	3-1	0.247	0.688	065.6	-153.1	1,2
	3-2			156.2	-158.3	1,2
	3-3			221.6	-156.8	1,2
55 854.9548	3-1	0.260	0.688	135.3	-148.5	1,2
	3-2			172.7	-057.7	1,2
	3-3			217.7	+084.1	1,2
55 856.8928	3-1	0.531	0.702	063.3	-149.9	2,3
	3-2			152.5	-155.6	2,3
	3-3			216.3	-154.2	2,3
The 2012 run						
56 194.8118	2-1	0.814	0.029	054.8	-156.0	1
56 194.9180	2-1	0.829	0.030	065.9	-154.1	1
56 197.8894	3-1	0.245	0.050	065.6	-155.2	1
	3-2			153.5	-160.1	1
	3-3			218.7	-158.6	1
56 197.9362	3-1	0.252	0.051	065.0	-152.1	1
	3-2			155.6	-157.5	1
	3-3			220.4	-155.9	1
56 200.0052	3-1	0.541	0.065	106.3	-002.5	1
	3-2			203.9	-060.1	1
	3-3			276.1	-041.1	1
56 200.0306	3-1	0.545	0.065	099.2	-000.3	1
	3-2			207.7	-056.8	1
	3-3			278.3	-039.2	1
56 226.9927	2-1	0.317	0.251	045.4	-125.8	1
56 227.0299	2-1	0.323	0.251	040.0	-109.9	1
56 227.8758	2-1	0.441	0.257	031.3	+100.3	1
56 227.9720	2-1	0.454	0.258	033.4	+117.0	1

Notes. Ephemeris, which was used to compute the orbital phases: 1 - $T_{\mathrm{min},1}(\mathrm{RJD}) = 7.1467 \times E + 56\,224.7246$, 2 - $T_{\mathrm{p},2}(\mathrm{RJD}) = 145.17 \times E + 55\,609.05$, where E is the epoch, T^1_{min} the epoch of the primary minimum of the orbit 1, $T_{\mathrm{p},2}$ the epoch of the periastron passage of the orbit 2.

Table D.1. RV measurements obtained with the cross-correlation technique described in Sect. 3.2. t denotes time, RV the heliocentric radial velocity, $\sigma_{\rm RV}$ the uncertainty of the heliocentric radial velocity, and *component* denotes members of ξ Tau (Aa, Ab, or B).

t (RJD)	RV (km s^{-1})	$\sigma_{\rm RV}$ (km s^{-1})	component
Contents of this Table are available electronically only.			

Notes. RJD = HJD − 2 400 000, components: Aa.. primary of orbit 1, Ab.. secondary of orbit 1, and B.. primary of orbit 2.

Table D.2. Reduced photometric observations acquired with the MOST satellite. t denotes time, MO the magnitude in the MOST filter, and $\sigma_{\rm MO}$ the uncertainty of the magnitude in the MOST filter.

t (RJD)	MO (mag)	$\sigma_{\rm MO}$ (mag)
Contents of this Table are available electronically only.		

Notes. RJD = HJD − 2 400 000

Table D.3. Reduced photometric observations acquired in the Johnson's U filter. t denotes time, U the magnitude in the Johnson's U filter, $\sigma_{\rm U}$ the uncertainty of the magnitude in the Johnson's U filter, and *source* the origin of an observation.

t (RJD)	U (mag)	$\sigma_{\rm U}$ (mag)	source
Contents of this Table are available electronically only.			

Notes. RJD = HJD − 2 400 000, sources: 1.. Hvar Observatory, 2.. South African Astronomical Observatory, 3.. Four College Automatic Photometric Telescope.

Table D.4. Reduced photometric observations acquired in the Johnson's B filter. t denotes time, B the magnitude in the Johnson's B filter, $\sigma_{\rm B}$ the uncertainty of the magnitude in the Johnson's B filter, and *source* the origin of an observation.

t (RJD)	B (mag)	$\sigma_{\rm B}$ (mag)	source
Contents of this Table are available electronically only.			

Notes. RJD = HJD − 2 400 000, sources: 1.. Hvar Observatory, 2.. South African Astronomical Observatory, 3.. Four College Automatic Photometric Telescope.

Table D.5. Reduced photometric observations acquired in the Johnson's V filter. t denotes time, V the magnitude in the Johnson's V filter, $\sigma_{\rm V}$ the uncertainty of the magnitude in the Johnson's V filter, and *source* the origin of an observation.

t (RJD)	V (mag)	$\sigma_{\rm V}$ (mag)	source
Contents of this Table are available electronically only.			

Notes. RJD = HJD − 2 400 000, sources: 1.. Hvar Observatory, 2.. South African Astronomical Observatory, 3.. Four College Automatic Photometric Telescope.

Table D.6. Calibrated squared visibility moduli estimated from studied spectro-interferometric observations. t denotes time, u the baseline projected in the **East-West** direction, v the baseline projected in the **North-South** direction, $\lambda_{\rm eff}$ the effective wavelength, V^2 the calibrated squared visibility modulus, $\sigma_{\rm V^2}$ the uncertainty of the calibrated visibility, and *src* the origin of an observation.

t (RJD)	u (m)	v (m)	$\lambda_{\rm eff}$ (m)	V^2	$\sigma_{\rm V^2}$	src
Contents of this Table are available electronically only.						

Notes. RJD = HJD − 2 400 000, sources: 1.. CHARA/VEGA, 2.. MARK III, 3.. NPOI, 4.. VLTI/AMBER.

Table D.7. Closure phases estimated from studied spectro-interferometric observations. t denotes time, u_1 the first baseline in a closing triangle projected in the **East-West** direction, v_1 the first baseline in a closing triangle projected in the **North-South** direction, u_2 the second baseline in a closing triangle projected in the **East-West** direction, v_2 the second baseline in a closing triangle projected in the **North-South** direction, $\lambda_{\rm eff}$ the effective wavelength, $T_3\phi$ the closure phase, $\sigma_{\rm T_3\phi}$ the uncertainty of the closure phase, and *src* the origin of an observation.

t (RJD)	u_1 (m)	v_1 (m)	u_2 (m)	v_2 (m)	$\lambda_{\rm eff}$ (m)	$T_3\phi$ (deg)	$\sigma_{\rm T_3\phi}$ (deg)	src
Contents of this Table are available electronically only.								

Notes. RJD = HJD − 2 400 000, sources: 1.. CHARA/VEGA, 2.. MARK III, 3.. NPOI, 4.. VLTI/AMBER.